ISSN 1854-0171

ACTA GEOTECHNICA SLOVENICA

2016/2
VOL. 13

ISSN: 1854-0171

ACTA GEOTECHNICA SLOVENICA

Ustanovitelji | Founders

Univerza v Mariboru, Fakulteta za gradbeništvo, prometno inženirstvo in arhitekturo
University of Maribor, Faculty of Civil Engineering, Transportation Engineering and Architecture

Univerza v Ljubljani, Fakulteta za gradbeništvo in geodezijo
University of Ljubljana, Faculty of Civil and Geodetic Engineering

Univerza v Ljubljani, Naravoslovnotehniška fakulteta
University of Ljubljana, Faculty of Natural Sciences and Engineering

Slovensko geotehniško društvo
Slovenian Geotechnical Society

Društvo za podzemne in geotehniške konstrukcije
Society for Underground and Geotechnical Constructions

Izdajatelj | Publisher

Univerza v Mariboru, Fakulteta za gradbeništvo, prometno inženirstvo in arhitekturo
Faculty of Civil Engineering, Transportation Engineering and Architecture

Odgovorni urednik | Editor–in–Chief

Bojana Dolinar — University of Maribor

Uredniki | Co–Editors

Jakob Likar	Geoportal d.o.o.
Janko Logar	University of Ljubljana
Borut Macuh	University of Maribor
Stanislav Škrabl	University of Maribor
Milivoj Vulić	University of Ljubljana
Bojan Žlender	University of Maribor

Posvetovalni uredniki | Advisory Editors

Heinz Brandl	Vienna University of Technology
Chandrakant. S. Desai	University of Arizona
Bojan Majes	University of Ljubljana
Pedro Seco e Pinto	National Laboratory of Civil Eng.

Lektor | Proof–Reader

Paul McGuiness

Naklada | Circulation

200 izvodov - issues

Cena | Price

25 EUR/letnik - 25 EUR/vol.; (50 EUR for institutions/za institucije)

Tisk | Print

Tiskarna Saje

Revija redno izhaja dvakrat letno. Članki v reviji so recenzirani s strani priznanih mednarodnih strokovnjakov. Baze podatkov v katerih je revija indeksirana: SCIE - Science Citation Index Expanded, JCR – Journal Citation Reports / Science Edition, ICONDA - The international Construction database, GeoRef. Izid publikacije je finančno podprla Javna agencija za raziskovalno dejavnost Republike Slovenije iz naslova razpisa za sofinanciranje domačih periodičnih publikacij.

Naslov uredništva | Address

ACTA GEOTECHNICA SLOVENICA
Univerza v Mariboru, Fakulteta za gradbeništvo, prometno inženirstvo in arhitekturo
Smetanova ulica 17, 2000 Maribor, Slovenija
Telefon / Telephone: +386 (0)2 22 94 300
Faks / Fax: +386 (0)2 25 24 179
E-pošta / E-mail: ags@uni-mb.si

Spletni naslov | web Address

http://www.fg.uni-mb.si/journal-ags/

The journal is published twice a year. Papers are peer reviewed by renowned international experts. Indexation data bases of the journal: SCIE - Science Citation Index Expanded, JCR – Journal Citation Reports / Science Edition, ICONDA- The international Construction database, GeoRef. The publication was financially supported by Slovenian Research Agency according to the Tender for co-financing of domestic periodicals.

NUMERIČNO MODELIRANJE VOZIŠČA OJAČENEGA Z GEOCELICAMI IN PRIMERJAVA Z LABORATORIJSKIMI EKSPERIMENTI

Samo Peter Medved *(vodilni avtor)*
Lineal d.o.o
Maribor, Slovenija
E-pošta: samo.medved@lineal.si

Bojan Žlender
Univerza v Mariboru,
Fakulteta za gradbeništvo, prometno inženirstvo in arhitekturo
Smetanova 17, SI-2000, Maribor, Slovenija
E-pošta: bojan.zlender@um.si

Stanislav Lenart
Zavod za gradbeništvo Slovenije (ZAG)
Ljubljana, Slovenija
E-pošta: stanislav.lenart@zag.si

Primož Jelušič
Univerza v Mariboru,
Fakulteta za gradbeništvo, prometno inženirstvo in arhitekturo
Smetanova 17, SI-2000, Maribor, Slovenija
E-pošta: primoz.jelusic@um.si

Ključne besede

fleksibilna vozišča, ojačitev, geocelice, simulator prometnih obremenitev, trajne deformacije, numerično modeliranje

Izvleček

Članek opisuje, na kakšen način lahko izboljšamo uporabnost fleksibilnih voziščnih konstrukcij z uporabo geocelic. V ta namen smo z laboratorijskimi preizkusi preizkušali dva tipa voziščnih konstrukcij (z in brez ojačitve z geocelicami), ki smo jih obremenjevali z dinamično obtežbo, ki je simulirala prometno obremenitev. Preizkušance smo obremenjevali istočasno tako z vertikalno kot horizontalno obremenitvijo z namenom vzpostaviti kompleksno napetostno stanje (rotacija smeri glavnih napetosti). Predstavljena je primerjava med obnašanjem konvencionalne fleksibilne voziščne konstrukcije in voziščne konstrukcije ojačene z geocelicami. Izdelan je bil numerični model laboratorijskih preizkusov in predstavljena je primerjava z rezultati laboratorijskih obremenilnih preizkusov. Laboratorijski preizkusi so bili izvedeni z napravo TLS – simulatorjem prometnih obremenitev, medtem ko je bilo numerično modeliranje izvedeno z uporabo naprednih modelov po metodi končnih elementov (MKE), ki opisujejo trajne deformacije in napetostno stanje nevezanega nosilnega sloja iz kamnitega materiala. Razvoj trajnih deformacij voziščne konstrukcije brez in z ojačitvijo z geocelicami je prikazan na numeričnem modelu in preverjen z rezultati eksperimentov.

MODELING OF A GEOCELL-REINFORCED PAVEMENT: AN EXPERIMENTAL VALIDATION

Samo Peter Medved *(corresponding author)*
Company Lineal d.o.o
Maribor, Slovenia
E-mail: samo.medved@lineal.si

Bojan Žlender
University of Maribor,
Faculty of civil engineering, transportation engineering and architecture
Maribor, Slovenia
E-mail: bojan.zlender@um.si

Stanislav Lenart
Slovenian national building and civil engineering institute (ZAG)
Ljubljana, Slovenia
E-mail: stanislav.lenart@zag.si

Primož Jelušič
University of Maribor,
Faculty of civil engineering, transportation engineering and architecture
Maribor, Slovenia
E-mail: primoz.jelusic@um.si

Keywords

flexible pavement, reinforcement, geocell, traffic load simulator, permanent deformation, numerical modeling

Abstract

This article details how the serviceability of a flexural pavement structure is improved by incorporating the Cellular Confinement System (geocells). For this purpose, two different pavement structures, with and without embedded geocells, were manufactured in a laboratory and an accelerated traffic type of loading was applied. The vertical and horizontal cyclic loads were applied simultaneously to simulate the effect of principal stress rotation. A comparative study between the conventional flexible pavement and the geocell-reinforced flexible pavement is presented. Additionally, numerical models of the laboratory tests were built and the results were compared. The simulation of the experimental tests using the Traffic Load Simulator (TLS) are carried out using the FEM and advanced models that describe the permanent strain behavior of the unbound granular material. The development of permanent deformation within the pavement structure, with and without the geocells, is also presented through the numerical model, which was verified by the experimental results.

1 INTRODUCTION

A pavement structure is a geometrically simple, multi-layered structure. The upper layers are formed by a bound material such as asphalt or concrete, while the lower-base and sub-base layers consist of unbound stone aggregate mixtures. The sub-grade layer under the pavement structure is an embankment or natural ground with features created by geological processes. Reinforcement can be introduced into the pavement structure to improve its cost-effectiveness and to extend the serviceable life of the structure.

Within the research presented in this article, geocell reinforcement is used to optimize the resources used to construct a solid, stabilized base and sub base for the pavement. The research goal was to prove the reduction of lateral as well as vertical movements of the soil particles in a pavement structure when a three-dimensional geocell confinement is used. [1].

Experimental and theoretical studies, which investigate the reinforcement mechanisms and failure modes of pavements reinforced with geocells, are described in the literature [2], [3]. Experimental studies carried out by Pokharel et al. [4] show that the installation of a geocell with a higher elastic modulus increases the stiffness and bearing capacity of a pavement. Accelerated pavement testing of unpaved roads with geocell-reinforced sand bases have been presented by Yang et al. [5]. Based on

the test results, they concluded that geocells significantly improve the stability of unpaved roads with sand bases and reduce the amount of permanent deformation. However, less experimental studies have been carried out on paved structures reinforced with geocells. An analysis and design methodology for the use of geocells in flexible pavements was proposed by Babu et al. [6]. Menegelt et al. [7] show the effect of the geocell on the resilient modulus dependent on the infill material. Resilient modulus tests were conducted on two coarse-grained soils (gravel and sand) and a fine-grained soil (lean silty clay) in a large-size cell with and without the geocell confinement. Singh et al. [8] presented a comparative study looking at a conventional flexible pavement and a geocell-reinforced flexible pavement. The results show a significant improvement in the bearing capacity when using geocell reinforcement.

This article presents the laboratory test results for a flexible pavement structure subjected to traffic loading, which was simulated by applying a synchronized vertical and horizontal cyclic load. A special testing device, named the Traffic Load Simulator (TLS), was constructed at the Slovenian National Building and Civil Engineering Institute (ZAG) for this purpose. In contrast to other similar experimental researches the TLS introduces vertical and horizontal cyclic loads to take into account the specifics of traffic loading, which results in vertical and horizontal normal stresses as well as non-zero values of the shear stress. The latter causes the rotation of the principal stress axis. The impact of embedded geocells (Fig. 1) upon the rutting development, permanent deformation of the pavement structure and its vertical distribution in the base layer are presented. Additionally, this article presents a model for the rutting prediction based on a mechanistic-empirical method for flexible pavements using the layered elastic model. The developed model is compared to the experimental results of TLS tests to determine the accuracy of the proposed model.

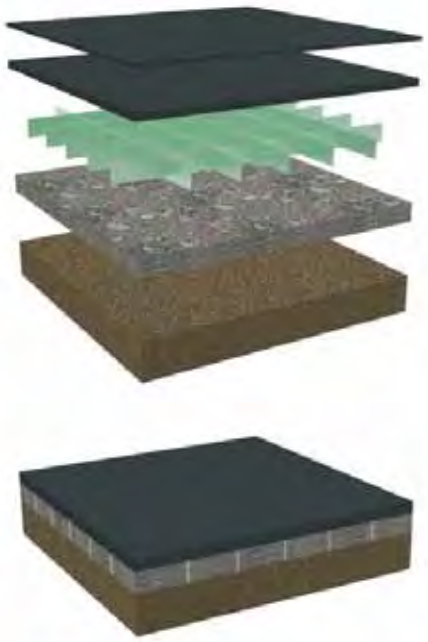

Figure 1. Scheme of a pavement structure reinforced with geocells.

2 EXPERIMENTAL PROGRAM

The arrangement of the laboratory test, the materials used and the details of the experimental program are described in this section. The laboratory test equipment with the Traffic Load Simulator (TLS) is presented in Fig. 3. Two specimens of paved road sections, 0.4 m long, 0.4 m wide and 0.51 m deep, were constructed for the purposes of the experiments in the laboratory. To enable particularities of the traffic load simulation with the principal stress axis rotation, specimens were constructed within 17 rigid aluminium frames. Free, non-frictional movements of the frames were allowed in the horizontal direction. The height of each aluminium frame is 3 cm and the internal layout dimensions are 40 cm × 40 cm. The loading in the vertical direction was applied with a full rubber tire attached to a hydraulic piston. The pavement structure was placed on the base of the loading frame and thereby rigidly supported in the vertical direction. The horizontal loading was applied through the lower aluminium frame with a horizontal hydraulic piston. The horizontal force is measured at the rigidly supported, upper aluminium frame.

Two accelerated pavement tests with multiple stage loading were performed on test specimens without geocells (TLS1) and with geocells directly under the asphalt layer (TLS3).

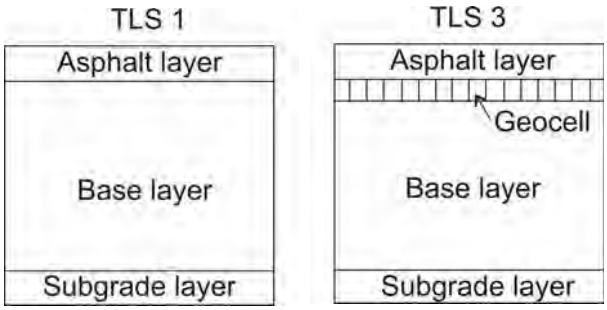

Figure 2. Test specimens without geocell and with geocell reinforcement.

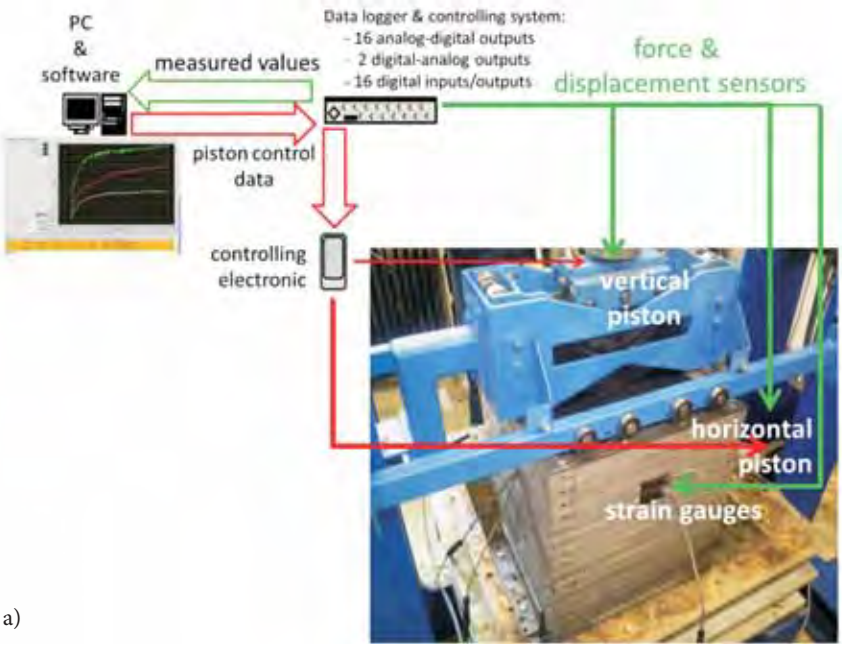

a)

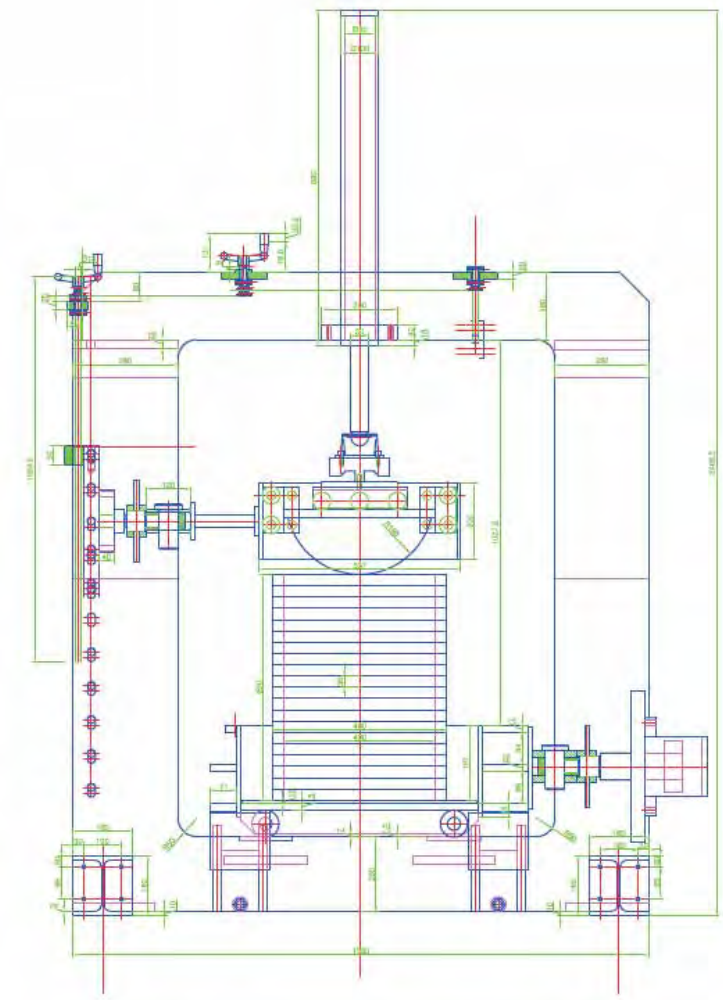

b)

Figure 3. The laboratory test equipment: Traffic Load Simulator (a); Scheme of apparatus (b).

2.1 Material properties

2.1.1 Properties of asphalt

The impact of the type of asphalt used in relation to the deformation characteristics of the pavement was not researched in this study. Thus it was an aim to disable the asphalt effect by using the same type of asphalt layer in the case of the geocell-reinforced and unreinforced specimens. The asphalt mix, AC8 surf B50/70 A3, was prepared in a fixed asphalt mixing plant and left to cool. It was delivered to the laboratory in containers. When the test specimens were constructed in the laboratory, asphalt was heated up to approximately 150°C and manually compacted into 3-cm-thick surface layers. Details about the characteristics of the asphalt layer after the compaction are presented in Table 1. The main aim of preparing the asphalt layer was to minimize the possible differences between the asphalt layers of both test specimens.

Table 1. Characteristics of the material being compacted into test specimens.

		TLS 1	TLS 3
Asphalt	density, ρ (kg/m^3)	2401	2274
Gravel	density, ρ (kg/m^3)	2160	2090
	Water content, w (%)	5.51	5.70

2.1.2 Properties of Geocells

Geocells (Fig. 4) are recognized as a suitable geosynthetic reinforcement for granular soils to support static and moving wheel loads on roadways. The stiffness of the geocells has been identified as a key influencing factor for geocell reinforcement, and hence the rigidity of the entire pavement structure. Laboratory wheel loading tests have shown that the performance of geocell-reinforced bases depends on the elastic modulus of the geocell. The Salvaverde type [9] of geocells has been used in this laboratory test. They are manufactured from a high-density polyethylene (HDPE) material. The height of the Geocells used was 5 cm, size (50 cm × 50 cm), the acceptable load stated by the manufacturer is 350t/m^2, the yield strength, f_u , and the modulus of elasticity E of the material used are 28 MPa and 850 MPa respectively.

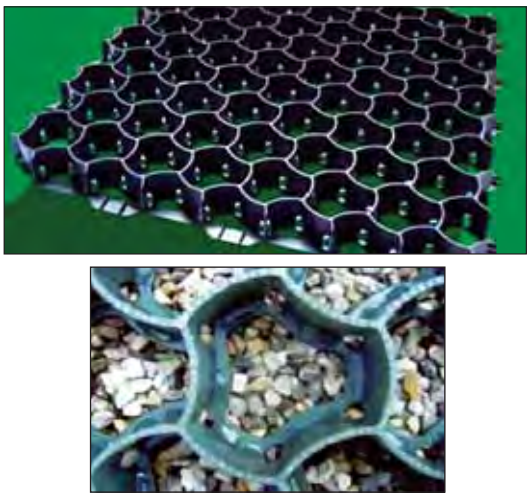

Figure 4. Geocells used in this study.

2.1.3 Properties of the unbound bearing layer

Test procedures for the investigation of mixtures of stone grains, which are intended for unbound bearing layers, are provided by European specifications [10], [11], [12], [13] and [14]. The general characteristics of the gravel material used for the unbound layer are described in more detail elsewhere [12], while a comparison of the densities achieved during compaction are presented in Table 1. The capacity of the unbound base layers was measured through plate-loading tests to determine the values of the deformation for the E_{v1} and E_{v2} modules [TSC 06.200]. The required values of the deformation modules for the unbound bearing layers must meet the requirements in Table 1. It should be noted that the values for the deformation modules are slightly different than expected due to the specimen's preparation particularities. The results for the plate-loading tests measured during the first two cycles for TLS 1 and TLS 3 are presented in Table 2 and Fig. 5.

Table 2. The deformation modules for unbound bearing layers.

D = 155 mm	TLS 1	TLS 3
Determination of E_{v1} module		
u_1 (mm)	1.350	1.264
u_2 (mm)	1.481	1.372
σ_1 (MN/m^2)	0.257	0.257
σ_2 (MN/m^2)	0.356	0.356
E_{v1} (MN/m^2)	87.853	106.563
Determination of E_{v2} module		
u_1 (mm)	1.626	1.440
u_2 (mm)	1.69	1.529
σ_1 (MN/m^2)	0.254	0.255
σ_2 (MN/m^2)	0.349	0.347
E_{v2} (MN/m^2)	172.559	120.168
E_{v2}/E_{v1}	1.96	1.13
The required values of deformation modules for unbound bearing layers		
E_{v2} (MN/m^2)	≥ 90	≥ 90
E_{v2}/E_{v1}	≤2.4	≤2.4

It is clear from the results presented in Table 1 and 2 that the unbound bearing layer in the case of specimen TLS 3 exhibits a lower density and stiffness compared to TLS 1. Similarly, the asphalt in the surface layer was slightly less compacted in the case of TLS 3 compared to TLS 1. Thus, the more deformable behaviour of specimen TLS 3 (if the effect of the geocell reinforcement is neglected) would be expected during traffic loading.

2.1.4 Properties of subgrade

The commercially available, closed-cell elastomer material Sylodyn [15] has been used to simulate soft ground.

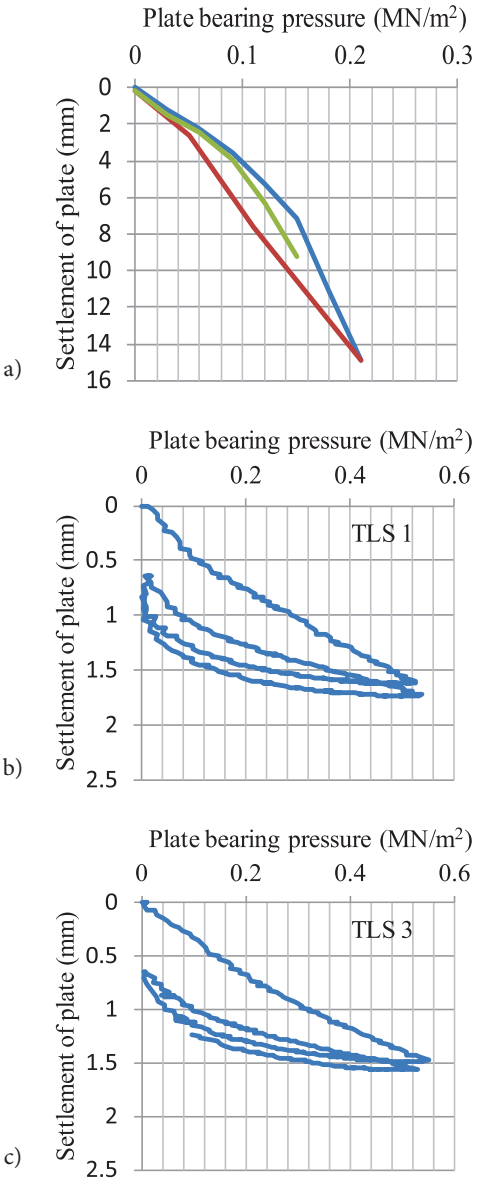

Figure 5. The plate-load test result for the first two cycles for the subgrade layer (a) and the base layer for TLS 1 (b), and TLS 3 (c).

A 5-cm-thick layer of this elastic material enabled equal and constant subgrade conditions for both specimens. Its properties have been tailored in order to meet the requirements for a very low deformation modulus. A typical result of the plate-loading test (loading-blue, unloading-red and reloading-green) of an elastomer material in a subgrade layer is given in Fig. 5a. As can be seen, no permanent deformation developed during cyclic loading of this layer. The Plate Loading Test was carried out in accordance with [16]. It consists of loading a steel plate of known diameter and recording the settlements corresponding to each load increment. The results of the plate-loading test give the modulus of the elastomer material in the subgrade layer equal to 4 MPa. The deformation modulus of the unbound bearing layer of specimens TLS 1 and TLS 3 was measured using the same test method.

2.2 Preparation of the test pavement samples, setup and test procedure

In the first step, a 5-cm-thick elastomer material was positioned to simulate the sub-grade. Next, the unbound granular material was installed and compacted at the moisture content given in Table 1. Approximately 97% (TLS 1) and 95% (TLS 3) of the maximum dry density defined by a modified Proctor compaction test was reached. In the first pavement specimen (TLS 1) only the asphalt layer was installed without any reinforcement. In the second pavement specimen (TLS 3), the geocells were incorporated on the top of the base layer. A very good jointing between the geocells and the asphalt (during the installation phase warm asphalt embraced the top edge of the geocells) was reached. The preparation steps and the installation of the materials for TLS 3 are shown in Fig. 6.

The cyclic loading was then applied through the wheel, through cyclic loading in the vertical and horizontal directions (Fig. 7). Five loading sequences were applied. Vertical loads varied in each loading cycle between the minimum and the maximum value. The minimum value was set to 2 kN for all the loading steps, while the maximum values were 15 kN to 35 kN (see Fig. 7b). The loading process, which includes a load piston and rubber tire, is shown in Fig. 7a. The amplitude of the cyclic horizontal load was approximately one quarter of the vertical amplitude for all the loading steps, while the time diagram of both loads was somehow simultaneous to simulate the rotation of the principal stress. The loading frequency was approximately 0.5 Hz.

Figure 6. Preparation of test pavement specimen.

a)

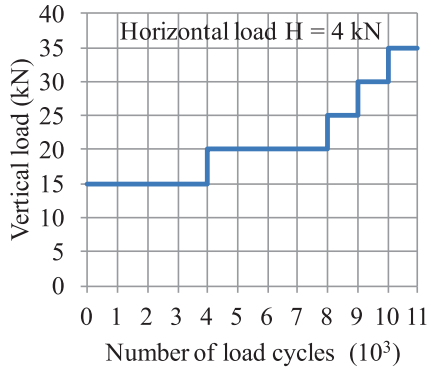

b)

Figure 7. The loading process for the pavement sections (a) and the loading steps (b).

2.3 TLS test results

Before the application of the cyclic load, a plate-loading test on the asphalt layer for TLS 1 and TLS 3 was performed. The settlements obtained in the second cycle were compared with the settlement obtained using a numerical model. The development of the permanent deformation of the pavement structure without geocells (TLS 1) was measured. Fig. 8a presents the result of the plate-loading test on the asphalt layer for the first two cycles. Fig. 8b shows an increasing amount of permanent deformation at the specimen surface, which arises from the deformations of the whole tested structure after each loading step. Since the test specimens differentiate noticeably only in the presence of the geocells, the observed differences in permanent deformation can be contributed to the effect of the geocells. The development of the permanent deformation of the pavement structure with geocells in the contact between the unbound layer and the asphalt layer (TLS 3) is presented in Fig. 9. The increase in the permanent deformation at the asphalt surface with an increasing number of loading cycles is shown in Fig. 10a for both specimens. For the first 4000 loading cycles, a load of 15 kN was applied. After that, an additional 4000 cycles were applied with a load of 20 kN. For loads of 25 kN, 30 kN and 35 kN, a 1000 load cycles were applied sequentially. The increments of the axial permanent deformation ε1 given as a function of the number of loading cycles N is a good indicator of further long-term deformation. Fig. 10b shows the increments in the vertical permanent deformation ε1 for all the loading steps for the number of loading cycles N=1000. The increments arising from Fig. 10a indicate that the installation of the geocells reduced the permanent deformation of the flexural pavement from 12.9 mm (TLS 1) to 6.1 mm (TLS 3), meaning that a decrease in the permanent deformation due to the

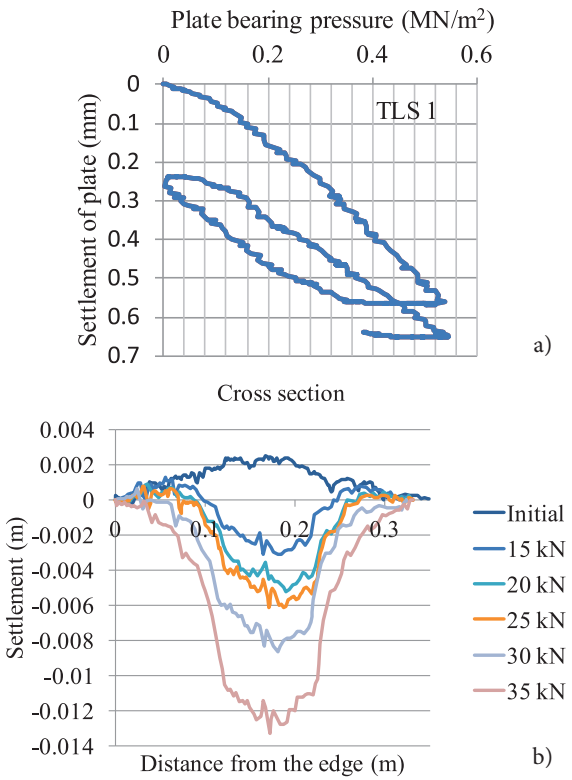

Figure 8. Development of the permanent deformation of the TLS 1: first two cycles of plate-loading test (a), all loading steps (b).

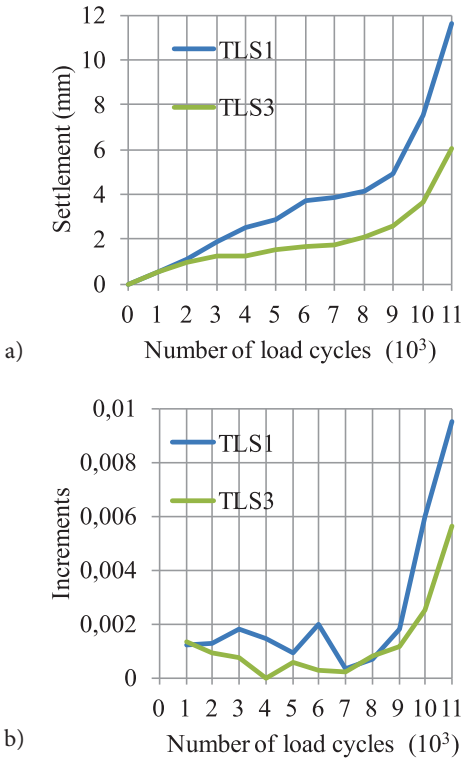

Figure 10. Increase of permanent deformation and the increments of the vertical permanent deformation ε_1 for all loading steps, at N=1000.

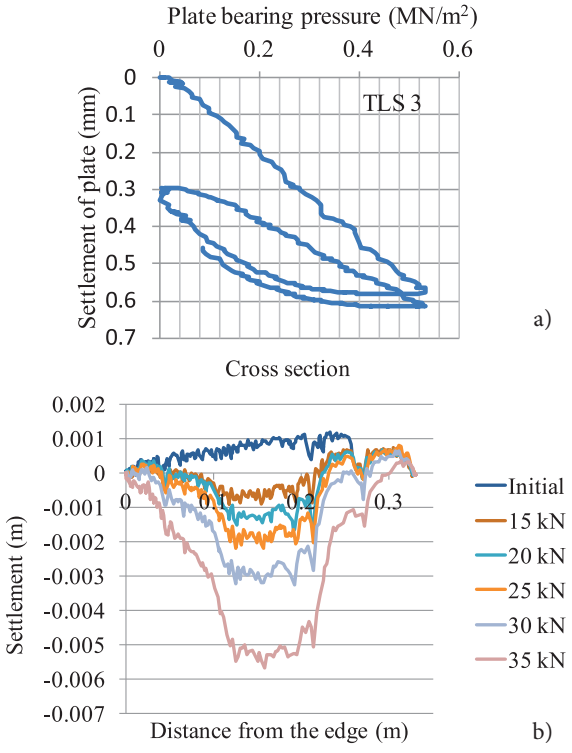

Figure 9. Development of permanent deformation of the TLS 3: first two cycles of plate-loading test (a), all loading steps (b).

geocell reinforcement is approximately 53%. However, it would be necessary to carry out a sufficient number of loading cycles for an accurate prediction of the development of the permanent deformation.

3 NUMERICAL MODELING

Flexural pavement structures exhibit an elastoplastic behaviour in response to the loading and unloading conditions imposed by traffic loads. Upon unloading, this entails both the recoverable and the permanent deformation components. Therefore, the model for the prediction of the deformation of a geocell-reinforced flexible pavement structure consists of two steps: the resilient and the permanent deformation. The first step is to calculate the elastic stress-strain response for a given wheel load using a finite-element modelling (FEM) program. To estimate the permanent deformation response of the pavement structure the Tseng and Lytton [17] relationship was used (Eq. 14). In this way the lifespan of the pavement structure is evaluated. In this section the numerical models of TLS 1 and TLS 3 are presented.

3.1 The resilient response of the pavement structure

A finite-element analysis program (EverStressFE) was used to simulate the response of flexible pavement systems subjected to a wheel load. The model consists of a three-layer pavement system with finite plan dimensions of 400 mm × 400 mm loaded with a single tire. The material properties, such as the flexural stiffness of the asphalt layer S_a, the flexural stiffness of the geocells S_c, the resilient modulus M_r and the Poisson`s ratio μ of the base layer are estimated in this step. The layer thickness and the estimated material properties of these materials are presented in Table 3. The asphalt mixture's stiffness is determined by using the European norm EN 12697-26 [18].

Table 3. Cross-section of pavement structure composition and the mechanical properties of the layers.

Layer	Input data	TLS1	TLS 3
Asphalt layer	Thickness (mm)	30	30
	Flexural stiffness (MPa)	3000	3000
	Poisson's ratio (-)	0.35	0.35
Geocell	Thickness (mm)	/	50
	Flexural stiffness (MPa)	/	2000
	Poisson's ratio (-)	/	0.3
Base layer	Thickness (mm)	430	380
	Resilient modulus (MPa)	173	120
	Poisson's ratio (-)	0.35	0.35
Sub-grade layer	Thickness (mm)	50	50
	Resilient modulus (MPa)	4	4
	Poisson's ratio (-)	0.35	0.35

The resilient modulus of the base layer is estimated by using a repeated load triaxial compression test, according to European norm SIST EN 13286-7:2004 EN 13286-7 [19]. A cyclic load triaxial test was used to determine the resilient strain. The resilient strain εr is taken as the unloading strain from the maximum dynamic stress down to the static contact stress. The resilient modulus M_r is defined as the relationship between the cyclic deviatoric stress and the resilient axial strain. Several models could be used to describe the resilient behaviour of the unbound granular material in cyclic triaxial tests. The Witczak-Uzan equation [20] is used for the numerical analyses. Uzan [21] proposed a model that considers the effect of the shear stress on the resilient modulus as follows:

$$M_r = K_1 \cdot \theta^{K_2} \cdot \sigma_d^{K_3} \qquad (1)$$

where K_1, K_2, and K_3 are regression analysis constants evaluated by a multiple regression analyses of the experimental data. Uzan's model considers both the effect of the bulk stress (θ) and the deviator stress (σ_d), which are directly related to the maximum shear stress

$$\tau_{\max} = \frac{\sigma_d}{2} \; . \qquad (2)$$

Witczak and Uzan [20] modified the model by including the octahedral shear stress in the model instead of the deviator stress.

$$\frac{M^r}{p_a} = K_1 \cdot p_a \cdot \left(\frac{\theta}{p_a}\right)^{K_2} \cdot \left(\frac{\sigma_d}{p_a}\right)^{K_3} \qquad (3)$$

$$\tau_{oct} = \frac{\sqrt{2}}{3} \cdot (\sigma_1 - \sigma_3) \qquad (4)$$

The mesh in the FEM is locally refined to obtain a given level of solution accuracy. The rectangular tire contact is modelled with a constant applied stress equal to the tire pressure. The tire pressure is linearly increased with the load. The load per tire F (kN) and the tire width w (mm) were determined. When 15 kN was applied, the tire pressure was 750 kPa and when 35 kN was applied, 1750 kPa was assigned. The FEM (Fig. 11) is designed to analyse complex pavement structures for which analytical solutions do not necessarily exist. Two FE models were solved and the results were compared to the experimental values in order to investigate the accuracy of the FE

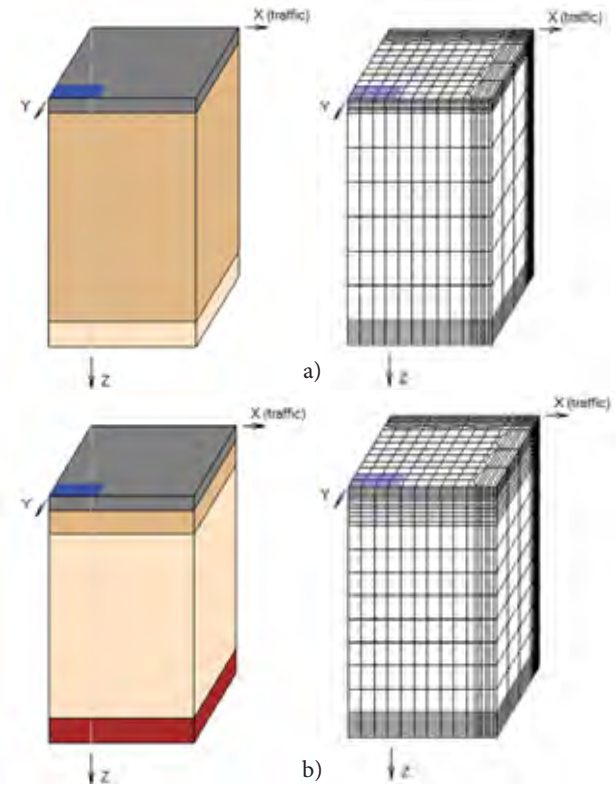

Figure 11. Numerical models of laboratory-tested specimens: without geocell (a) and with geocell reinforcement (b).

Table 4. Calculated horizontal strains at the bottom of the asphalt layer, the average vertical strains and the octahedral shear stress at the base layer.

F (kN)	TLS 1			TLS 3		
	At the bottom of the asphalt layer	Average values in the base layer		At the bottom of the asphalt layer	Average values in the base layer	
	ε_t (10^{-6})	τ_{oct} (kPa)	ε_v (10^{-6})	ε_t (10^{-6})	τ_{oct} (kPa)	ε_v (10^{-6})
15	721.2	57.2	1154.5	29.3	21.8	547.2
20	961.6	76.3	1539.3	39.0	29.0	729.7
25	1202.0	95.4	1924.1	48.8	36.3	912.1
30	1442.4	114.4	2308.9	58.5	43.5	1094.5
35	1682.8	133.5	2693.7	68.3	50.8	1276.9

solution. The vertical strain, horizontal strain, and vertical displacement were obtained for both the TLS1 and TLS3 models (see Table 4). The outputs examined were primarily the maximum vertical (surface) displacement (Fig.12); however, the vertical strains and horizontal strains were also recorded (Fig. 13). The chosen vertical

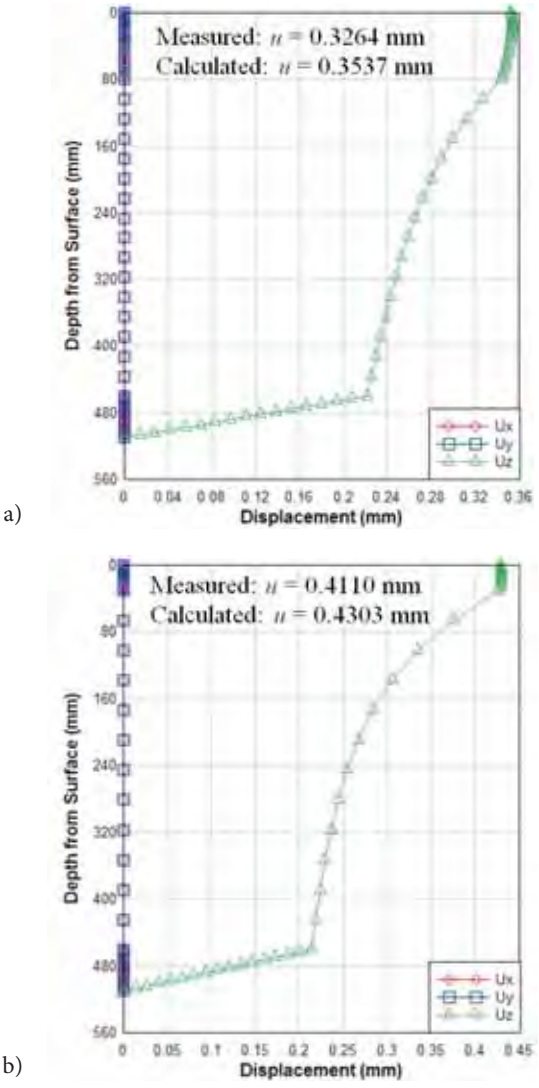

Figure 12. Calculated settlements of the pavement structures using the finite-element modelling.

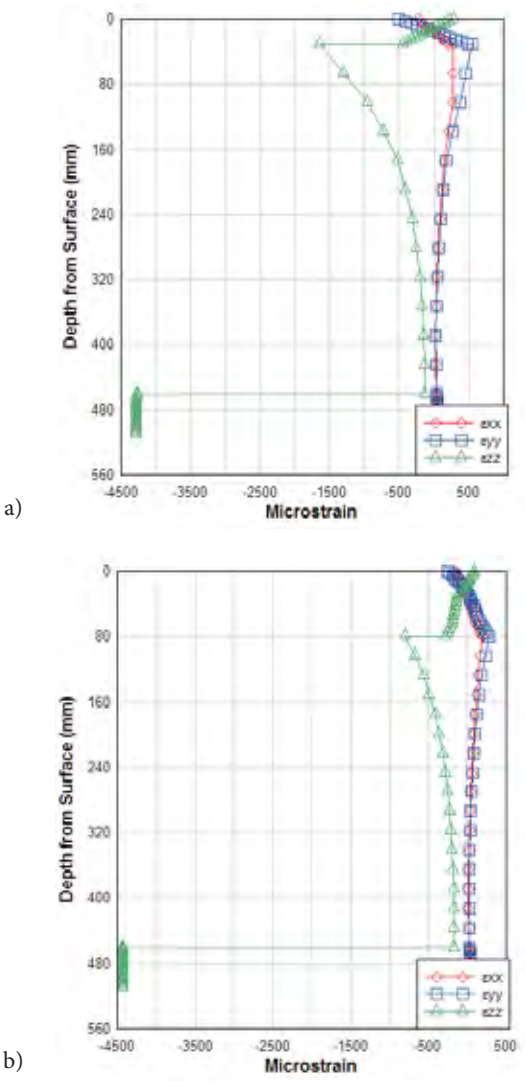

Figure 13. Calculated strains in the cross-section of the test pits: without geocell (a) and with geocell reinforcement (b).

and horizontal strains were the same strains that would be used in the rutting and fatigue prediction models. The settlements in the second cycle of the laboratory test are consistent with the results of the numerical model.

3.2 Permanent deformation of pavement structure

For the prediction of permanent strain in the pavement structure, the following Tseng and Lytton relationship [17] is used:

$$\delta_{1,p}(N) = \frac{\varepsilon_0}{\varepsilon_r} \cdot e^{-\left(\frac{\rho}{N}\right)^{\beta}} \cdot \varepsilon_v \cdot h \qquad (5)$$

where ε_r is the resilient strain and ε_0 is the maximum permanent strain at a very high number of loading cycles, both measured in the laboratory, h is the depth of the layer and ε_v is elastic strain in the pavement layer, computed from the FEM analysis. The parameters ε_0, ρ and β are defined by laboratory tests using the repeated load triaxial apparatus with the Tseng and Lytton procedure [17].

The determination of the permanent deformations and the failure criteria for gravel materials are based on repeated load tests as defined in EN 13286-7 [14] and SIST EN 13286-7:2004 [19]. The magnitude and development of permanent deformations depends on the static stress state of the material, the magnitude of the repeated load, the magnitude of the spherical and distortional repeated load components and the relationship between them, the number of loading cycles, and the physical properties of the material (density, water content, etc.).

Many researchers, like Paute et al. [22] , have tried to relate the permanent deformation after a given number of cycles to the applied stresses (generally the maximum stresses). Some of these relationships also try to couple the effects of both stresses and the number of load cycles. Consider the model of Hornych et al. [23] and Paute et al. [22], the relation between the axial permanent deformations $\varepsilon_1^p(N)$ and the number of loading cycles N is given by:

$$\varepsilon_1^{p^*} = \varepsilon_1^p(N) - \varepsilon_1^p(100) = A \cdot \left[1 - \left(\frac{N}{100}\right)^{-B}\right] \qquad (6)$$

where $\varepsilon_1^p(100)$ is the axial permanent deformation after 100 cycles and $\varepsilon_1^{p^*}(N)$ is the normalized axial permanent deformation at $N > 100$.

Eq. 6 describes the normalized axial permanent deformation, where the parameters A and B define the deformation growth with the number of loading cycles. Parameter A denotes the limit of the function of the permanent axial deformations, where the parameter B denotes its deflection.

The increments of the axial permanent deformation ε_1 are used as an indicator of further long-term deformation and to determine the slope of the failure line. The increments of the axial permanent deformation are given as a function of the number of loading cycles N in the following form [24]:

$$\frac{d\varepsilon_1^p}{dN} = \frac{A \cdot B}{N} \cdot \left(\frac{N}{100}\right)^{-B} \qquad (7)$$

The magnitudes of the parameters A and B depend on the stress level that is expressed by the spherical and deviator stress components

$$p = \sigma_0 + \frac{\sigma_1 + 2 \cdot \sigma_3}{3} \qquad (8)$$

$$\sigma_d = \sigma_1 - \sigma_3 \qquad (9)$$

The maximum axial permanent deformation or parameter A varies in proportion to the maximum deviatory and spherical stresses given in Eq. 8.

$$A = \frac{\frac{\sigma_{d,\max}}{(p_{\max} + p^*)}}{a - b \cdot \frac{\sigma_{d,\max}}{(p_{\max} + p^*)}} \qquad (10)$$

where the stress parameter p^* is defined using a section of the failure line with σ_d axis in p-σ_d space. It is determined from a linear equation of test data, according to the method of least-square deviation.

$$\sigma_d = k \cdot p - p^* \qquad (11)$$

where k is the slope of the line. The parameters a and b are determined from the test data, with a linear equation of the inverse value of parameter A, using the method of least-square deviation.

$$A^{-1} = a \cdot \left[\frac{\sigma_{d,\max}}{(p_{\max} + p^*)}\right]^{-1} - b \qquad (12)$$

The relationship between the parameters a and b gives the slope of the failure line, given by the parameters M and S.

$$\sigma_{d,f} = \frac{a}{b} \cdot (p + p^*) = M \cdot p + S \qquad (13)$$

where S is the failure deviatoric stress component σ_d for the spherical stress component $p = 0$ and M is the slope of the failure line. To predict the permanent strain parameter the Tseng and Lytton [17] relationship was used:

$$\varepsilon_{1,p}(N) = \varepsilon_0 \cdot e^{-\left(\frac{\rho}{N}\right)^{\beta}} \qquad (14)$$

where ε_0 is the maximum permanent strain at a very high number of loading cycles, N is the number of cycles and ρ, β are parameters. These parameters are expressed as functions of the octahedral deviator stress τ_{oct} based on a set of repeated load triaxial compression tests. Table 5 shows the parameters which are used for the permanent strain prediction.

The prediction of permanent strain in the pavement structure is calculated using the Tseng and Lytton [17] procedure (Eq. 5). Using the parameters from Table 5, the prediction of long-term deformation for all the loading steps with and without the geocell reinforcements was calculated. Fig. 14 shows the long-term prediction for all the loading steps for the pavement model without geocells (TLS 1) and the comparison of the permanent deformation of TLS 1 and TLS 3 for a loading step of 15 kN. Additionally, the development of permanent deformation is compared with the laboratory test, for all the loading steps conducted with a traffic-load simulator (see Fig. 15).

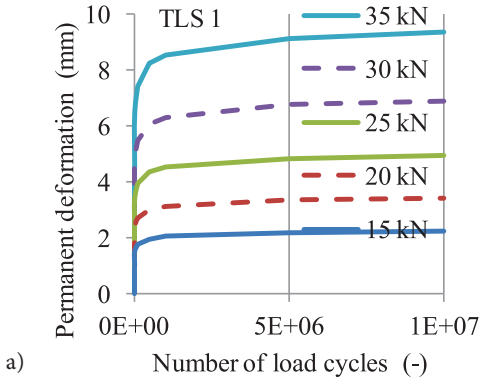

a)

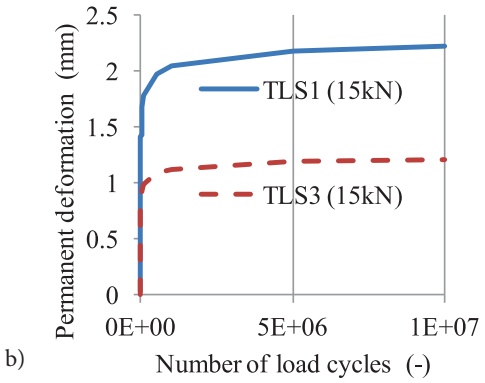

b)

Figure 14. Predicted permanent deformation for TLS 1 and TLS 3 for a large number of cycles.

Table 5. Base-layer permanent strain parameters for TLS 1 and TLS 3.

Load (kN)	τ_{oct} (kPa)	ε_v	ε_0	ε_r	ρ	β
Permanent strain parameters for TLS 1						
15	57.2	0.001155	0.002673	0.000520	0.2135	832
20	76.3	0.001539	0.003492	0.000579	0.2016	808
25	95.4	0.001924	0.004560	0.000646	0.1928	791
30	114.4	0.002309	0.005956	0.000720	0.1860	776
35	133.5	0.002694	0.007779	0.000803	0.1803	764
Permanent strain parameters for TLS 3						
15	21.8	0.000547	0.002712	0.000425	0.2587	916
20	29.0	0.000730	0.002402	0.000442	0.2443	890
25	36.3	0.000912	0.002658	0.000461	0.2337	871
30	43.5	0.001095	0.002943	0.000481	0.2254	855
35	50.8	0.001277	0.003257	0.000501	0.2186	842

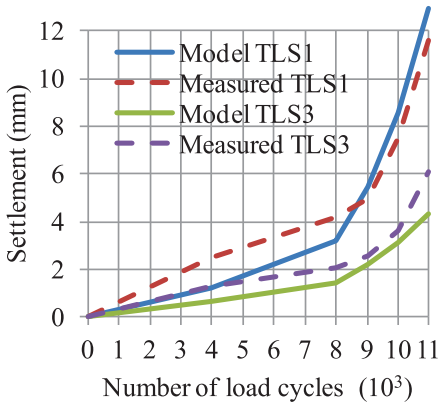

Figure 15. Measured and predicted permanent deformation for TLS 1 and TLS 3 for all the loading steps.

6. CONCLUSION

A pavement structure was constructed in a laboratory to measure the permanent deformation caused by cyclic loading. To reduce the settlement and permanent deformation, geocells were incorporated into the base layer. A laboratory test shows that the permanent deformation was reduced by approximately 53% due to the geocell reinforcement. The laboratory test was also conducted to validate the numerical model for geocells' reinforcement use in pavement design. The numerical model allows the horizontal strain at the bottom of the asphalt layer to be calculated, which is used to determine the fatigue life of the asphalt layer. The results of the numerical model

show that the horizontal strain in the asphalt layer decreases significantly when geocells are used in the pavement structure. Consequently, the fatigue life of the asphalt layer is extended.

REFERENCES

[1] Kief, O., Rajagopal, K. 2008. Three dimensional cellular confinement system contribution to structural pavement reinforcement. Geosynthetic India '08 Seminar, Hyderabad, India.

[2] Rea, M., Mitchel, J. 1978. Sand reinforcement using paper grid cells. Proceedings of the regular Meeting , Rocky Mountain Coal Mining Institute, 644-663.

[3] Dash, S.K., Sireesh, S., Sitharam, T.G. 2003. Model studies on circular footing supported on geocell reinforced sand underlain by soft clay. Geotextiles and Geomembranes 21, 197-219. doi:10.1016/S0266-1144(03)00017-7

[4] Pokharel, S., Han, J., Leshchinsky, D., Parsons, R., Halahmi, I. 2010. Investigation of factors influencing behavior of single geocell-reinforced bases under static loading. Geotextiles and Geomembranes 28, 570-578. doi:10.1016/j.geotexmem.2010.06.002

[5] Yang, X., Han, J., Pokharel, S., Manandhar, C., Parsons, R., Leschinsky, D., Halahmi, I. 2011. Accelerated pavement testing of unpaved roads with geocellreinforced sand bases. Geotextiles and Geomembranes 32, 95-103. doi: 10.1016/j.geotexmem.2011.10.004

[6] Babu, G., Kumar, P. 2012. An approach for evaluation of use of geocells in flexible pavements. Delhi, India.

[7] Mengelt, M., Edil, T., Benson, C. 2006. Resilient modulus and plastic deformation of soil confined in a geocell. Geosynthetics International 13 (5), 195-205. doi: 10.1680/gein.2006.13.5.195

[8] Singh, Y., Shankar, R., Jayan, A. 2015. Design of Geocell Reinforced Flexible Pavement. International Journal of Engineering Research & Technology 4,3. doi: http://dx.doi.org/10.17577/IJERTV4IS031111

[9] Geoplast, 2016. The right protection for turf driveway. Available: swww.geoplast.it/en/products/green/salvaverde.

[10] European Standard EN 1097:2003 Tests for mechanical and physical properties of aggregates.

[11] European Standard EN 1744:2003 Tests for mechanical and physical properties of aggregates.

[12] European Standard EN 932:2003 Tests for general properties of aggregates.

[13] European Standard EN 993:2003 Tests for geometrical properties of aggregates.

[14] European Standard EN13286:2003 Unbound and hydraulically bound mixtures, Tests methods.

[15] Getzner, 1990. The material for the most stringent requirements, 2016. Available: www.getzner.com/en/products/sylodyn.

[16] British Standard BS 1377 Part 9:1990.

[17] Tseng, K., Lytton, R. 1989. Prediction of Permanent Deformation in Flexible Pavements Materials in Implication of Aggregates in the Design, Construction and Performance of Flexible Pavements. Philadelphia: H.G. Schreuders and C.R. Marek.

[18] European Standard EN 12697-26:2012-03 Bituminous mixtures, The methods for hot mix asphalt; part 26: Stiffness.

[19] European Standard, SIST EN 13286-7:2004 Unbound and hydraulically bound mixtures - Part 7. Repeated load triaxial test for unbound mixtures.

[20] Witczak, M., Uzan, J. 1988. The Universal Airport Pavement Design System: Granular Material Characterization. University of Maryland, Department of Civil Engineering, Maryland.

[21] Uzan, J. 1985. Characterization of Granular Material, Washington D.C.

[22] Paute, J., Jouvre, P., Martinez, J., Ragenau, E. 1988. Modele de calcul pour le dimensionnement des chausses souples. Bulletin de laisons des Laboratoires des Ponts et Chaussees 156, 21-36.

[23] Hornych, P., Corte, J., Paute, J. 1993. Etude des deforamations permanentes sous chargements repetes de trois graves non traitees. Bulletin de laisons des Laboratoires des Ponts et Chaussees 184, 45-55.

[24] Ficko, G., Žlender, B. 2005. The analysis of permanent deformations of repeatedly loaded gravels from the Mura region. Acta Geotechnica Slovenica 2, 2, 25-37.

[25] Wasseloo, J., Visser, A., Rust, E. 2009. The stress–strain behaviour of multiple cell geocell packs. Geotextiles and Geomembranes 27, 31-38.

GNSS MONITORING GEOLOŠKO ZAHTEVNIH OBMOČIJ

Boštjan Kovačič *(vodilni avtor)*
Univerza v Mariboru,
Fakulteta za gradbeništvo, prometno inženirstvo in arhitekturo
Smetanova 17, SI-2000, Maribor, Slovenija
E-pošta: bostjan.kovacic@um.si

Boško Pribičević
University of Zagreb,
Faculty of geodesy
Kačićeva 26, HR-10000, Zagreb, Hrvaška
E-pošta: bpribic@geof.hr

Rok Kamnik
Univerza v Mariboru,
Fakulteta za gradbeništvo, prometno inženirstvo in arhitekturo
Smetanova 17, SI-2000, Maribor, Slovenija
E-pošta: rok.kamnik@um.si

Ključne besede

geodezija, geotehnika, monitoring, gnss meritve, geologija, deformacijska analiza, geodetska mreža

Izvleček

Spremljanje pomikov s pomočjo tridimenzionalnih globalnih navigacijskih satelitskih metod (GNSS), ki so del geodetskih metod, postajajo ključne preiskave pri ugotavljanju modelov vzrokov in posledic med zunanjimi naravnimi vplivi na eni in kriteriji, ki opisujejo nivo funkcionalnosti in varnosti naravnega ali zgrajenega objekta na drugi strani v primerih pomikov v prostoru in času.

Glavni cilj deformacijske analize je potrditi stabilnost referenčnih točk geodetske mreže. Uporablja se za določitev pomikov kontrolnih točk, ki so stabilizirane na opazovanem objektu. Domneva o stabilnosti določenih referenčnih točk mora temeljiti na trdnih dokazih skozi meritve in biti potrjena skozi numerične metode. To je en del deformacijske analize; takrat ko določamo vrednosti pomikov in deformacij. Za to je potrebna transformacija, pri kateri se izvede primerjava med koordinatami istih točk v dveh različnih časovnih epohah. Na osnovi ocenjenih transformacijskih parametrov se lahko sklepa o možnih pomikih znotraj referenčnih točk še posebej ali so se spremenili datumski parametri. Po potrditvi stabilnosti geodetske mreže se lahko določijo koordinatne razlike identičnih točk merjenih v različnih časovnih okvirjih, ki se lahko nato opredelijo kot pomiki in/ali deformacije opazovanega objekta. V članku je podana ocena viadukta glede na geologijo in tektonske aktivnosti pa tudi glede na izveden obremenilni preizkus. Viadukt je lociran na precej aktivnem območju, obremenilni preizkus pa je pokazal, da se objekt na zunanjo obtežbo obnaša v skladu s pričakovanji.

GNSS MONITORING OF GEOLOGICALLY DEMANDING AREAS

Boštjan Kovačič *(corresponding author)*
University of Maribor,
Faculty of civil engineering, transportation engineering and architecture
Smetanova 17, SI-2000, Maribor, Slovenia
E-mail: bostjan.kovacic@um.si

Boško Pribičević
University of Zagreb,
Faculty of geodesy
Kačićeva 26, HR-10000, Zagreb, Croatia
E-mail: bpribic@geof.hr

Rok Kamnik
University of Maribor,
Faculty of civil engineering, transportation engineering and architecture
Smetanova 17, SI-2000, Maribor, Slovenia
E-mail: rok.kamnik@um.si

Keywords

geodesy, geotehnics, monitoring, GNSS measurements, geology, deformation analysis, geodetic network

Abstract

Displacement research using the three-dimensional global navigation satellite system (GNSS) as part of geodetic monitoring is becoming the key investigation for establishing a cause-and-effect relationships model between external natural factors, on the one hand, and the criteria that describes the level of functionality and safety of the observed natural or artificial object, on the other, in cases of motion of an object in space and time. The main objective of the deformation analysis is to confirm the stabilities of the reference points of a geodetic network, which are used to determine the movements of the control points that are stabilized on the observed objects. The assumption about the stabilities of certain reference points must be based on reasonable grounds, underpinned by measurements and proven by numerical methods. This is one part of the results of the deformation analysis when determining the extent of the movements and deformations. To do this a transformation is used in which a comparison is made between the coordinates of the points for two separate epochs. On the basis of the estimated transformation parameters, possible movements can be concluded within the reference points, i.e., on whether the datum parameters have changed. After confirming the stability of the geodetic network the coordinate differences of identical points measured within the different time windows can be determined as displacements and/or deformations of an object. In this paper one viaduct was assessed through geology and tectonic activities and also a load test of the viaduct was performed. The viaduct is in a quite active region, but the load test showed that the bridge response to the load is as expected.

1 INTRODUCTION

Facilities that are usually the main issue within the context of deformation monitoring are often only an indirect indicator of the dynamic processes associated with the earth's surface and subsurface. Artificial structures are now being built from materials and in ways that tend to reduce the effects of the deformation of nature rather than to create the stress. Therefore, the primary task of deformation monitoring is to determine the stabilities of the areas of land before the construction.

The stability of a surface is related to the degree of slip and the landslide of rocks under the surface as well as the tectonic shifts deeper into the ground. Therefore, the necessary work prior to the commencement of constructing geotechnical structures, geological and tectonic investigations must be carried out, which frequently replaces the deformation monitoring and which focuses exclusively on the surface changes, and so are not launched

before, but possibly after the start, and most often at the completion, of the construction. The reasons for such an inconsistent sequence of events are usually economic. Landslides usually show themselves at an inclined position or orientation of the object, which may be:

- newly created changes that have not shown any signs of unexpected tilting in the past,
- changes due to a currently active landslide,
- the result of a proximity to areas with existing geodynamic events.

The objective of deformation monitoring is to determine facts about the stability of the observed object or the earth's surface in terms of the sizes of movements at certain points. In addition to stability, the importance of determining movements is in the evaluations of potential risks of built and natural objects to the environment and in particular to human life and its property. Therefore, determining the movements or deformations of natural and man-made structures is one of the more engaging and more demanding tasks of geodesy.

Deformation monitoring covers several temporal segments in terms of defining movements [1]:

- at the time before the appearance of natural forces that cause favourable conditions for the emergence of movements,
- during the operation of natural forces or the construction operation that realize movements of natural or man-made structures,
- completion of the construction operation, which also establish their long-term trends of movement for objects within a given area,
- when the natural forces end, i.e., during the straight influence of natural forces on the construction work, causing a relative annihilation of shifts or changes in the occurrences of the stagnations of these movements.

Deformation monitoring also covers several spatial segments in terms of determining movements:

- at the sites of the very origins of the phenomena of natural forces,
- at the place of the effective influence of natural forces or in the immediate vicinity of the facility itself,
- at all perceptual areas of influence of the natural forces,
- in places that are relatively stable
- indirectly also in areas that are absolutely stable.

Because of the fact that there are no absolutely stable points, especially on the earth's surface, the determination of displacements and deformations is virtually present in all scientific disciplines that in one way or another are related to the physical environment. The position

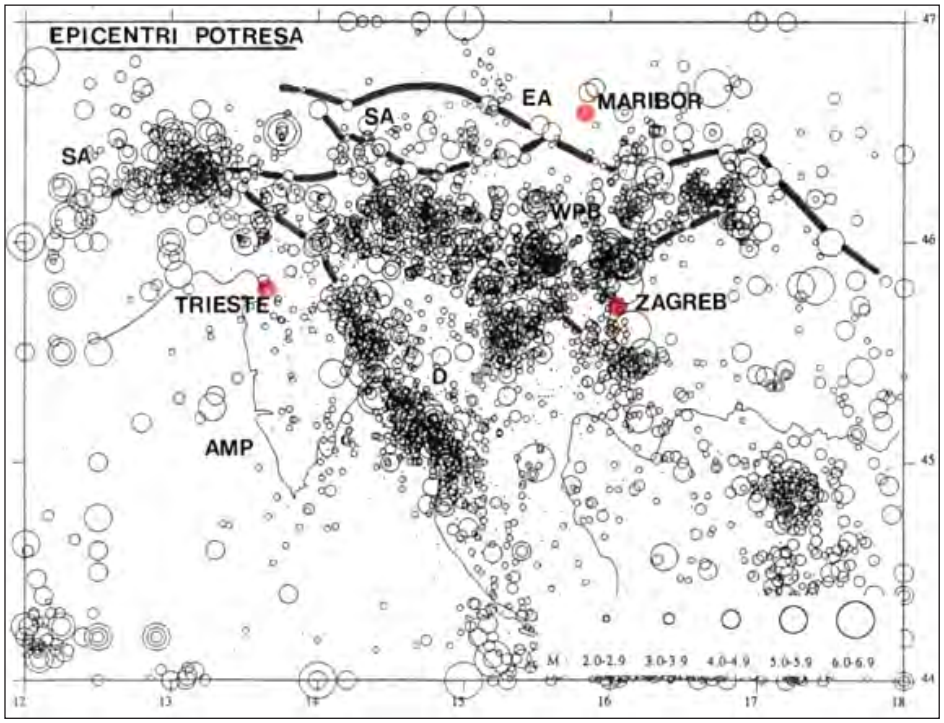

Figure 1. Earthquakes epicentres.

for determining movements when detecting landslides is determined by geomechanics in cooperation with surveyors to assess the suitability of the position due to the satellite's signal strength for deformation monitoring when using GNSS methods.

In order to collect the necessary data about the location of a viaduct, a detailed structural-geological mapping was needed. Thus, the most important structural data on the dynamics of a recent structural assembly was obtained and a series of outcrops of faults was discovered. The required measurements of the structural elements, which indicate the particular type, origin and location of faults in the structural part, were conducted, and the side faults of the movement and the related stress and deformation structures were found. Strict regulations of the position and the mutual relations of faults led to a study of additional satellite images. The collected data emphasize the determination of compression stress, its orientation and the angle of action. At each point of the measurement the orientation of the local compression stress is determined. Such a stress causes the deformation of parts of the structures. The orientation of the maximum compression stress is determined from several data. The maximum compression stress directly reveals the basic structural relationships, in fact the positions and movements of the complex of rock walls of different densities that forms the structural set.

Fig. 1 shows significant concentrations of epicentres in the peripheral parts of the Alps and the Dinarides and in the western part of the Pannonian Basin. The strongest earthquakes occur in the western part of the Southern Alps, in the northern part of the Dinarides and in the border region of the western and southern parts of the Pannonian Basin. Detailed locations of the epicentres sorted by magnitudes are shown in Fig. 2.

2 MONITORING WITH THE GNSS METHOD

In engineering practice, for monitoring the deformation of large structures (bridges, viaducts, hydro power plants, etc.), the technology of GNSS is generally used [2-6]. The method is also widely used for monitoring landslides [7-19]. Recently, the state geodynamic network is also more or less observed using this technology. Although GNSS allows positioning with an accuracy that is comparable to conventional methods, its use was restricted due to the need for observations of excessive length. With the development of instruments and, in particular, software, the observation time for the GNSS method was substantially reduced so that millimetre positioning can be obtained after less than 1 hour of observation. However, due to the elimination of the global movement of ground water and land masses

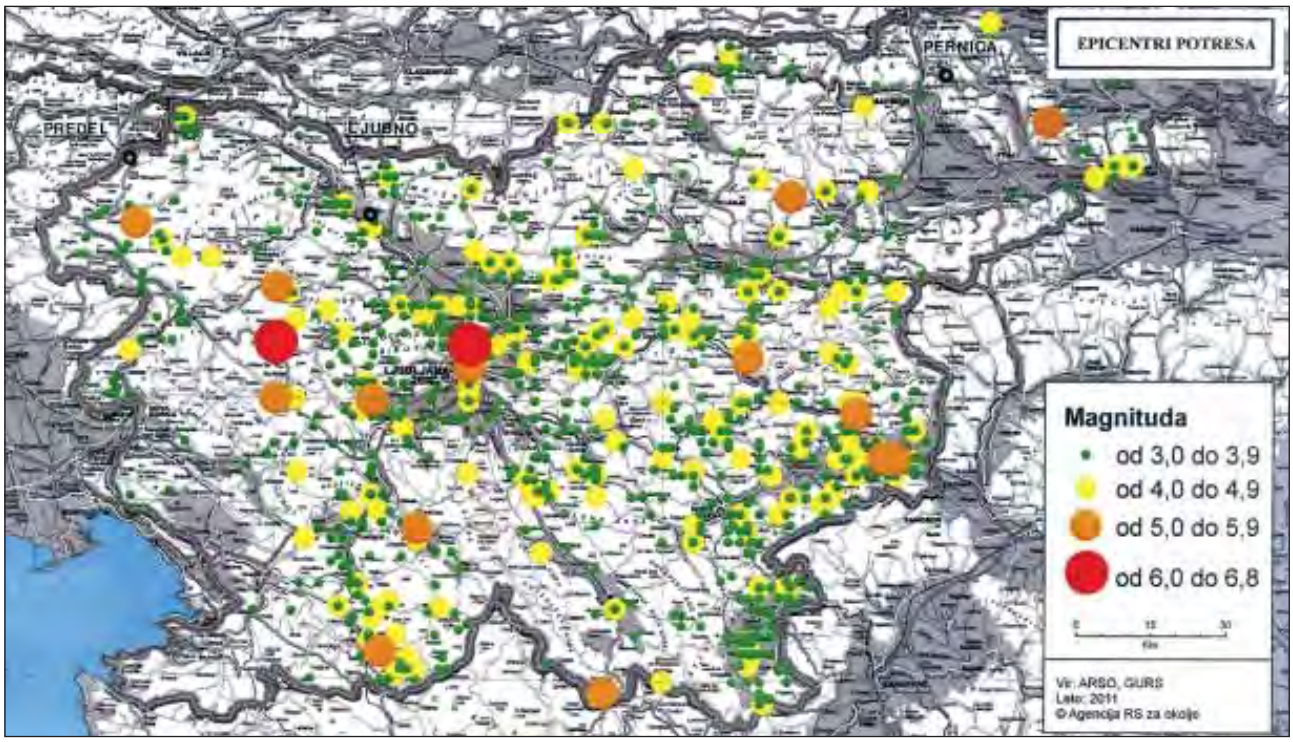

Figure 2. Earthquakes epicentres in Slovenia with the magnitudes (ARSO, GURS, 2011).

for the most accurate deformation analysis, longer times, which should last at least 24 hours, are recommended. [20]

Depending on the types of observed quantities and the means of the data processing, several methods for determining positions using the GNSS method can be as follows: absolute, code differentiated and the relative phase-shift method. In addition to the classical kinematic and RTK (real time kinematics) methods there are also the VRS (Virtual Reference Station) and PPP (Precise Point Positioning) methods. The latter is the most accurate method for determining absolute position, which can be considered as static or kinematic. For the purposes of geodetic monitoring only the static mode is used, which gives us mm accuracy. [21]

Research over recent years has demonstrated the usefulness of GNSS for a precise determination of three-dimensional positions for controlling dangerous natural phenomena. A detailed analysis of the dynamics of avalanches, especially for the purpose of installing a security system (functioning in real time), requires a combination of accurate positioning in three dimensions (a few mm) and a good time resolution (less than 1 hour). Monitoring landslides with the GNSS technique is usually used in several epochs, as a complement to conventional methods. For quality monitoring of the implementation of GNSS method it is necessary to determine the period of the time observations. Only in this way can a precision of one to two millimetres be obtained.

However, all the GNSS methods are based on the same geometric principle, i.e., that the position of a point in space is determined by the intersections of at least four spheres, whose radii represent the measured distance to the point of interest from these four points. These four points are satellites around the Earth (Fig. 3). The principle is similar to terestic trilateration: by the laws of plane geometry the position of new points can be obtained from the circle intersections, where the values of the radii are derived from distance measurements and the centres of the circles represent the positions of the instrument standing points, from which the distances are measured. In principle three measured distances (receiver–satellite) should be enough, but it is necessary to obtain a reference to at least 4 different satellites due to satellite and Earth movements and thus difficulties in determining the exact clock situation at the time of the transmission and reception of signals. Indeed, determining the timing of a received signal requires an extremely accurate clock in the receiver. These requirements may be minimized by using a time signal from the fourth satellite because only then can the difference between the times of the receptions signals from the individual satellites be measured.

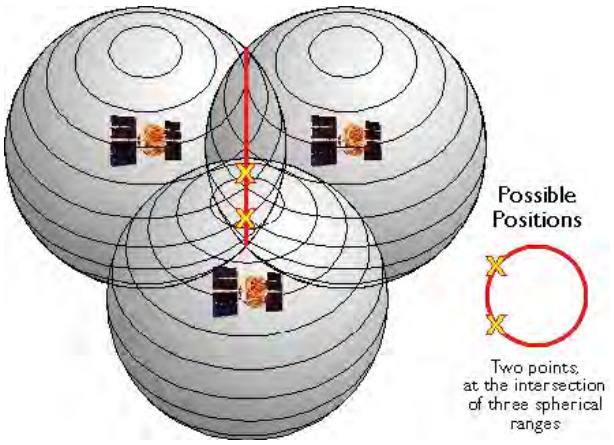

Figure 3. Two possible positions from observations from three satellites (https://www.e-education.psu.edu/natureofgeo-info/book/export/html/1796).

3 MEASUREMENT ACCURACIES

The GNSS method is a fairly new method that brings a lot of advantages over conventional methods. The positioning accuracy or determining the relative coordinates of a point with this method depends largely on the deployment of the satellites during the measurement and the quality of the performances of the observations. The accuracy could be easily described through evaluating the effects that cause errors in the measurement.

The main sources of error that contaminate the data obtained by GNSS technology can be divided into three groups:

- Error of signal propagation, tropospheric and ionospheric refraction, multipath (Fig. 4).
- Errors of the receiver: error during determination of the phase centre of the antenna, receiver system noise, neglected multipath effects, inaccurate coordinates of instrument standing point (known points),
- Errors in connection with the satellites: errors when determining the trajectories and positions of satellites.

If we succeed in minimizing the impacts or completely eliminate them during post processing then we can expect an accuracy of ± 2 mm in the horizontal direction and ± 3 mm in the vertical direction, of course for 24-hour observations.

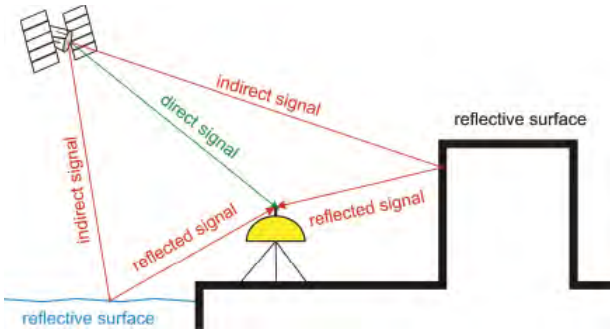

Figure 4. Signal multipath.

4 DETERMINING THE POSITION WITH GNSS OBSERVATIONS

On the basis of code or phase observations the absolute and relative positions of the GNSS receiver can be determined. The absolute position is determined only on the basis of the given positions of GNSS satellites in the selected coordinate system at the time of observation and with the observed distance between the satellite and the receiver. The relative position is determined relative to the known position of one or more points placed within the default coordinate system at the known satellite positions and the observed distance between the satellite and the receiver. Therefore, in both cases the basis for determining the position is the geometric distance between the satellite and the receiver. For this purpose, it is necessary to perform the linearization of the distance between the satellite and the receiver.

2.1 Linearization

Geometric distance $\rho_i^j(t)$ between the satellite j and the receiver i is:

$$\rho_i^j(t)=\sqrt{\left((X^j(t)-x_i)^2+(Y^j(t)-y_i)^2+(Z^j(t)-z_i)^2\right)} \equiv f(x_i,y_i,z_i) \quad (1)$$

The connection (1) between the geometric distance $\rho_i^j(t)$, the GNSS satellite position in the chosen coordinate system

$$r^j(t)=\left[(X^j(t),Y^j(t),Z^j(t)\right]^T \quad (2)$$

and the position of the GNSS receiver

$$r_i=\left[x_i,y_i,z_i\right]^T \quad (3)$$

is non-linear.

For the use of the geometric distance $\rho_i^j(t)$ in the linear mathematical model, the expression for geometric distance should be linearized. Knowing the approximate receiver position

$$r_{i0}=\left[(X_{i0},Y_{i0},Z_{i0}\right]^T \quad (4)$$

an approximate value for the geometric distance $\rho_{i0}^j(t)$ can be obtained using

$$\rho_{i0}^j(t)=\sqrt{\left((X^j(t)-x_{i0})^2+(Y^j(t)-y_{i0})^2+(Z^j(t)-z_{i0})^2\right)} \equiv f(x_{i0},y_{i0},z_{i0}) \quad (5)$$

The receiver position $r_i=\left[(X_i,Y_i,Z_i\right]^T$ when the known approximate position $r_{i0}=\left[(X_{i0},Y_{i0},Z_{i0}\right]^T$ can be calculated using

$$r_i=r_{i0}+\Delta r_i \quad \text{or}$$
$$x_i=x_{i0}+\Delta x_i,\ y_i=y_{i0}+\Delta y_i,\ z_i=z_{i0}+\Delta z_i \quad (6)$$

Therefore, the receiver position r_i is obtained by adding the vector of the known approximate position r_{i0} and the vector of unknown correction of approximate position

$$\Delta r_i=\left[(\Delta x_i,\Delta y_i,\Delta z_i\right]^T \quad (7)$$

The function:

$$f(r_i)=f(x_i,y_i,z_i) \quad (8)$$

is replaced with the function

$$f(r_i+\Delta r_i)=f(x_i+\Delta x_i,y_i+\Delta y_i,z_i+\Delta z_i) \quad (9)$$

Function (9) can be developed in a Taylor series at the point of the approximate receiver position:

$$f(x_i,y_i,z_i)\equiv f(x_{i0}+\Delta x_i,y_{i0}+\Delta y_i,z_{i0}+\Delta z_i)$$
$$=f(x_{i0},y_{i0},z_{i0})+\frac{\delta f(x_{i0},y_{i0},z_{i0})}{\delta x_{i0}}\Delta x_i+\frac{\delta f(x_{i0},y_{i0},z_{i0})}{\delta y_{i0}}\Delta y_i$$
$$+\frac{\delta f(x_{i0},y_{i0},z_{i0})}{\delta z_{i0}}\Delta z_i \quad (10)$$

In the Taylor series we keep only those parts where the component of correction Δr_i for the approximate vector is present in the first potency, otherwise the previous equation would be non-linear again for the vector of correction Δr_i for the approximate position.

Partial derivatives for Equation (10) can be calculated using (5):

$$\frac{\delta f(x_{i0},y_{i0},z_{i0})}{\delta x_{i0}}=-\frac{X^j(t)-x_{i0}}{\rho_{i0}^j(t)};\frac{\delta f(x_{i0},y_{i0},z_{i0})}{\delta y_{i0}}=$$
$$=-\frac{Y^j(t)-y_{i0}}{\rho_{i0}^j(t)};\frac{\delta f(x_{i0},y_{i0},z_{i0})}{\delta z_{i0}}=-\frac{Z^j(t)-z_{i0}}{\rho_{i0}^j(t)} \quad (11)$$

The partial derivatives in Eq. (11) represent the components of a single vector, directed from the satellite to the approximate receiver position. Inserting Eq. (11) in Eq. (10) we obtain:

$$\rho_i^j(t) = \rho_{i0}^j(t) - \frac{X^j(t) - x_{i0}}{\rho_{i0}^j(t)}\Delta x_i - \frac{Y^j(t) - y_{i0}}{\rho_{i0}^j(t)}\Delta y_i - \frac{Z^j(t) - z_{i0}}{\rho_{i0}^j(t)}\Delta z_i \quad (12)$$

Eq. (12) presents a linear connection between the geometric distance between the satellite and receiver $\rho_i^j(t)$ and corrections of the approximate positions $\Delta x_i, \Delta y_i, \Delta z_i$. This connection represents the starting equation for obtaining the GNSS position of the receiver, using the observations of pseudo distances between the GNSS satellite and the GNSS receiver [22].

5 GNSS MEASUREMENTS FOR THE DEMANDING AREA OF THE RAZDRTO REGION

The modern technology of GNSS measurements allows us to carry out observations without taking into account some important factors that have guided the work of surveyors for decades. These are primarily the weather conditions and the mutual visibility of geodetic points within a network. Planning a survey today is slightly different and depends on the intended method of GNSS surveying, and it is necessary to provide: the purpose, aim and accuracy of the measurement, the number of new and reference points, the time planning of satellite positions, the number and types of receivers, the duration of the observation, and the post processing methods in order to present the results properly.

The slope hills of Nanos near Razdrto are geologically very demanding, because there are a few landslides affecting the highway and the viaducts. When making a GNSS network it is necessary to take into account the general requirements for the implementation of GNSS observations. In particular, unimpeded GNSS signal reception, which means that within the vicinities of the points there should not be any physical obstacles. Sometimes this is hard to provide. However, since the GNSS method does not require mutual visibility of the points, the standings for the GNSS receiver can be placed in more accessible areas. The point needed to be observed but there is no signal that can be replaced with classical geodetic measurements. We can use different types of antennas and receivers (Fig. 5 a, b, c, d), but it is necessary to use the same equipment at the same point during different time epochs.

Figure 5. a-d: Different types of antennas and receivers.

Before observations on the route of a highway 50 points for the GNSS measurements were permanently stabilized on structures (retaining walls, viaducts, or pile walls) and in their proximity within a triangular design (Fig 6). For stabilization, concrete pillars, castes and metal plates were installed on the objects for the observation. Figure 4 shows the disposition of the measurement points on the object and its surroundings. The red points are GNSS standing points for 24-hour static observations and the blue points are classical points for total station observations.

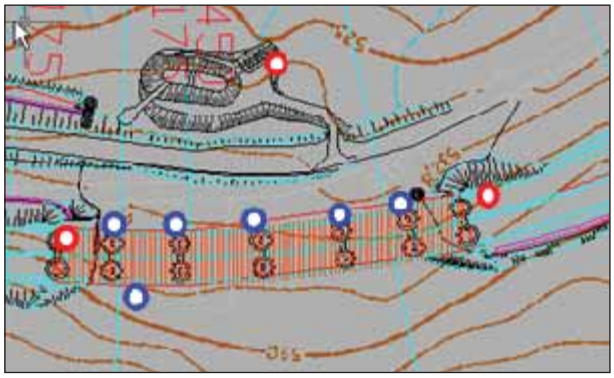

Figure 6. Example of different observation points on a viaduct.

Before the measurements, it was necessary to define the geodetic datum, which was provided with a set of given IGS points (International GNSS Service) that had known coordinates and speed vectors in the coordinate assembly ITRF2005 (International Terrestrial Reference Frame 2005) with high precision and accuracy. Further, four points of the Slovenian network of permanent stations of the SIGNAL (Slovenia Geodesy Navigation Area) were also taken in account during post processing, which is regarded as new point (with unknown coordinates). Points of the SIGNAL system have certain coordinates with lower accuracies so they could not be treated as given. SIGNAL points were selected so that they are the closest to the observed area, but none on the landslide area.

The post-processing of observations is carried out for each of the Julian day. Thus, it is necessary for each epoch to obtain two positions – two sets of coordinates for each point. On the basis of the differences in coordinates for each day the qualities of the observations and the post processing can be concluded.

The results of post-processing are the estimated coordinates of the points for each day with the corresponding accuracies. The accuracy assessment is based on these two variables since it represents a more realistic assessment of the accuracy. For each point obtained after post-processing in each epoch one set of coordinates in ITRF2005 coordinate system. Our goal is to present the coordinates of the points measured in each of the (new) state projections, i.e., the Transverse Mercator projection with corresponding accuracies. The transformation from ITRF2005 in the Slovenian state projection is carried out through the transformation to the ETRF89 coordinate assembly in which the positions are (depending on ITRF2005) reduced for movements of Eurasian tectonic plates. The positions in the ETRF89 points are then the basis for the conversion into the national cartographic projection.

It is assumed that the accuracies of the coordinates of points in the map projections and the precisions of geodetic coordinates in ITRF2005 are the same. Therefore, it is also assumed that with the transition to a state map projection (via ETRF89) the accuracies of the coordinates are not substantially altered. Table 1 shows some of the coordinates of the points on the Razdrto highway region in the Transverse Mercator projection with corresponding accuracies. The heights are "above sea level", which is obtained by ellipsoidal heights estimated via GNSS observations, reduced by the geoid height from the current geoid model of Slovenia. In Fig. 7, all the points are visible for that region.

Figure 7. 50 GNSS points on the Razdrto region.

Table 1. Measured coordinates and accuracies.

Point	Y [m]	Y [m]	H [m]	σ_Y [mm]	σ_X [mm]	σ_H [mm]
BAZ1	426090.0469	68720.5530	627.0367	1.85	0.87	1.93
BAZ2	418920.5057	77178.8702	112.9227	1.29	0.67	5.33
BO11	425303.9651	69705.3899	552.8670	1.74	3.06	4.38
BO13	425182.0177	69805.6379	545.7189	0.40	1.29	1.72
CER1	422999.0351	71962.3986	371.7237	0.98	1.11	1.20
CER2	423047.1678	71996.6312	385.2510	0.94	3.97	10.41
NPO2	422218.9394	72703.2487	333.3368	1.47	0.79	0.94
OZ41	420625.1227	74371.2769	250.1885	0.23	0.68	7.19
SUM1	424023.0656	70903.7784	455.9258	3.43	1.94	14.57
SUM2	423960.9856	70922.8898	429.2213	1.56	0.21	2.70
SUM3	423911.8404	71021.9010	439.5185	1.00	1.50	5.00
Z101	422617.1739	72155.0979	346.2361	1.46	1.32	2.15

From the table we can see that the data were captured with an accuracy of between 1 to 2 mm. At the points CER2 and SUM1 the determined positions were slightly less accurate because of the lower signal strength. This disadvantage was compensated for with conventional terestic measurements.

For any assessment of the possible movements of geodetic points it is necessary to determine the coordinates of points within several epochs. Based on a set of coordinates obtained in that way, it is necessary to assess the trends of potential changes in the coordinates of the points. The trends of coordinate changes can be well established only in the cases of quality coordinates or through high-quality time series of the coordinates of points. The graph below shows the changes in the coordinates of points in time for a one-year period for a point in Koper in the form of deviations from the mean of the individual coordinates for each point within the network. The coordinates in each epoch represent the deviations from this mean value with the specified standard deviation. The results are presented in graphical form (Fig. 8), where the positive axis ΔE represents the movements in an easterly direction, positive ΔN in the north and Δh in the vertical direction. Each vertical line represents the window within a certain epoch. If the mean value in every epoch is inter-connected, a line of movements can be obtained.

The changes of the coordinates of points can also be displayed in a plane map projection. Fig. 9 shows the estimated coordinates of the points for each epoch. However, according to the calculated standard deviations of the estimated coordinate points and methods used in the measurement points it is difficult to talk about the movements of points.

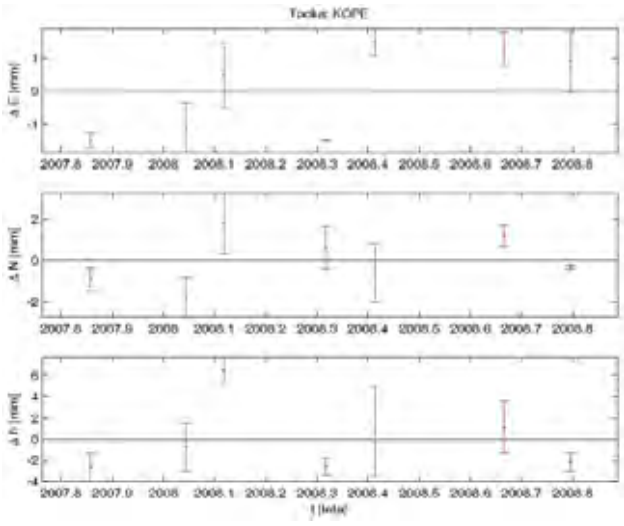

Figure 8. Coordinate differences over time.

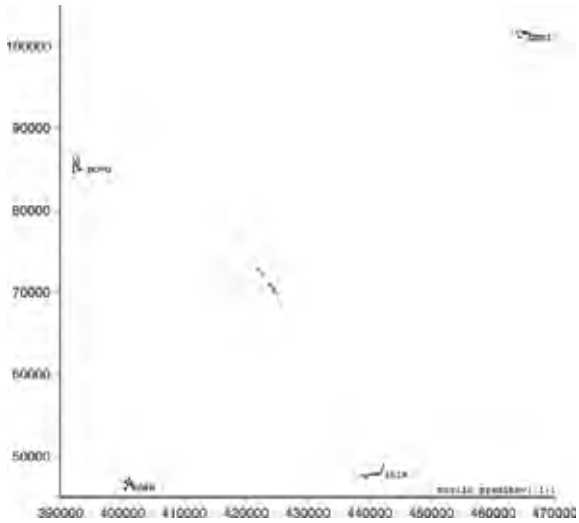

Figure 9. Movements of points for the SIGNAL points.

6 CONCLUSION

Measurements of ground movements using the GNSS method are used very often today. With better and better instrumentation, increased numbers of satellites and better software for data processing this method can obtain highly accurate results. There are not many areas that could have implemented long-term monitoring in Slovenia. So far, classical geodetic measurements have been performed more or less, but the method shows some weaknesses, like shifts of station points and connecting points, weather conditions, invisibility between points, and large mutual distances.

The GNSS method is ideal because it does not need stable positioning points and mutual visibility. Major emphasis is given to the deformation analysis of measurements. In general, a deformation analysis is a set of methods described for the detection and evaluation of the movements and the deformations of natural or man-made structures. The focus is primarily on the concept of data processing so that the deformation analysis frequently indicates, more or less, a procedure for determining movements using appropriate and relevant analytical approaches. It denotes the procedure of processing the measurement results. Geodetic deformation monitoring is thus a wider concept, covering all stages from planning and establishing a system of continuous operation, data processing, analysis and the presentation of results, while under the deformation analysis we understand the processing of measured data and analysing them. The analysis of GNSS data for the purpose of monitoring the movement of soil should also use the knowledge of statistics, geomechanics, civil engineering and geology as well

as additional knowledge of geophysics, geodynamics, and geodesy. The results showed that the GNSS method can cover wider areas in which we need to provide a "clean" signal and all-day surveillance. Based on the results so far we can suggest that the method is very suitable for the long-term monitoring of soil movements for already built objects and for the observation of mutual positions.

In this paper one viaduct was assessed through geology and tectonic activities and also a load test of the viaduct was performed. The viaduct is in a quite active region but the load test showed that the bridge's response to the load is as expected.

REFERENCES

[1] Savšek Safič, S. 2002. Optimalna metoda določanja stabilnih točk v deformacijski analizi, doctoral thesis, UL, FGG.

[2] Yi, T.H., Li, H.N., Gu, M. 2013. Experimental assessment of high-rate GPS receivers for deformation monitoring of bridge, Measurement 46, 420-432.

[3] Moschas, F., Stiros, S. 2011. Measurement of the dynamic displacements and of the modal frequencies of a short-span pedestrian bridge using GPS and an accelerometer. Engineering structures 33, 10-17. http://dx.doi.org/10.1016/j.engstruct.2010.09.013

[4] Handayani, H.H., Yuwono Taufik M. 2015. Preliminary study of bridge deformation monitoring using GPS and CRP (case study: Suramadu Bridge). Procedia Environmental Sciences 24, 266-276.

[5] Kaloop, M.R., Li, H. 2011. Sensitivity and analysis GPS signals based bridge damage using GPS observations and wavelet transform. Measurement 44, 927-937.

[6] Elnabwy, M.T., Kaloop, M.R., Elbeltagi, E. 2013. Talkha steel highway bridge monitoring and movement identification using RTK-GPS technique. Measurement 46, 4282-4292.

[7] Du, J.C., Teng, H.C. 2007. 3D laser scanning and GPS technology for landslide earthwork volume estimation. Automation in Construction 16, 657-663. doi:10.1016/j.autcon.2006.11.002

[8] Chadwick, J., Dorsch, S., Glenn, N., Thackray, G., Shilling, K. 2005. Application of multi-temporal high-resolution imagery and GPS in a study of the motion of a canyon rim landslide. ISPRS Journal of Photogrammetry & Remote Sensing 59, 212-221.

[9] Squarzoni, C., Delacourt, C., Allemand, P. 2005. Differential single-frequency GPS monitoring of the La Valette landslide (French Alps). Engineering Geology 79, 215-229. doi:10.1016/j.enggeo.2005.01.015

[10] Mora, P., Baldi, P., Casula, G., Fabris, M., Ghirotti, M., Mazzini, E., Pesci, A. 2003. Global Positioning Systems and digital photogrammetry for the monitoring of mass movements: application to the Ca' di Malta landslide (northern Apennines, Italy). Engineering Geology 68, 103-121. doi:10.1016/S0013-7952(02)00200-4

[11] Rizzo, V. 2002. GPS monitoring and new data on slope movements in the Maratea Valley (Potenza, Basilicata). Physics and Chemistry of the Earth 27, 1535-1544. doi:10.1016/S1474-7065(02)00174-2

[12] Brückl, E., Brunner, F.K., Kraus, K. 2006. Kinematics of a deep-seated landslide derived from photogrammetric, GPS and geophysical data. Engineering Geology 88, 149-159. doi:10.1016/j.enggeo.2006.09.004

[13] Baldi, P., Cenni, N., Fabris, M., Zanutta, A. 2008. Kinematics of a landslide derived from archival photogrammetry and GPS data. Geomorphology 102, 435-444. doi:10.1016/j.geomorph.2008.04.027

[14] Benoit, L., Briole, P., Martin, O., Thom, C., Malet J.P., Ulrich, P. 2015. Monitoring landslide displacements with the Geocube wireless network of low-cost GPS. Engineering Geology 195, 111-121. doi:10.1016/j.enggeo.2015.05.020

[15] Peyret, M., Djamour, Y., Rizza, M., Ritz, J.F., Hurtrez, J.E., Goudarzi, M.A., Nankali, H., Chéry, J., Dortz, K. Le, Uri F. 2008. Monitoring of the large slow Kahrod landslide in Alborz mountain range (Iran) by GPS and SAR interferometry. Engineering Geology 100, 131-141. doi:10.1016/j.enggeo.2008.02.013

[16] Zhu, X., XU, Q., Zhou, J., Deng, M. 2012. Remote Landslide Observation System with Differential GPS. Procedia Earth and Planetary Science 5, 70-75.

[17] Coe, J.A., Ellis, W.L., Godt, J.W., Savage, W.Z., Savage, J.E., Michael, J.A., Kibler, J.D., Powers, P.S., Lidke, D.J., Debray, S. 2003. Seasonal movement of the Slumgullion landslide determined from Global Positioning System surveys and field instrumentation, July 1998–March 2002. Engineering Geology 68, 67-101. doi:10.1016/S0013-7952(02)00199-0

[18] Gili, J. A., Corominas, J., Rius, J. 2000. Using Global Positioning System techniques in landslide monitoring. Engineering Geology 55, 167-192. doi:10.1016/S0013-7952(99)00127-1

[19] Moss, J. L. 2000. Using the Global Positioning System to monitor dynamic ground deformation networks on potentially active landslides. JAG 2, 1.

[20] Malet, J.P., Maquaire, O., Calais, E. 2002. The use of Global Positioning System techniques for the continuous monitoring of landslides: application to the Super-Sauze earthflow (Alpes-de-Haute-Provence, France). Geomorphology 43, 33-54. doi:10.1016/S0169-555X(01)00098-8

[21] Kozmus, K., Stopar, B. 2003, Načini določanja položaja s satelitskimi tehnikami. Geodetski vestnik 47, 4.

PRIMERJAVA LINEARNE IN NELINEARNE SEIZMIČNE INTERAKCIJSKE ANALIZE PREDOR-TLA

Elefterija Zlatanović *(vodilni avtor)*
University of Niš,
Faculty of Civil Engineering and Architecture
Aleksandra Medvedeva 14, 18000 Niš, Srbija
E-pošta: elefterija2006@yahoo.com

Marina Trajković-Milenković
University of Niš,
Faculty of Civil Engineering and Architecture
Aleksandra Medvedeva 14, 18000 Niš, Srbija
E-pošta: trajmarina@gmail.com

Dragan Č. Lukić
University of Novi Sad,
Faculty of Civil Engineering and Architecture
Kozaračka 2a, 24000 Subotica, Srbija
E-pošta: drlukic.lukic@gmail.com

Stanko Brčić
University of Belgrade,
Faculty of Civil Engineering
Bulevar kralja Aleksandra 73, 11000 Beograd, Srbija
E-pošta: stanko.brcic@gmail.com

Vlatko Šešov
University of Skopje,
Institute of Earthquake Engineering and Engineering Seismology – IZIIS
Todor Aleksandrov 165, 1000 Skopje, Makedonija
E-pošta: vsesov@gmail.com

Ključne besede

predor okroglega prereza, linearno / nelinearno obnašanje tal, model nosilec-vzmet, ravninsko-deformacijski pogoji, poenostavljena dinamična analiza s končnimi elementi, interakcija tla-konstrukcija

Izvleček

Članek preučuje potresne učinke na interakcijo predor--tla. Za to so bile izvedene dvodimenzionalne numerične analize s pomočjo programa ANSYS. V študiji je uporabljen potresno obremenjen združeni model nosilec-vzmet, ki je simuliran pod čistimi strižnimi pogoji in določen z analizo odziva tal s prostim poljem z uporabo programske kode EERA. Lastnosti materiala tal so obravnavane tako linearno kot nelinearno. Rezultati, dobljeni z linearnimi dinamičnimi analizami so primerjani z v praksi znanimi analitičnimi elastičnimi rešitvami. Primerjani so tudi rezultati linearnih in nelinearnih analiz, za oba primera so ovrednotene pomembne razlike ter pomembni dejavniki, ki vplivajo na interakcijo predor-tla.

A COMPARISON OF LINEAR AND NONLINEAR SEISMIC TUNNEL–GROUND INTERACTION ANALYSES

Elefterija Zlatanović *(corresponding author)*
University of Niš,
Faculty of Civil Engineering and Architecture
Aleksandra Medvedeva 14, 18000 Niš, Serbia
E-mail: elefterija2006@yahoo.com

Marina Trajković-Milenković
University of Niš,
Faculty of Civil Engineering and Architecture
Aleksandra Medvedeva 14, 18000 Niš, Serbia
E-mail: trajmarina@gmail.com

Dragan Č. Lukić
University of Novi Sad,
Faculty of Civil Engineering and Architecture
Kozaračka 2a, 24000 Subotica, Serbia
E-mail: drlukic.lukic@gmail.com

Stanko Brčić
University of Belgrade,
Faculty of Civil Engineering
Bulevar kralja Aleksandra 73, 11000 Belgrade, Serbia
E-mail: stanko.brcic@gmail.com

Vlatko Šešov
University of Skopje,
Institute of Earthquake Engineering and Engineering Seismology – IZIIS
Todor Aleksandrov 165, 1000 Skopje, Republic of Macedonia
E-mail: vsesov@gmail.com

Keywords

circular tunnel, linear/nonlinear soil behaviour, beam–spring model, plane-strain conditions, simplified dynamic FE analysis, soil–structure interaction

Abstract

In order to study the effects of a seismically induced tunnel–ground interaction, two-dimensional numerical analyses are performed using the sofware ANSYS. The study employs a coupled beam–spring model subjected to earthquake loading that is simulated under pure shear conditions and determined by a free-field ground-response analysis using the code EERA. The properties of the soil material are considered as both linear and nonlinear. The results obtained by linear dynamic analyses are compared with state-of-practice analytical elastic solutions. A comparison of the results of both linear and nonlinear analyses is also performed, and significant differences, as well as important factors influencing the tunnel–ground interaction for both cases, are evaluated.

1 INTRODUCTION

A reliable evaluation of the seismic response of tunnel structures is crucial in civil and earthquake engineering. As the structural design has shifted to the performance design in recent years, the seismic design, accounting for the soil–structure interaction (SSI) effects, becomes more important. The presence of a tunnel structure considerably modifies the free-field ground motion leading to a different seismic response of the tunnel lining. This phenomenon is related to the combined effects of the *kinematic interaction* and the *dynamic (inertial) interaction*. The kinematic interaction is influenced by the inability of a structure to match the free-field deformation. The dynamic interaction is caused by the existence of a structural mass making the effect of inertial force on the response of the surrounding environment, in which case dynamic forces in the tunnel's structure cause the tunnel to deform the soil, thus producing stress waves that travel away from the structure (radiation damping).

The response of the tunnel, which is confined by the surrounding rock or soil, is basically governed by the ground deformation, and the level of the tunnel deformation will depend on the stiffness of the tunnel relative to the stiffness of the surrounding ground. Therefore, an analysis of the tunnel–ground interaction, concerning both the tunnel and the ground stiffness, is required in order to find an accurate tunnel response.

Besides the ratio of the ground and the lining stiffness, another aspect that sensibly affects the response of the tunnel is the shear-stress transmission at the ground–lining interface. Numerous approaches are frequently based on the assumption that the soil behaves in a linear elastic manner and is perfectly bonded to a structure. However, the contact between the soil and the structure is usually imperfect, since slippage as well as separation

often occur in the interface region. Furthermore, the soil region immediately adjacent to the tunnel structure can experience an extensive strain level, thus causing the coupled soil–tunnel system to behave in a nonlinear manner. The soil–structure interaction effects decrease as the relative displacements between the soil and the structure increase.

In many practical situations, the condition of *partial slip* exists. Nevertheless, solutions are usually derived for the two extreme contact conditions: full-slip and no-slip. *The full-slip condition (smooth contact, sliding contact)* between the lining and the ground assumes equal normal displacements and unequal tangential displacements of the medium and lining at the common interface (i.e., no shear stress transmission and no tangential shear force exist). This assumption is used in order to obtain the extreme values of the bending moments and the shear forces in the tunnel lining, and is only valid for the case of a very soft soil or excitations of high intensity. *The no-slip condition (perfect contact, rigid contact, rough interface)* considers equal displacements of the medium and the lining at the common interface (i.e., the continuity of stresses and displacements, and no relative shear displacements exist), and is being adopted to find the maximum values of the thrust acting in the lining. It is usual practice to consider both of the extreme cases and apply the more critical one. For the case of unequal displacements of the structure and the surrounding ground, or the existence of a locally concentrated mass in the structure, the effect of inertia must not be overlooked. Nowadays, intensive studies are being performed regarding the effect of the interface friction on the tunnel liner's internal forces due to the seismic S- and P-wave propagation [1].

2 THEORETICAL BACKGROUND

The seismic response of circular tunnels has been the focus of a number of studies. Owen and Scholl [2] proposed the response of circular tunnels to an earthquake action to be described by axial compression/extension, longitudinal bending, and ovaling. Considering these deformation modes, it is suggested that the most critical deformation pattern of a circular tunnel is the ovalisation of the cross-section caused by the shear S-waves propagating in the planes perpendicular to the tunnel axis. Therefore, a number of simplified approaches have been developed to quantify the seismically induced ovaling effect on circular tunnels, which is commonly modelled as a two-dimensional, plane-strain condition. The so-called *free-field deformation approach* [3, 4] is based on the theory of wave propagation in an infinite, homogeneous, isotropic, elastic medium, and does not account for any soil–structure interaction effect. In addition, there are analytical solutions after various authors [5-11] that represent the so-called *soil–structure interaction approach*. They are based on the theory of an elastic beam on an elastic foundation, which takes into account the soil–structure interaction (SSI) effects in a quasi-static manner, ignoring any inertial interaction effect. An extensive review of the aforementioned methods can be found in Hashash et al. [12]. A simple modification in order to improve the accuracy of the widely used closed-form elastic solutions considering the kinematic interaction between the tunnel and the ground is suggested by Billota et al. [13]. In addition, expressions for earthquake-induced displacements and the accumulated internal lining forces related to circular tunnels embedded in a rock medium for near-fault conditions are developed by Corigliano et al. [14]. A set of closed-form expressions to calculate the circular tunnel liner's forces due to compressional seismic P-wave propagation is presented in [15]. Both no-slip and full-slip interface conditions were considered and the obtained results were compared and verified against dynamic numerical analyses.

These two approaches include various sub-methods characterised by different levels of approximation depending on the design stage, a knowledge of the geologic setting, and geotechnical parameters. Concerning the types of analyses, they can be grouped into three categories, i.e., *pseudo-static, simplified dynamic*, and *full (detailed) dynamic analysis*, regarding the increasing levels of complexity in the analytical models, soil characterisation, and a description of the seismic input. In pseudo-static methods, the ground–tunnel analysis is uncoupled. The seismic input is reduced to the peak-strain amplitude, computed by simplified formulas based on simple assumptions of harmonic plane S-wave propagation in a homogeneous, isotropic, elastic medium, and then considered to be acting on the tunnel lining in static conditions. In this way the effects of tunnel shape and stiffness on the seismic ground behaviour are ignored. In a simplified dynamic analysis, the soil straining in the range of depths corresponding to the tunnel section, between the tunnel crown and the invert, is computed through a free-field, one-dimensional, site seismic response (SSR) analysis, and then applied to the tunnel lining, again in pseudo-static conditions. In such a way both the acceleration time history and the site characteristics are taken into account, whereas the kinematic soil–structure interaction is still neglected. Moreover, the effects of compressional waves are also neglected, as only the shear waves are considered, which propagate in vertical planes inducing shear strain. In a

full dynamic analysis, the force increments in the lining due to an earthquake are directly obtained as an output of the numerical modelling (such as the dynamic finite element or finite difference methods) adopted for the simulation of the shaking of the coupled ground–tunnel system. In this way, besides the acceleration time history and the site characteristics, both the kinematic and dynamic interactions are also taken into consideration. All the above-presented analyses are reviewed by Billota et al. [16].

The mechanical behaviour of the soils can be relatively complex, even under static conditions, and particularly under seismic impact, in which case the soil is cyclically loaded. Accordingly, there was a need to modify the linear approach in order to provide a reasonable estimation of the ground response to an earthquake action. Experimental results have suggested that some energy is dissipated, even at a very low strain level, thus indicating that the damping ratio of a soil is never zero. It is also suggested that both the soil's shear modulus and the damping ratio are dependent on the shear-strain level. To describe the degradation of the shear modulus and the increase of the damping ratio along with the shear-strain level increase, different curves were proposed in the literature for various types of soils [17]: fine-grained soils, sand, and gravel. The previously mentioned soil models are *equivalent linear models*, and are the simplest and most commonly used. However, they have a limited ability to represent the most significant aspects of soil behaviour under cyclic loading conditions. Equivalent linear models represent only an approximation of the actual nonlinear behaviour of the soil. For that reason they are not proposed to be used directly for problems concerning permanent ground deformation or failure, because they imply that the strain always returns to zero after the cyclic loading. Consequently, since a linear material has no limiting strength, it is not possible to achieve soil failure. And yet, the assumption of linearity allows a very efficient class of constitutive models to be used for ground-response analyses, particularly for problems involving low strain levels such as stiff soil deposits and weak input motions.

Considering the complexity and the high computational cost of dynamic FE analyses, the present study employs simplified dynamic analyses to investigate the seismic response of tunnels that are interacting with the surrounding environment. Although such simplified methods cannot properly simulate the soil stiffness and strength changes that take place during an earthquake and they ignore any dynamic soil–structure interaction effects, they give a reasonable evaluation of the seismic loads regarding an initial estimation of the strains and deformations in a tunnel [18].

A beam–spring model was chosen for the analyses, since, despite its simplicity, it allows relative contributions of partial influences in the total internal lining forces, such as the earthquake-induced displacements, soil shear stress, and tunnel section inertia, to be studied separately.

As noted previously, various analytical studies have suggested that the most critical deformation of a circular tunnel is the ovaling of the cross-section that is caused by shear waves that propagate in planes perpendicular to the tunnel axis, which implies a stress concentration at the tunnel's soffits (shoulder and knee locations of the lining). Therefore, the models were subjected to simple shear conditions obtained by means of a one-dimensional site seismic response (SSR) analysis that neglects the effects of the tunnel's shape and stiffness on the seismic behaviour of a soil. In addition, this analysis ignores the effects of all but vertically propagating shear waves. The free-field soil deformations caused by the wave propagation are calculated for both linear and nonlinear soil behaviour. Thereafter, the calculated soil displacements were applied to beam–spring models in order to simulate earthquake-induced ovalisation under simple shear conditions. Furthermore, the computed deformations are used to calculate the seismic force increments in the tunnel lining by means of closed-form elastic solutions after Wang [9] and Penzien (2000) [11]. The obtained numerical results from the simplified dynamic linear analysis were compared with the analytical solutions. Lastly, significant differences between the linear and nonlinear tunnel–ground interaction analyses were estimated and summarised.

3 GROUND CONDITIONS AND TUNNEL CHARACTERISTICS

The analytical and numerical simulations were performed on a virtual example considering idealised tunnel and ground conditions. The tunnel structure of a circular cross-section is placed within a 30-m-thick soil deposit of medium-dense sand overlying a relatively stiff bedrock, with an overburden cover of 12 m and an axis depth of 15 m. An external tunnel radius of 3.0 m was used, whereas the thickness of the lining is 0.3 m. The physical properties of the tunnel lining and the ground material surrounding the tunnel are reported in Fig. 1.

The shear wave velocity profile $V_s(z)$, illustrated in the given figure as well, was required for a one-dimensional, nonlinear, seismic site reponse analysis completed using the software EERA. The dashed line represents an average value of the shear wave velocity within the soil medium needed for the purpose of the 1D linear SSR analysis.

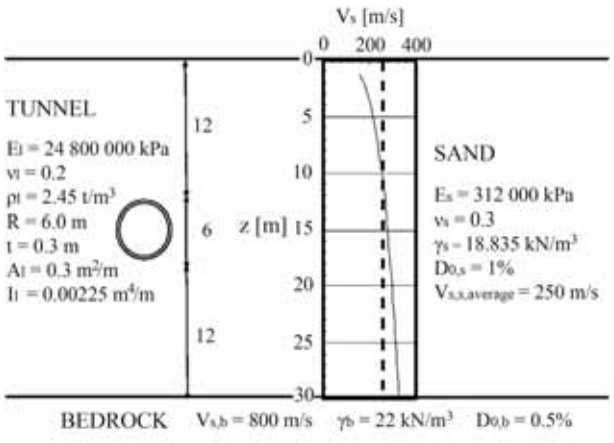

Figure 1. Soil profile and tunnel characteristics (reproduced after Billota et al., 2007 [16]).

4 DESCRIPTION OF THE NUMERICAL MODELS

The present study employs a two-dimensional, coupled beam–spring model using the finite-element-based simulation platform ANSYS [19] to examine the soil–tunnel structure interaction phenomenon. The problem has been analysed and the results of both linear and nonlinear analyses are then compared.

The following assumptions are adopted in the analyses:

1) The soil material surrounding the tunnel is assumed to be a homogeneous and isotropic half-space;
2) The tunnel lining is assumed to behave in a linear elastic manner, whereas the properties of the soil material are considered to be both linear and nonlinear;
3) Two-dimensional, plane-strain analyses were performed, thus assuming the uniform nature of the tunnel's structure and the soil deposit throughout the tunnel's length.

4.1 Discrete coupled beam–spring model (software ANSYS)

The ANSYS 2D discrete model consists of 36 two-noded Timoshenko beam elements (BEAM188) for the tunnel lining and 72 two-noded bi-linear spring elements (COMBIN14) for the soil, placed in the radial (36) and tangential directions (36 elements). At each node there are 3 DOF (*Ux*, *Uy*, *ROTz*) for the beam, and 1 DOF (*Ux*) for the spring elements. The main purpose of the spring elements is the ground–structure interaction modelling, completed by supports placed radially and tangentially (discrete contact). The tied-degrees-of-freedom boundary condition was applied along the interface of the tunnel's lining and the surrounding soil-springs, in order to constrain the nodes of both beam and spring elements to deform identically for the purposes of a no-slip condition simulation, assuming compatible displacements of the lining and the ground [20].

Prior to all the 2D simplified dynamic analyses presented in this study, a static analysis was undertaken in order to check the model for static conditions as well. A static analysis should be performed in order to verify the safety of the tunnel under static conditions, meaning that the tunnel's structure should be stabilised by a balance between the weight of the overburden cover, the reaction force from the ground below, and the lateral soil pressure (Fig. 2(a)).

The emphasis on the inertial effects of surface structures (Force Method) is in stark contrast to the design of underground structures, in which case the seismic design loads are characterised in terms of deformations and strains imposed on the structure by the surrounding ground. Thus, the seismic response of underground structures is controlled by the earthquake-induced ground strain field and its interaction with the structure. This led to the development of design methods such as the Seismic Deformation Method that explicitly considers the seismic deformation of the ground [21].

In the simplified dynamic analysis, on the basis of the seismic deformation method, a beam–spring model illustrated in Fig. 2(b) was used. The interaction between the soil and the tunnel was simulated by a coupled-type interaction spring consisting of a radial and a tangential soil spring. According to the seismic deformation method, seismic forces acting on the beam–spring model were assumed to be the result of the seismically induced ground displacements, the ground shear stress, and the inertial force. The maximum relative displacement between the top and the bottom of the tunnel's cross-section was considered in the analysis.

For the purpose of the given analyses, the properties of soil springs were determined after expressions given by a number of authors: St. John and Zahrah [4], Matsubara and Hoshiya [22], ALA-ASCE [23], and Verruijt [24]. After conducting a series of numerical tests, the value of the soil spring stiffness that was finally adopted in the analyses was according to ALA-ASCE [23] (Table 1). It was the smallest obtained value for the soil spring constants, and the only one for which it was possible to successfully simulate the elastic subgrade reaction in the static analysis. In this way, the flexible surrounding medium was modelled, in which case the soil–tunnel

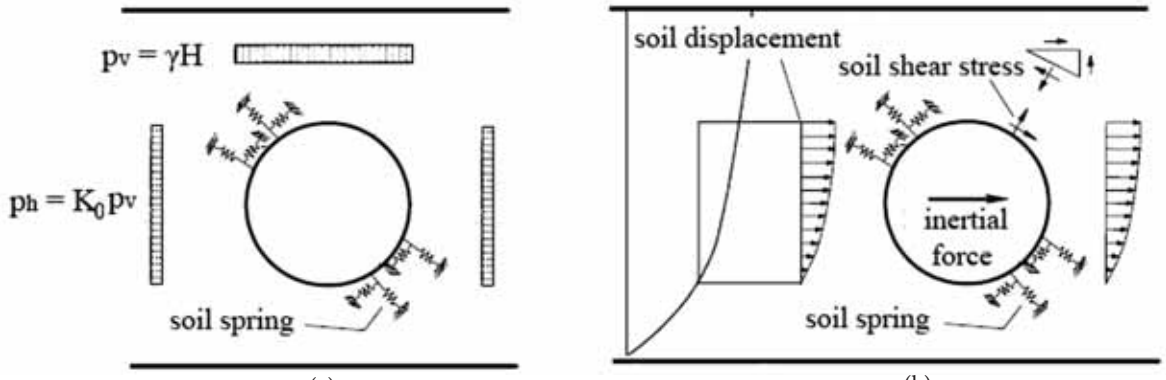

Figure 2. Beam–spring model: (a) static analysis and (b) dynamic analysis. ((b) reproduced after Mizuno and Koizumi, 2006 [21]).

Table 1. Bi-linear spring properties considered in the numerical analyses.

Yield force per unit length of tunnel (kN/m)	Yield displacement (mm)
3085.173	150

interaction is the most pronounced and applying the springs in the model is meaningful. Furthermore, for large frequencies the spring is much more flexible, resulting in smaller values of the spring constant. Therefore, the chosen spring coefficient simulates the soil in a proper way under both static and dynamic conditions.

4.2 One-dimensional SSR analysis (code EERA)

The SSR analyses were carried out using the code EERA [25], which stands for Equivalent-linear Earthquake site Response Analysis. The input of the data and the output of the results are completely integrated with the program MS Excel. This code is intended to perform analyses for linear and equivalent linear stratified subsoils. The code is based on the assumption of vertically propagating, horizontal shear SH-waves through a horizontally layered soil deposit. The horizontal soil layers are represented by a Kelvin–Voigt solid, in which case the soil column is discretised into individual layers using a multi-degree-of-freedom, lumped-parameter model. Shear moduli and viscous damping characterise the properties of the soil layer.

The equivalent linear approach is based on the assumption that both the shear modulus and the damping ratio depend on the shear-strain level, in order to account for some types of soil nonlinearities. For a given input excitation and an initial evaluation of the shear modulus and the damping values, an effective shear strain equal to 65% of the peak strain [17] is computed for a given soil layer. Based on the modulus degradation and the damping curves, revised values of the shear modulus and damping are then obtained. The solution process is developed as a frequency-domain (FD) analysis and an iterative scheme is required to approach a converged solution.

The EERA code allows the bedrock to be modelled as rigid, by choosing the option "inside", or as elastic, by assigning it as the last layer and selecting the option "outcrop". For the purpose of the signal transformation from the outcropping rock to the bedrock, placed at the bottom of the soil layer, the code applies a proper transfer function to the input signal. A computation procedure for determining the bedrock motion from a known free-surface motion is known as deconvolution [17].

The source of the dynamic excitation in this research is the acceleration record of the Hyogoken Nanbu (Kobe) Earthquake in Japan in 1995. The seismic signal of the great Kobe Earthquake has been considered for the reason that this event was the most devastating to underground facilities in recorded history. Strong ground-motion data are generally not available at the depths of concern for tunnel structures, so the development of the required ground motions needs to incorporate attenuation effects (the ground motion decreasing with the depth). The surface acceleration record was applied at the outcropping rock and then transformed to the bedrock, placed at the bottom of the soil layer, by applying a suitable transfer function to the input signal (deconvolution).

Fig. 3 illustrates the acceleration time history that was employed in all the SSR analyses. The peak value of the input-acceleration time history is 0.821g (8.05 m/s^2) occurring approximately 8.5 s after the onset of the excitation.

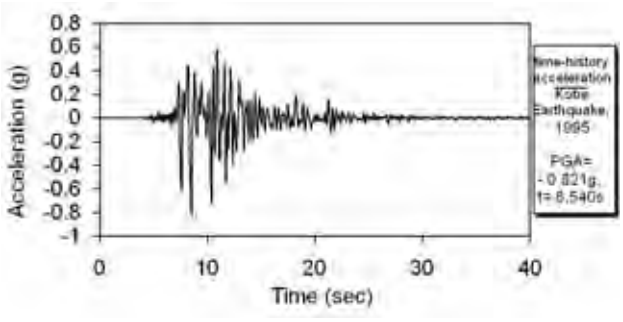

Figure 3. Surface-acceleration record of the 1995 Kobe Earthquake in Japan.

The acceleration, the shear stress, and the strain induced by the seismic waves at the tunnel's depth were calculated using a free-field, one-dimensional SSR analysis. The average soil shear strain, γ_{ave}, as the design free-field shear strain of the soil in the seismic analysis of tunnel structures in the range of depths between the tunnel crown and the invert [26], as well as the corresponding soil shear stress, τ_{ave}, were calculated. The soil straining, i.e., the displacements induced by an earthquake excitation, are then applied through soil springs to the tunnel section of the ANSYS's beam–spring model in a pure shear condition, whereas the soil shear stress was applied directly to the tunnel's lining. In such a way, both the acceleration time history and the site characteristics are taken into account, considering the kinematic tunnel–soil interaction in an approximate way. However, the dynamic soil–structure interaction is ignored.

5 COMPARISON OF THE LINEAR AND EQUIVALENT-LINEAR 1D SSR ANALYSIS RESULTS FOR A SOIL COLUMN

In the present analyses, the ground conditions and the soil behaviour are modelled according to Fig. 1. The free-field soil deformations caused by the wave propagation are calculated for the cases of the linear elastic and nonlinear types of soil behaviour.

In the linear analysis (Fig. 4(a)) it is assumed that the **shear-wave propagation velocity** is constant. For the given soil column, an average value of the shear-wave velocity profile of 250 m/s was used throughout the analysis. In the equivalent-linear analysis, the shear-wave velocities change with the depth of the soil column, as illustrated in Fig. 4(b).

When it comes to a **soil's shear modulus**, in the linear analysis it is assumed to be constant, regarding a constant value of the shear-wave velocity along the soil-

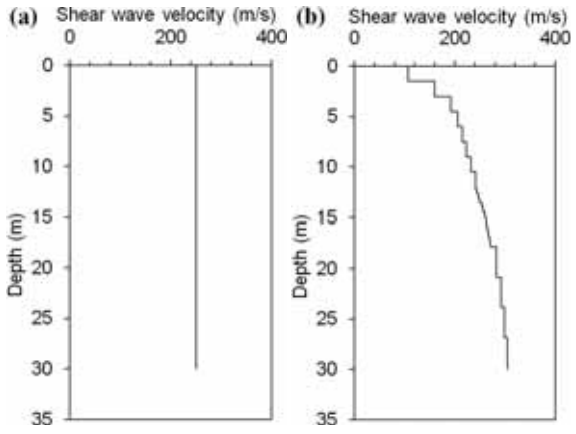

Figure 4. Shear wave velocity profile: (a) linear SSR analysis and (b) equivalent-linear SSR analysis.

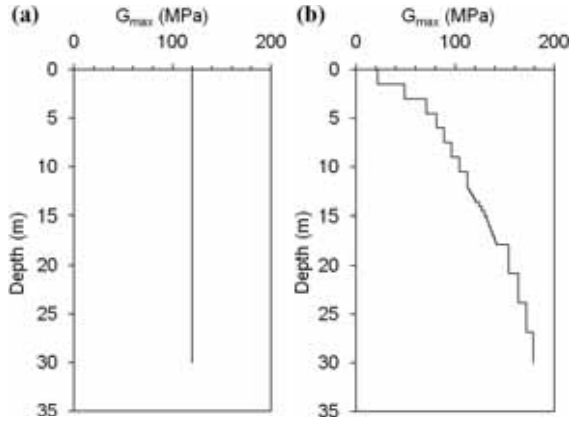

Figure 5. Maximum values of soil shear modulus: (a) linear SSR analysis and (b) equivalent-linear SSR analysis.

column depth (Fig. 5(a)). Its value is G_{max} = 120 MPa. In the equivalent-linear analysis, in accordance with a non-uniform shear-wave velocity profile, the shear modulus is not constant and changes with the depth of the soil column (Fig. 5(b)).

Besides a constant value within the soil column depth, for the case of the linear analysis the soil's shear modulus does not depend on a soil's shear strain level either (G/G_{max} = 1). The value of the **damping ratio** is also constant in the linear approach, and for the sand soil material it is taken to be $D = D_0$ = 1%. In the equivalent linear analyses, for the considered sandy soil material, the equivalent linear soil model as proposed by Seed and Idriss in 1970 (shear-modulus curve) [27] and Idriss in 1990 (damping-ratio curve) [28] was used (Fig. 6). The plot illustrates the prominent properties of the nonlinear soil behaviour – a dependence of both the soil's shear modulus and the damping ratio on the soil's

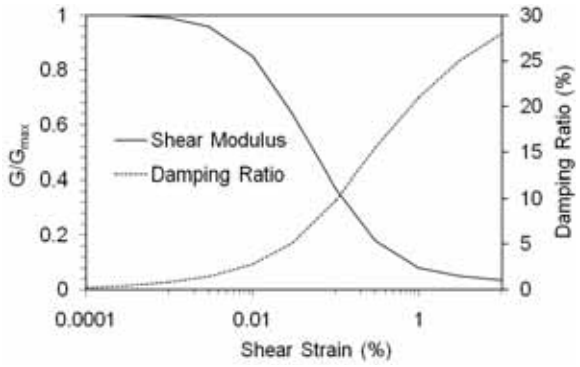

Figure 6. Equivalent-linear model for sand used in EERA code [25].

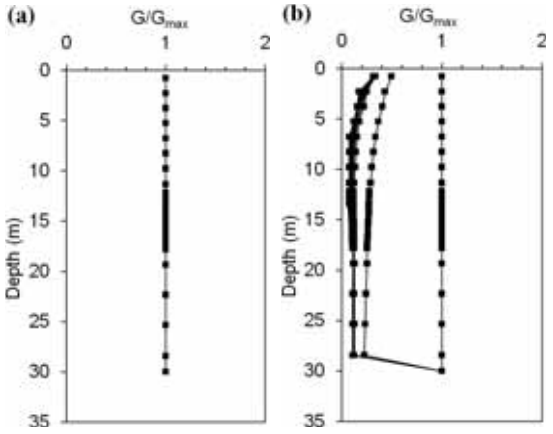

Figure 7. Soil shear modulus ratio G/Gmax: (a) linear SSR analysis and (b) equivalent-linear SSR analysis.

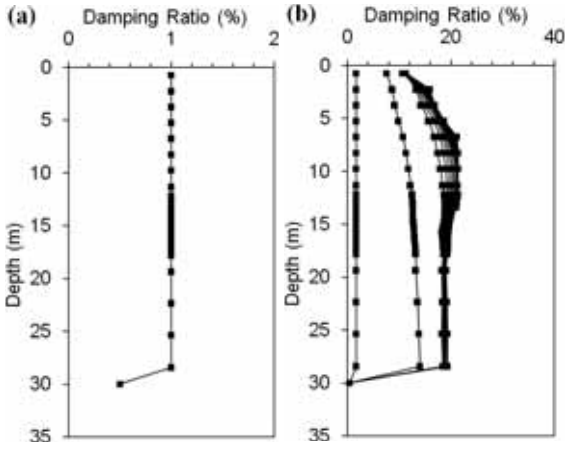

Figure 8. Soil damping ratio: (a) linear SSR analysis and (b) equivalent-linear SSR analysis.

shear-strain rate, i.e., the shear modulus degradation and the damping ratio increase, being influenced by the soil's shear-strain increase. For the previously reported soil properties, diagrams of the soil's shear-modulus ratio

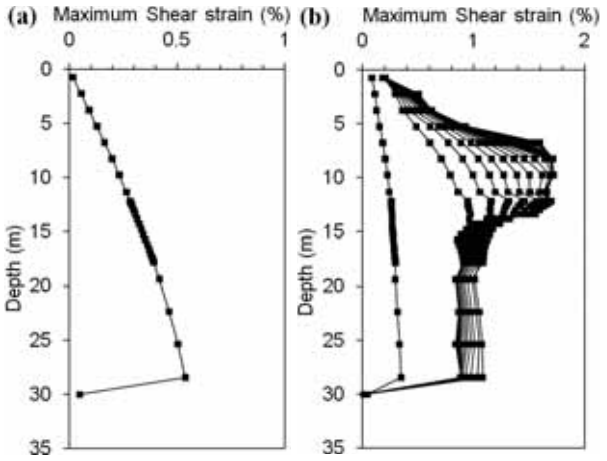

Figure 9. Maximum soil shear strain: (a) linear SSR analysis and (b) equivalent-linear SSR analysis.

G/G_{max} and the damping ratio throughout the soil column are illustrated for the cases of linear and equivalent-linear analyses in the following plots (Fig. 7(a)–(b) and Fig. 8(a)–(b)).

The linear EERA analysis showed that for the given soil profile and input excitation, the **maximum soil shear strain** is 0.54%, and its average value at the tunnel's location (at depths between the crown and invert) is 0.34% (Fig. 9(a)). In the equivalent-linear analysis, the maximum soil shear deformation is 1.72%, whereas its average value at the tunnel's location is 1.16% (Fig. 9(b)). Accordingly, the linear analysis underestimates the soil's shear strain significantly, because with the assumed constant damping ratio of the soil, it neglects the fact that along with a shear-strain level increase (i.e., soil weakening), a soil damping ratio, as well as the possibility of the soil absorbing a portion of the seismic energy, are being increased too, which, on the other hand, is predicted by the equivalent-linear analysis. The seismic energy absorption of the soil (hysteretic energy dissipation) at the level of the tunnel's centre-line for both analyses is illustrated in two subsequent plots (Fig. 10(a)–(b)).

Regarding the **soil's shear stress**, its maximum value obtained from the linear analysis is 646.69 kPa, and the average value at the tunnel's location between 12 and 18 m of the given soil profile is 406.25 kPa. In the equivalent linear analysis, the calculated maximum soil shear stress is 199.45 kPa, whereas its average value between the top and the bottom of the tunnel section is 150.99 kPa. In conclusion, the linear analysis overestimates the soil's shear stress values, since, unlike the equivalent linear soil model, it does not take into account the shear-modulus reduction with the soil's shear-strain amplitudes due to the constant soil shear modulus assumption (Fig. 11(a)–(b)).

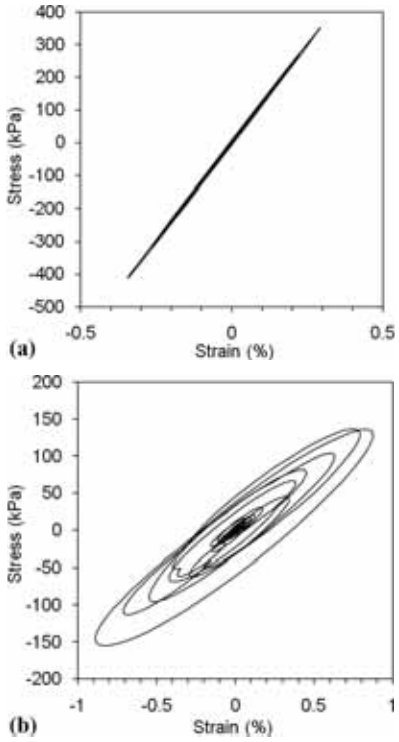

Figure 10. Soil hysteretic energy dissipation at the tunnel's centre-line location: (a) linear SSR analysis and (b) equivalent-linear SSR analysis.

The **peak ground acceleration** at the ground surface is another aspect included in the EERA code SSR analysis (Fig. 12(a)–(b)). For the case of the linear analysis, the maximum ground acceleration value is 1.57g, and at the level of the tunnel's axis it is equal to 1.30g. In the equivalent linear analysis, a_{max} = 1.04g, and at the tunnel spring-line location, it is 0.61g. Hence, the linear analysis gives higher peak ground-acceleration values due to the assumption of a constant damping ratio for the soil. In the equivalent linear analysis, however, the ground-acceleration values are significantly lower. This is correlated with the nonlinear soil property corresponding to the increasing percentage of damping along with the soil's shear-strain increase (i.e., soil weakening), and by that, the soil's ability to absorb a part of the seismic wave energy, which finally results in considerably lower values for the ground acceleration.

The effects of soil damping are illustrated in the figures related to the **amplification ratio** of the ground acceleration at the surface to the acceleration at the bedrock underlying the 30-m-thick soil layer. The linear analysis resulted in an amplification ratio of up to 3.5 and, as can be seen from Fig. 13(a), the amplification function has a number of peaks corresponding to the natural frequencies of the layer, indicating an amplitude decrease with higher frequencies in a slower manner due to the constant

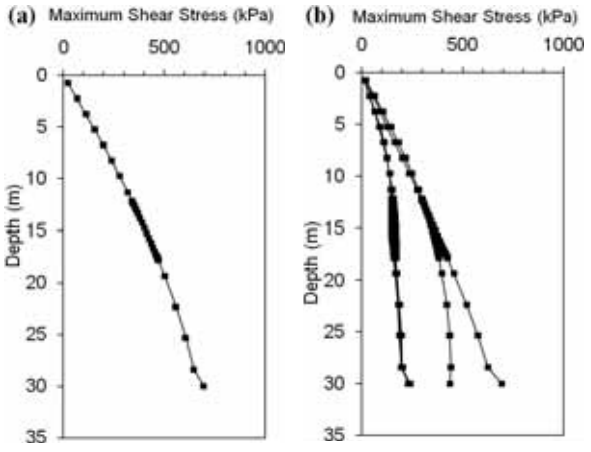

Figure 11. Maximum soil shear stress: (a) linear SSR analysis and (b) equivalent-linear SSR analysis.

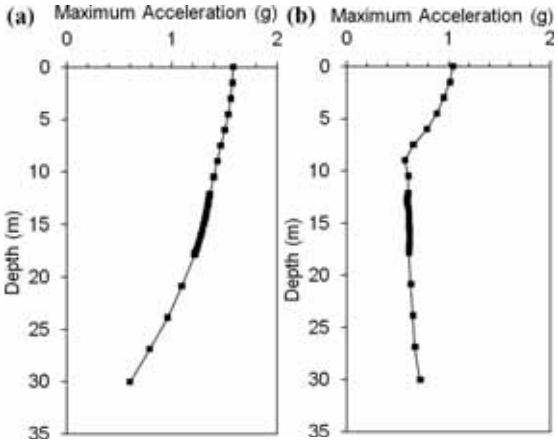

Figure 12. Peak ground acceleration: (a) linear SSR analysis and (b) equivalent-linear SSR analysis.

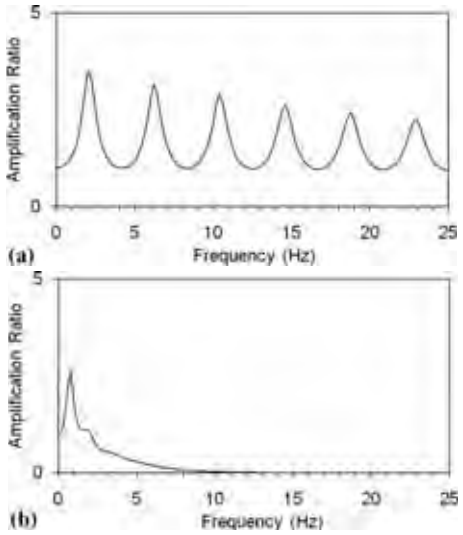

Figure 13. Amplification ratio: (a) linear SSR analysis and (b) equivalent-linear SSR analysis.

soil damping ratio. On the other hand, the amplification function computed by the equivalent-linear analysis resulted in a somewhat lower maximum (2.6), with only a couple of peaks (Fig. 13(b)), due to the prominent soil nonlinearities and high damping values related to the relatively rapid absorption of the seismic wave energy.

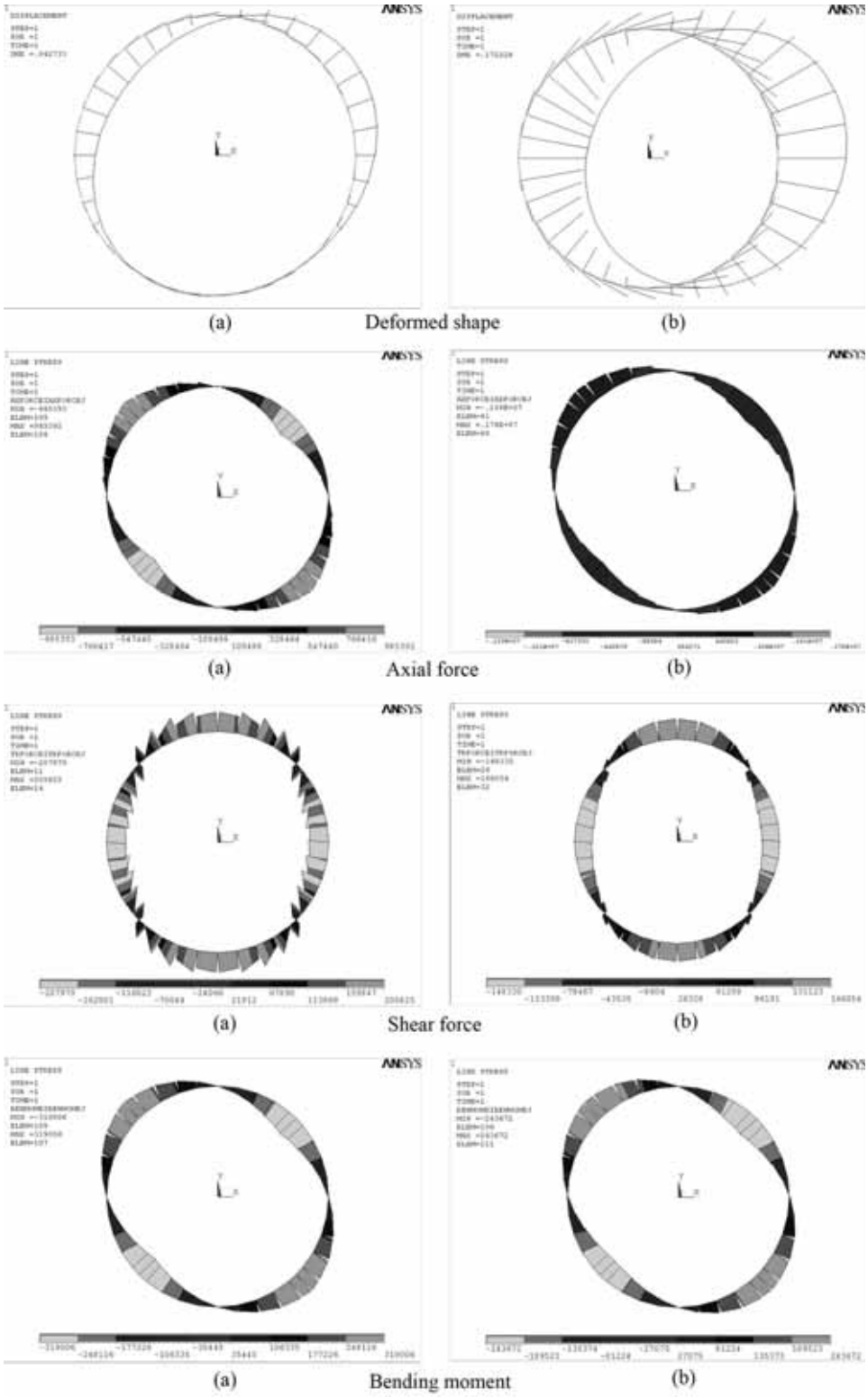

Figure 14. Ovalisation and lining force distributions: (a) linear and (b) nonlinear SSI analysis.

6 ANSYS OUTPUT PLOTS OF LINEAR AND NONLINEAR SOIL–TUNNEL INTERACTION ANALYSES

The corresponding beam–spring numerical model of the linear and nonlinear soil–tunnel interaction analysis was made using ANSYS. The output plots are given for the case of the total loading: earthquake, tunnel section inertia, and soil shear stress. Referring to an ovalisation of a transverse section of the tunnel's lining, all the ANSYS output plots (Fig. 14(a)–(b)) confirmed that the beam–spring model has simulated this deformation pattern successfully in both the linear and nonlinear SSI analyses, since the maxima of the thrust and the bending moment occur at the shoulder and knee locations (θ = 45°, 135°, 225°, and 315°), whereas the extreme values of the transversal force occur at the tunnel crown, abutments, and invert locations of the lining (θ = 0° (360°), 90°, 180°, and 270°).

7. COMPARISON OF LINEAR AND NONLINEAR SOIL–TUNNEL STRUCTURE-INTERACTION ANALYSES

7.1 Comparison of the numerical linear analysis and analytical solutions

First, the results of the simplified dynamic linear analyses are compared to the closed-form elastic solutions related to earthquake-induced sectional forces in the tunnel lining (Fig. 15). The internal forces in the lining are functions of the free-field shear strain γ_{ave} [29]. The considered strain is the average value between the depths corresponding to the crown and the invert of the tunnel. In this work, the state-of-practice analytical expressions by Wang, 1993 [9] and Penzien, 2000 [11] were used, which refer to the tunnel and ground properties corresponding to Fig. 1. In the analyses described here, only the case of a no-slip condition was considered, since it results in maximum values of thrust. Under the assumption of a rough interface between the lining and the soil (assuming compatible displacements of the lining and the ground), the variation of thrust (N), shear force (T), and bending moment (M) in terms of the angle θ is calculated according to equations given by the aforementioned authors. The angle θ is measured counter clockwise with respect to the x-axis.

In applications of the beam–spring model, conducting a simplified dynamic analysis in a simple shear condition, it is quite usual to take into account only the earthquake-induced displacements and eventually the tunnel section's inertial force, without considering the influence of the soil's shear stress. In relation to that, two cases have been analysed in the present study: a beam–spring model without considering the seismically induced soil shear stress and a beam–spring model that involves the soil's shear stress, in order to estimate the error when the shear stress of the soil medium is not accounted for. The common conclusion that can be drawn regarding all the forces in the tunnel's lining is that excluding the soil's shear stress from the coupled beam–spring model, in order to simulate SSI effects, yields a considerable underestimation of the internal lining forces.

With regard to the **thrust** distribution around the lining, considering Wang's solution [9], the beam–spring model, when accounting for the soil's shear stress, provides a fairly consistent distribution of the N-force. On the other hand, the beam–spring model without the soil's shear stress consideration greatly underestimates the values of the axial force, approximately the same as Penzien's solution [11], thus confirming the conclusions of the study by Hashash et al. [30] that Penzien's approach predicts much lower thrust values than those predicted by Wang's method.

Accordingly, ignoring the soil's shear stress in a simplified dynamic analysis by using a beam–spring model yields an error that cannot be tolerated, since the contact between the structure and the surrounding ground in the model is defined in a discrete manner, only at a number of points. On the other hand, such a beam–spring model results in the thrust distribution being approximately the same as obtained with Penzien's approach. This implies that Penzien's methodology severely underestimates the seismically induced maximum thrust in the tunnel's lining under the no-slip assumption for the reason of a lack of implementation of the circumferential stiffness of the tunnel–ground system (resistance to compression), which is in accordance with the remarks in [29], and, because of that, it should be avoided.

Referring to all of the previously mentioned, it can be concluded that, in order to develop reliable simulations and obtain relevant results, a beam–spring model in a simplified dynamic analysis should take into consideration, besides the earthquake-induced soil displacements and the tunnel's inertial force, also the soil's shear stresses.

Furthermore, the distributions of the **transverse forces** and the **bending moments** along the tunnel's lining according to the analytical and numerical results are also illustrated in the same plots (Fig. 15). It should be pointed out that in Wang's approach an expression for the transverse forces does not exist. The presented distribution of the shear forces is opposite to that of Penzien's

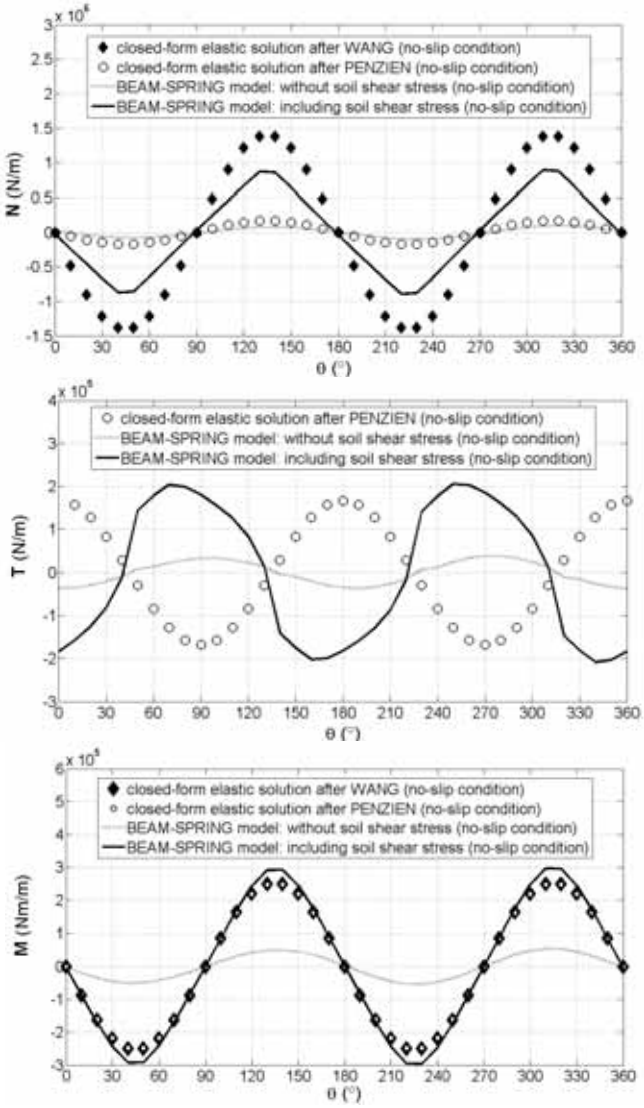

Figure 15. Comparison of the linear SSI analysis results with the closed-form elastic solutions.

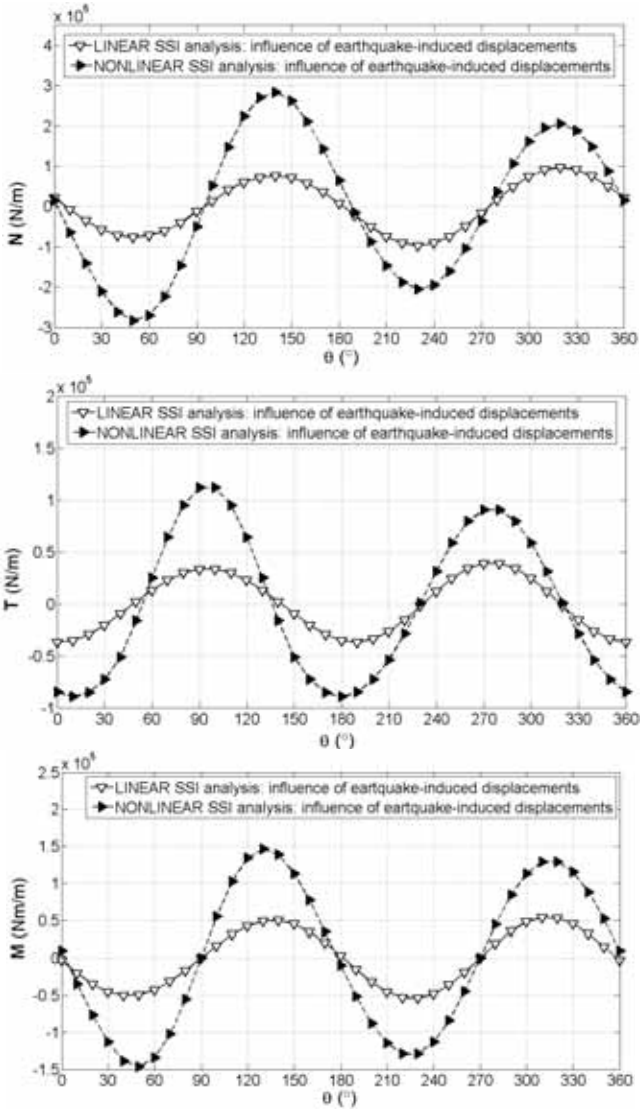

Figure 16. Comparison of thrust, shear force, and bending moment distributions in the tunnel lining computed by the linear and nonlinear SSI analyses: influence of earthquake-induced displacements.

solution, since in the ANSYS software the opposite sign convection for T-forces is established. As to the seismically induced shear forces and bending moments, the coupled beam–spring models involving soil shear stress for the no-slip assumption predict the distribution pattern that matches relatively well with the solutions according to Penzien's and Wang's approaches. This is opposite to the discrete models that do not account for the soil's shear stress, in which case the shear-force and bending-moment values are significantly underestimated when compared to the elastic closed-form solutions. Unlike the thrust distribution, the solutions of Wang and Penzien provide consistent distributions of the bending moments (the symbols related to Wang's and Penzien's solutions for *M* practically coincide).

Finally, it can be observed that the magnitude of the thrust has a much greater influence than the moments on the stresses experienced by the tunnel's lining, which is typical for a rough tunnel–ground interface assumption.

7.2 Influence of seismically induced displacements upon the internal lining forces

Based on a comparison of the results of numerical linear and nonlinear analyses regarding the distributions of thrust, shear force, and bending moment in the tunnel's lining due to earthquake-induced displacements (Fig. 16), the following conclusions can be drawn: the linear analysis, which predicts lower soil shear-strain values, results in smaller soil displacements induced by seismic

shear-wave propagation throughout the sandy soil medium. The maximum displacement values of the tunnel's section are 3.55 cm at the crown and 1.63 cm at the invert locations. Hence, the relative displacement between the top and the bottom of the circular tunnel profile has a lower value (1.92 cm), resulting in a smaller deformation (ovalisation) of the tunnel's cross-section. On the other hand, in the nonlinear analysis, due to a significantly larger soil shearing, the soil displacements are also larger: 17.68 cm at the crown and 12.43 cm at the invert regions. This, of course, results in a greater displacement difference between the top and the bottom of the tunnel's cross-section (5.25 cm) when compared to the linear analysis, which also leads to significantly greater ovalisation of the tunnel's structure.

In conclusion, a linear analysis underestimates the soil's shear strain and, consequently, underestimates the soil displacements due to earthquake action, thus leading to a significant underestimation of the internal lining forces.

7.3 Influence of the soil's shear stress upon the internal lining forces

From the seismically induced soil shear-stress viewpoint, according to Fig. 17, the results are the following: in the linear analysis, the soil shear modulus is constant and does not depend on the soil shear deformation, thus resulting in higher values for the soil's shear stress. In contrast to that, the nonlinear analysis gives significantly lower values for the soil's shear stress, since

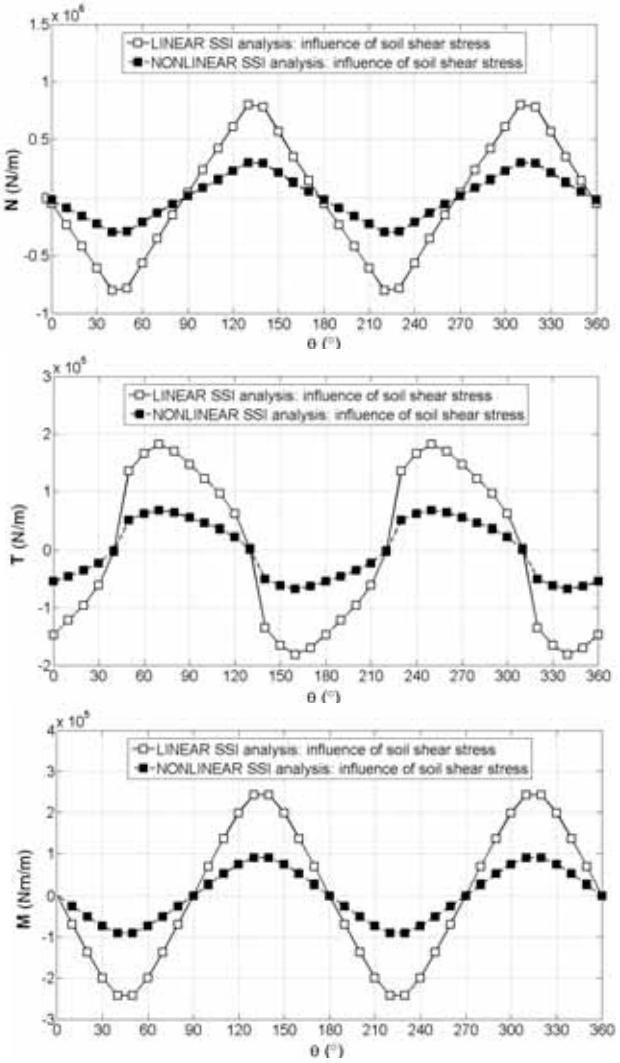

Figure 17. Comparison of thrust, shear force, and bending moment distributions in the tunnel lining computed by the linear and nonlinear SSI analyses: influence of soil shear stress.

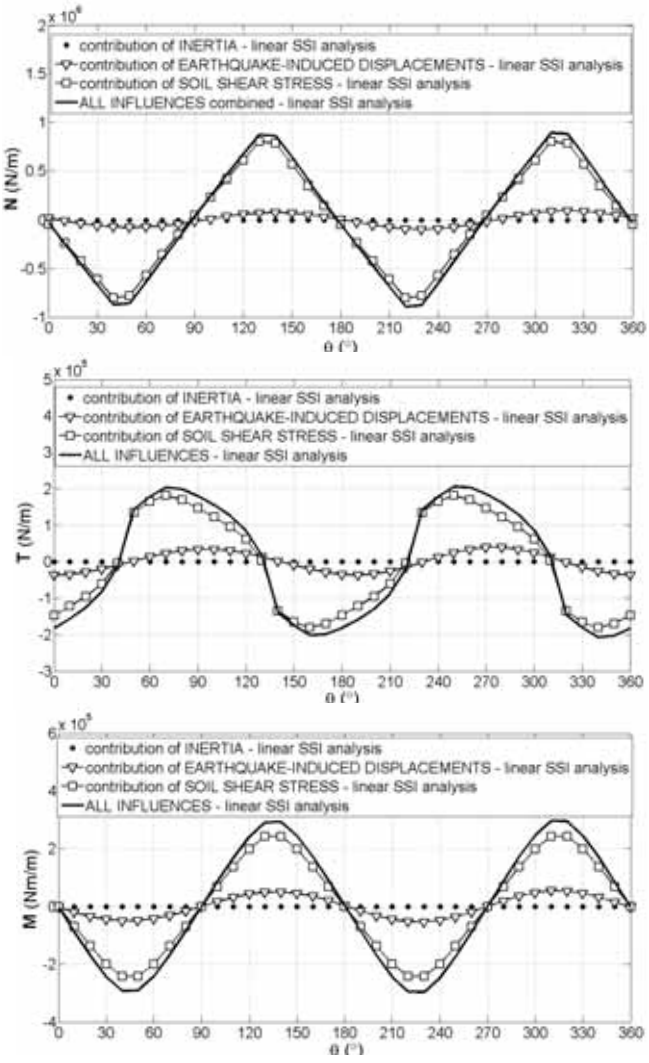

Figure 18. Contribution of earthquake-induced displacements, tunnel section inertial force, and soil shear stress to thrust, shear force, and bending moment distributions in the tunnel lining computed by the linear SSI analysis.

the nonlinear soil model accounts for the soil's shear-modulus degradation with the increase of the soil's shear strain. Hence, it can be observed that a linear analysis represents a conservative solution because it predicts unrealistically high values for the soil's shear stress.

7.4 Influence of the tunnel section inertia upon the internal lining forces

Regarding the inertial force of a tunnel section, it has a higher value in the linear analysis, considering the significantly higher computed values of the ground acceleration in comparison with the nonlinear analysis, as a consequence of the assumption of a constant damping ratio, typical for the linear soil behaviour. In the case of soil behaving in a nonlinear manner, the value of the tunnel section inertial force is considerably lower, owing to the lower ground acceleration, due to the soil's ability to absorb a seismic energy to some extent, and therefore, to enlarge the shearing deformations, resulting in stronger damping abilities. Therefore, a linear analysis overestimates the inertial forces.

7.5 Relative contributions of the partial influences in the total internal lining forces

Referring to the formerly discussed tunnel section inertia, on the basis of the plots given in Fig. 18 and Fig. 19, it can be seen that the relative contribution of the inertial force in the total of the internal lining forces is

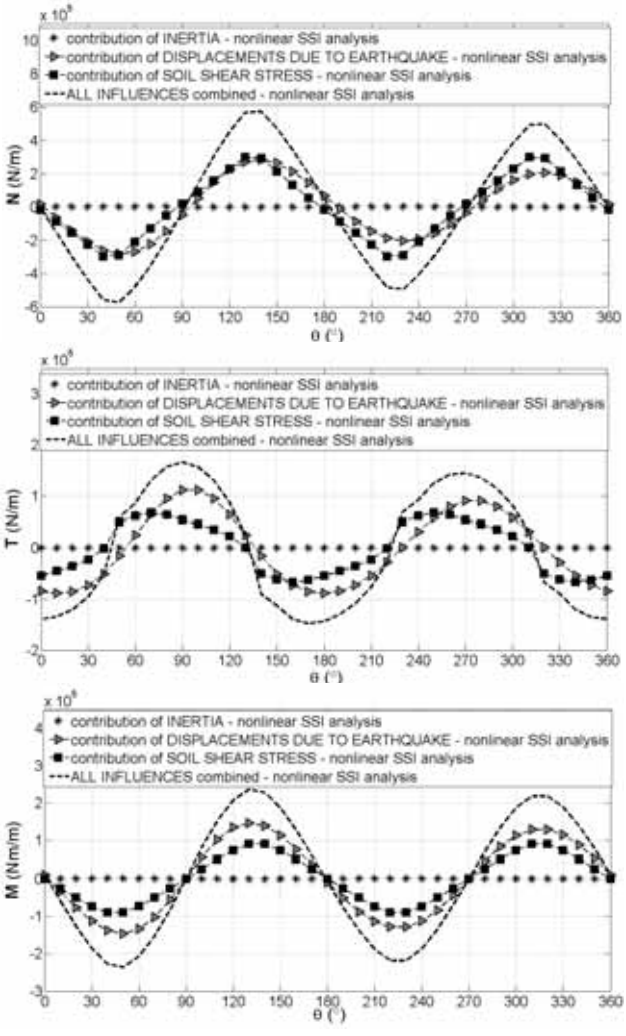

Figure 19. Contribution of earthquake-induced displacements, tunnel section inertial force, and soil shear stress to thrust, shear force, and bending moment distributions in the tunnel lining computed by the nonlinear SSI analysis.

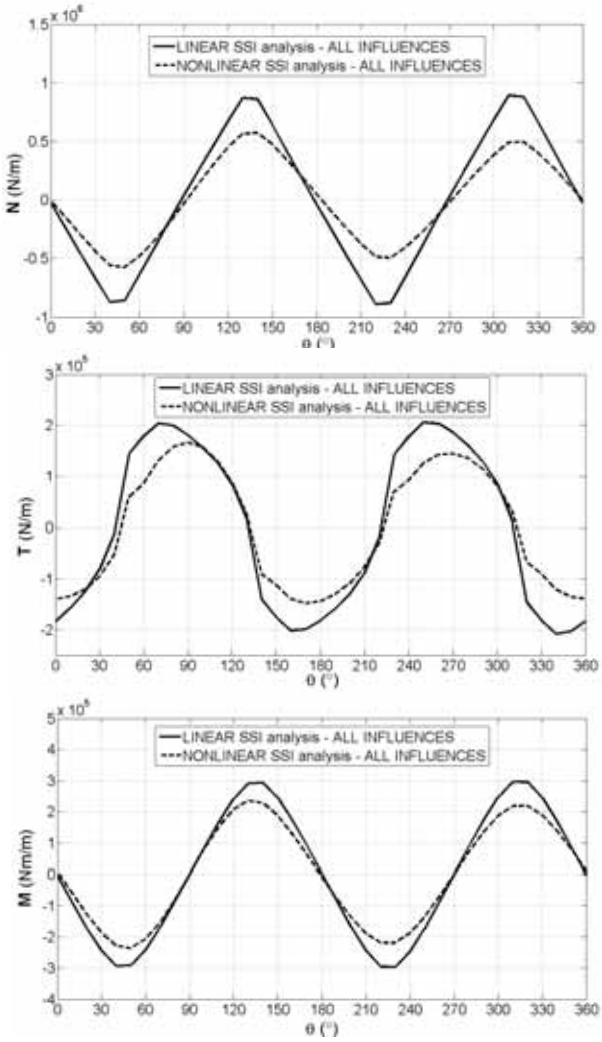

Figure 20. Comparison of thrust, shear force, and bending moment distributions in the tunnel lining computed by the linear and nonlinear SSI analyses: all influences combined (earthquake-induced displacements + tunnel section inertial force + soil shear stress).

negligibly low for the cases of both linear and nonlinear analyses, because it participates in the total lining thrust, shear force, and bending moment distributions by much less than 1%. Considering the relative contributions of the other two factors (i.e., seismically induced displacements and a soil shear stress), there is a quite evident difference between the two types of analysis. According to the results of the linear analysis (Fig. 18), the influence of the soil shear stress is the most dominant in the total distributions of the *N*, *T*, and *M* forces in the tunnel lining. Regarding the results of the nonlinear analysis (Fig. 19), however, earthquake-induced displacements have a predominant influence upon all of the sectional forces, although the contribution of the soil shear stresses is also quite pronounced, particularly in the case of the accumulated thrust.

7.6 Comparison of linear and nonlinear SSI analyses

Taking into consideration the combined effects of all of the influences (i.e., earthquake-induced displacements + tunnel section inertia + soil shear stresses) upon the total distributions of the thrust, shear force, and bending moment in the tunnel lining (Fig. 20), a linear analysis could be considered as the more conservative one for estimating the seismically induced internal lining forces. This is particularly pronounced, as the earthquake excitation and the degree of soil nonlinearities increase.

Although the linear analysis is computationally convenient and provides reasonable results for many practical problems, it presents an approximation of the actual soil–tunnel system response. On the other hand, the nonlinear analysis allows a significant accuracy in simulating the tunnel–ground interaction under earthquake loading conditions due to the fact that the soil behaviour is taken into consideration more realistically regarding its nonlinearity. Nevertheless, more parameters than used for the linear analysis are usually required, the evaluation of which might be complex due to the variability in the soil conditions, the uncertainty in the soil properties, and the scatter in the experimental data upon which many of the input parameters are based. In addition, this analysis suffers from the important disadvantage that the solution time, the computational cost, and the complexity of the analysis are substantially increased.

8. CONCLUDING REMARKS

Considering the analyses described in this paper, related to the simplified dynamic linear and nonlinear analyses of soil–tunnel structure interaction studied by a numerical coupled beam–spring model under no-slip condition, with a special emphasis on the relative contributions of partial influences, such as the earthquake-induced displacements, soil shear stress, and tunnel section inertia, in the total internal lining forces, the following conclusions can be drawn:

– When using the beam–spring model, in order to simulate the SSI effects correctly, soil shear stresses should be taken into account along with seismically induced displacements. It was found that the relative part of the cross-sectional forces induced by the tunnel section inertia is significantly less than 1% of the total computed values for both the linear and nonlinear analyses. This is not surprising, since the tunnel section inertia is negligible relative to the inertia of the surrounding ground. Therefore, the inertial force could be ignored in a numerical model.

– A significant discrepancy in the computed seismically induced lining thrust between Wang's and Penzien's analytical approach is validated. The comparisons with numerical results clearly demonstrate that Wang's solution provides a realistic estimation of the thrust in the tunnel linings for the no-slip condition. Accordingly, Penzien's expression for the seismically induced axial force in the lining under the rough interface assumption should be avoided.

– Linear analysis underestimates the soil shear strain, and consequently also underestimates the soil displacements induced by seismic shear-wave propagation, producing a significant underestimation of the tunnel lining's cross-sectional forces. In addition, it predicts unrealistically higher values of the soil shear stress due to the assumption of a constant soil shear modulus throughout the analysis, thus resulting in higher internal lining forces. From a tunnel inertial force point of view, it overestimates the lining's cross-sectional forces, considering significantly higher computed ground accelerations compared to nonlinear analysis, as a consequence of the constant damping ratio assumption typical for the linear soil behaviour. The influence of the soil shear stress is the most dominant in total distributions of *N, T*, and *M* forces in the tunnel lining.

– Nonlinear analysis, due to a prediction of a significantly larger soil shearing (soil displacements), results in a higher relative displacement between the top and the bottom of the circular tunnel cross-section compared to the linear analysis. This leads to significantly greater ovalisation of the tunnel structure, and therefore to higher values of the internal

lining forces. Unlike the linear approach, a nonlinear analysis gives lower values of the soil shear stress, since the nonlinear soil model accounts for the soil shear modulus reduction, as the soil shear strain increases. In the case of soil behaving in a nonlinear manner, the tunnel section inertial forces are lower owing to lower ground accelerations, due to an increase of the damping ratio with the soil shear strain increase, as well as the nonlinear soil property to absorb a significant portion of the seismic wave energy along with the soil weakening. Earthquake--induced displacements have a predominant influence upon all of the cross-sectional forces, although the relative contribution of the soil shear stresses is also quite significant.

– It seems that the linear analysis can result in a more conservative estimation of the internal forces in the tunnel lining, as the peak acceleration and the level of soil nonlinearity increase.

In order to improve the models and to validate the above drawn conclusions, analyses with more complex models should be performed, in accordance with the most recent achievements in the area of tunnel structures under seismic impact. The interface region between the tunnel lining and the surrounding ground could be more properly simulated as a full-slip contact, with separation allowed under tensile stresses. In addition, the effects of the secondary compressional P-waves, resulting from the shear S-waves scattered by the ground surface, should also be taken into account. Therefore, a possible course of further researches should be in accordance with the former stated remarks, and is an ongoing research activity of the authors of this paper.

Acknowledgement

The authors gratefully acknowledge the support of the Ministry of Education, Science and Technological Development of the Republic of Serbia in the scope of the scientific-research projects TR36028 (2011–2014) and TR36043 (2011–2014).

REFERENCES

[1] Kouretzis, G.P., Sloan, S.W., Carter, J.P. 2013. Effect of interface friction on tunnel liner internal forces due to seismic S- and P-wave propagation. Soil Dynamics and Earthquake Engineering 46, 41-51. doi: 10.1016/j.soildyn.2012.12.010

[2] Owen, G.N., Scholl, R.E. 1981. Earthquake engineering of large underground structures. Report FHWA/RD-80/195, Federal Highway Administration and National Science Foundation, McLean, Virginia.

[3] Newmark, N.M. 1968. Problems in wave propagation in soil and rock. Proc. Int. symp. on Wave Propagation and Dynamic Properties of Earth Materials, Albuquerque, New Mexico, pp. 7-26.

[4] St. John, C.M., Zahrah, T.F. 1987. Aseismic design of underground structures. Tunnelling and Underground Space Technology 2(2), 165-197.

[5] Burns, J.Q., Richard, R.M. 1964. Attenuation of stresses for buried cylinders. Proc. Symp. on Soil–Structure Interaction, University of Arizona at Tempe, Arizona, pp. 378-392.

[6] Hoeg, K. 1968. Stresses against underground structural cylinders. Journal of the Soil Mechanics and Foundations Division, ASCE 94(4), 833-858.

[7] Peck, R.B., Hendron, A.J., Mohraz, B. 1972. State of the art in soft ground tunneling. Proc. Conf. on Rapid Excavation and Tunneling, American Institute of Mining, Metallurgical and Petroleum Engineers, New York, pp. 259-286.

[8] Schwartz, C.W., Einstein, H.H. 1980. Improved design of tunnel supports: Vol. 1 – Simplified analysis for ground–structure interaction in tunneling. Report UMTA-MA-06-0100-80-4, US Department of Transportation, Urban Mass Transportation Administration, Washington DC.

[9] Wang, J.N. 1993. Seismic design of tunnels: a state-of-the-art approach. Parsons, Brinckerhoff, Quade and Douglas, Inc., New York.

[10] Penzien, J., Wu, C. 1998. Stresses in linings of bored tunnels. International Journal of Earthquake Engineering and Structural Dynamics 27(3), 283-300. DOI: 10.1002/(SICI)1096-9845(199803)27:3<283::AID-EQE732>3.0.CO;2-T

[11] Penzien, J. 2000. Seismically induced racking of tunnel linings. International Journal of Earthquake Engineering and Structural Dynamics 29(5), 683-691. DOI: 10.1002/(SICI)1096-9845(200005)29:5<683::AID-EQE932>3.0.CO;2-1

[12] Hashash, Y.M.A., Hook, J.J., Schmidt, B., Yao, J.I.-C. 2001. Seismic design and analysis of underground structures. Tunnelling and Underground Space Technology 16, 247-293.

[13] Billota, E., Lanzano, G., Russo, G., Santucci de Magistris, F., Silvestri, F. 2008. An early-stage design procedure for circular tunnel lining under seismic actions. Proc. 14th World conf. on Earthquake Engineering, Beijing, Paper No. 08-02-0049.

[14] Corigliano, M., Scandella, L., Lai, C.G., Paolucci, R. 2011. Seismic analysis of deep tunnels in near fault

conditions: a case study in Southern Italy. Bulletin of Earthquake Engineering 9(4), 975-995. doi: 10.1007/s10518-011-9249-3

[15] Kouretzis, G.P., Andrianopoulos, K.I., Sloan, S.W., Carter, J.P. 2014. Analysis of circular tunnels due to seismic P-wave propagation, with emphasis on unreinforced concrete liners. Computers and Geotechnics 55, 187-194. http://dx.doi.org/10.1016/j.compgeo.2013.08.012

[16] Billota, E., Lanzano, G., Russo, G., Santucci de Magistris, F., Aiello, V., Conte, E., Silvestri, F., Valentino, M. 2007. Pseudostatic and dynamic analyses of tunnels in transversal and longitudinal directions. Proc. 4th Int. conf. on Earthquake Geotechnical Engineering, Thessaloniki, Paper No. 1550.

[17] Kramer, S.L. 1996. Geotechnical earthquake engineering. Prentice Hall, New Jersey.

[18] Kontoe, S., Zdravkovic, L., Potts, D.M., Menkiti, C.O. 2008. Case study on seismic tunnel response. Canadian Geotechnical Journal 45, 1743-1764.

[19] ANSYS Inc. 2012. ANSYS Documentation, ANSYS Multiphysics. Canonsburg, Pennsylvania. www.ansys.com.

[20] Zlatanović, E., Broćeta, G., Popović-Miletić, N. 2013. Numerical modelling in seismic analysis of tunnels regarding soil–structure interaction. Facta Universitatis, Series: Architecture and Civil Engineering 11(3), 251-267. doi:10.2298/FUACE1303251Z

[21] Mizuno, K., Koizumi, A. 2006. Dynamic behavior of shield tunnels in the transverse direction considering the effects of secondary lining. Proc. 1st European conf. on Earthquake Engineering and Seismology, Geneva, Paper No. 1359.

[22] Matsubara, K., Hoshiya, M. 2000. Soil spring constants of buried pipelines for seismic design. Journal of Engineering Mechanics 126(1), 76-83.

[23] ALA-ASCE. 2001. Guidelines for the design of buried steel pipe. Reston, Virginia. http://www.americanlifelinesalliance.com/pdf/Update061305.pdf.

[24] Verruijt, A. 2005. Soil dynamics. Delft University of Technology, Delft.

[25] Bardet, J.P., Ichii, K., Lin, C.H. 2000. EERA – A computer program for Equivalent-linear Earthquake site Response Analyses of layered soil deposits. University of Southern California, Los Angeles.

[26] Zlatanović, E., Lukić, D., Šešov, V. 2014. Pseudostatic and simplified dynamic methods of design soil shear strain evaluation in seismic analysis of tunnel structures. Izgradnja 68(1-2), 9-19 (in serbian).

[27] Seed, H.B., Idriss, I.M. 1970. Soil moduli and damping factors for dynamic response analyses. Report EERC 70-10, Earthquake Engineering Research Center, University of California, Berkeley.

[28] Idriss, I.M. 1990. Response of soft soil sites during earthquakes. Proc. H. Bolton Seed Memorial Symposium, J.M. Duncan (ed.), Vol. 2, BiTech Publishers, Vancouver, British Columbia, Canada, pp. 273-289.

[29] Zlatanović, E., Lukić, D., Šešov, V. 2014. Presentation of analytical solutions for seismically induced tunnel lining forces accounting for soil–structure interaction effects. Building Materials and Structures 57(1), 3-28.

[30] Hashash, Y.M.A., Park, D., Yao, J.I.-C. 2005. Ovaling deformations of circular tunnels under seismic loading: an update on seismic design and analysis of underground structures. Tunnelling and Underground Space Technology 20, 435-441. doi: 10.1016/j.tust.2005.02.004

PRAKTIČNA METODA ZA OPTIMALNO ZASNOVO PASOVNEGA TEMELJA Z OPTIMIZACIJO S KOLONIJO MRAVELJ

Boonchai Ukritchon *(vodilni avtor)*
Chulalongkorn University,
Department of Civil Engineering
Bangkok, Tajska
E-pošta: boonchai.uk@gmail.com

Suraparb Keawsawasvong
Chulalongkorn University,
Department of Civil Engineering
Bangkok, Tajska
E-pošta: suraparb@hotmail.com

Ključne besede

optimalno načrtovanje; temeljenje; stabilnost; nelinearno programiranje; optimizacija kolonije mravelj

Izvleček

Namen članka je predstaviti praktično metodo optimalne zasnove pasovnih temeljev obremenjenih z vertikalnimi in horizontalnimi obtežbami. Problem načrtovanja z iskanjem optimalne velikosti temelja in minimalne količine armature je izražen v nelinearni minimalizacijski obliki. Na vrhu pasovnega temelja delujejo vertikalne in horizontalne obtežbe. V problemu načrtovanja nastopajo štiri neodvisne spremenljivke, in sicer širina temelja, debelina temelja, globina temeljenja in količina armature. Zahtevane geotehnične omejitve vključujejo preveritve nosilnosti, prevrnitve, kot tudi globalni zdrs in lokalni zdrs na vogalih temeljev. Kratkotrajna stabilnost in dolgotrajna stabilnost sta sočasno formulirani. Konstrukcijske omejitve zajemajo kontrolo odpora prereza na strižne sile in upogibne momente.

Formulacija omejitvenega problema vodi do nelinearnega programiranja katerega cilj je zmanjšati skupno maso materiala temelja, vključno z betonom in armaturo. Optimalna rešitev je dobljena z algoritmom optimizacije s kolonijami mravelj, MIDACO. Predlagana metoda optimizacije je prikazana na primeru dejanskega načrtovanje temelja za podporo velikega stroja, ki se premika po tirih.

A PRACTICAL METHOD FOR THE OPTIMAL DESIGN OF CONTINUOUS FOOTING USING ANT-COLONY OPTIMIZATION

Boonchai Ukritchon *(corresponding author)*
Chulalongkorn University,
Department of Civil Engineering
Bangkok, Thailand
E-mail: boonchai.uk@gmail.com

Suraparb Keawsawasvong
Chulalongkorn University,
Department of Civil Engineering
Bangkok, Thailand
E-mail: suraparb@hotmail.com

Keywords

optimal design; footing; stability; nonlinear programming; ant-colony optimization

Abstract

The objective of this paper is to present a practical method for the optimal design of a continuous footing subjected to vertical and horizontal loads. The design problem of finding the optimal size of footing as well as the minimum steel reinforcement is formulated in a nonlinear minimization form. The continuous footing is subjected to the vertical and horizontal loads acting on the top of the column. There are four design variables in the design problem, i.e., the width of the footing, the thickness of the footing, the soil-embedment depth, and the amount of steel reinforcement. The required geotechnical constraints include the bearing capacity, overturning, as well as global sliding and local sliding at the footing corners. Short-term stability and long-term stability are considered simultaneously in the same formulation. The structural constraints are enforced to control the shear force and bending moment within the section resistance. The formulation of the problem's constraints leads to the nonlinear programming, whose objective function is to minimize the total cost of the footing material, including the concrete and steel reinforcement. The optimal solution is solved using the ant-colony optimization algorithm MIDACO. The proposed optimization method is demonstrated through the actual design of the footing for supporting a large machine moving on rails.

1 INTRODUCTION

A shallow foundation is generally used to support a structure when the underlying soil has a relatively high shear strength. The conventional design of a shallow foundation subjected to a vertical loading is an iterative process that considers geotechnical analysis and structural reinforced-concrete design separately. The dimension of the footing must be assumed initially such that a geotechnical analysis of the bearing capacity is evaluated. Once the geotechnical considerations have been satisfied, the design of a structurally reinforced-concrete footing is then carried out. This process is repeated in order to determine the optimal dimensions of the footing as well as the amount of steel reinforcement. Thus, the conventional process for the optimal design of a footing is iterative and practical.

This paper studies the optimal design of a continuous footing subjected to vertical and horizontal loads. This foundation is used to support a large machine, such as a stacker or a reclaimer used in a bulk-material handling process, as shown in Fig. 1 [1, 2]. These machines move slowly on a rail on top of strip footing in order to pile up the bulk material as a stockpile (stacker, Fig. 1(a)) or to recover the material (reclaimer, Fig. 1(b)) from a stockpile. Bulk materials include coal, limestone, ores, etc.

(a) stacker machine [1]

(b) reclaimer machine [2]

Figure 1. Large machine used in bulk-material handling process.

The optimal design of a continuous footing supporting these machines is complex because it is involved with checking the safety factors of several geotechnical criteria. The horizontal load adds more complexities and more stability evaluation, in addition to the standard bearing capacity for the vertical load case. The geotechnical analyses must evaluate additional failure mechanisms, namely, overturning, global sliding, and local sliding at the edge or corner of the footing. In addition, the short-term stability and long-term stability of these failure mechanisms must be considered in the analysis.

The techniques of optimization have been applied to many problems in geotechnical engineering [3, 4, 5, 6, 7]. Various previous studies have mainly focused on the optimal design of retaining structures and some optimization methods were proposed and developed. Early research of the optimization of a retaining wall was pioneered by Rhomberg and Street [8]. Saribas and Erbatur [9] presented a detailed study of the optimum design for reinforced-concrete cantilever retaining walls with seven geometrical and reinforcement design variables, where the constrained nonlinear programming was solved by a specially prepared program. Ten modes of wall failure, including overturning, sliding, eccentricity, bearing capacity, shear and the bending moment of the toe slab, heel slab and stem of the wall were considered. A similar technique for the optimization of a retaining wall was studied by Basudkar and Lakshman [10]. Alshawi et al. [11] applied the optimization method to a tie-back retaining wall.

Ceranic et al. [12] studied the application of a simulated annealing algorithm to a problem with only geometrical design variables. Castillo et al. [13] and Babu and Basha [14] presented an approach for a reliability-based design optimization of a reinforced-concrete cantilever retaining wall, where the analysis was performed by treating the input parameters as random variables. Khajehzadeh et al. [15] presented the effectiveness of the particle-swarm optimization with a passive congregation algorithm to the economic design of a retaining wall, where the problem consisted of eight geometrical and reinforcement design variables and the constraints were the same as those of Babu and Basha [14]. The ant-colony optimization method was proposed by Ghazavi and Bonab [16] to determine the optimal design of a reinforced concrete retaining wall. Camp and Akin [17] employed a numerically simple optimization algorithm, the big-bang/big-crunch optimization for designing low-cost or low-weight cantilever reinforced-concrete retaining walls with base shear keys. A numerical model was proposed by Pourbaba et al. [18] to obtain the optimum cost of cantilever retaining walls having different cases of backfill, where the optimal solution of the economical sections was determined by the chaotic imperialist competitive algorithm, minimizing the cost of the sections. Papazafeiropoulos et al. [19] employed two-dimensional finite-element simulations together with the genetic algorithm to find the optimum design of cantilever reinforced-concrete retaining walls with considerations for earthquake loading, where the linear elastic soil, retaining wall stem and wall foundation were assumed to calculate the seismic earth pressures. The optimum design of gravity and reinforced retaining walls using the enhanced charged system search algorithm, the recently developed meta-heuristic algorithm, was introduced by Talatahari and Sheikholeslami [20] to obtain the least-cost sections with different cases of backfill. Very recently, Sadoglu [21] proposed an optimization technique for the optimal design of a symmetrical gravity retaining wall. It is clear that most of the previous investigations have heavily focused on the optimal design of cantilever or gravity retaining walls where different optimization algorithms were proposed to solve the formulated optimization problems.

Several researches on the optimal design of foundations were conducted in the past [22, 23, 24 and 25]. Some studies focused on optimal design with a finite-element analysis [22], while the remaining focused on its mathematical formulation and derivation [23, 24, and 25]. The optimization technique was also applied to a steel pile group foundation [26]. Very few researches have studied the practical application of optimization for a strip footing. Moreover, none of research has considered short-term and long-term geotechnical conditions in the same optimization. These are the main contributions of the proposed practical method in this study.

In this paper, a practical method for the optimal design of a continuous footing subjected to vertical and horizontal loads is proposed. The geotechnical and structural constraints are enforced in order to setup a feasible region of the decision variable, including the footing width, the footing thickness, the soil-embedment depth, and the main steel reinforcement. The short-term and long-term stability are considered simultaneously in the same numerical optimization. The proposed nonlinear programming problem is solved using a state-of-the-art, ant-colony optimization algorithm, MIDACO [27, 28, 29, 30]. The proposed practical method of numerical optimization is applied to determine the optimal design of a continuous footing that supports a very large machine moving slowly on rail such as stacker or reclaimer, where they are commonly used in the stockpile.

2. PROBLEM FORMULATION

Fig. 2 shows the problem geometry for determining the optimal dimension of a continuous footing subjected to the vertical load (P) and the horizontal load (H). In this analysis, the global variable (X) consists of four design variables as:

$$X = (x_1, x_2, x_3, x_4) \qquad (1)$$

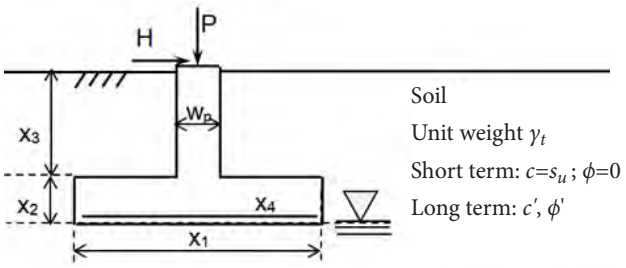

Figure 2. Problem geometry and design variables.

where

x_1 = Footing width (m)
x_2 = Footing thickness (m)
x_3 = Soil-embedment depth (m)
x_4 = Cross-sectional area of the main steel reinforcement (m^2/m)

Those four design variables represent the maximum unknowns of the continuous footing that can be optimized in the design. It should be noted that the width of the pedestal wall (W_p) is not considered as a design variable, but constitutes one of the input parameters because its size is controlled by the superstructure design.

2.1 Geotechnical constraints

Since this footing is subjected to both the vertical and horizontal loads, such a condition produces equivalently the inclined and eccentric loading, as shown in Fig. 3. The footing has the load eccentricity (e) measured from the centreline and the load inclination (α) with respect to the vertical line. The vertical component (Q_v) of the total load of the footing (Q) is the sum of the applied vertical load, the weight of the concrete footing, and the weight of the soil embedment. These expressions can be written in terms of the design variables as:

$$Q_v = P + \gamma_c x_1 x_2 + \gamma_c W_p x_3 + \gamma_t (x_1 - W_p) x_3 \qquad (2)$$

$$e = H(x_2 + x_3) / Q_v \qquad (3)$$

$$\alpha = \arctan(H / Q_v) \qquad (4)$$

where

P = The applied vertical load at the centre of the pedestal wall
H = The applied horizontal force at the centre of the pedestal wall
γ_c = Unit weight of concrete
γ_t = Total unit weight of back-filled soil

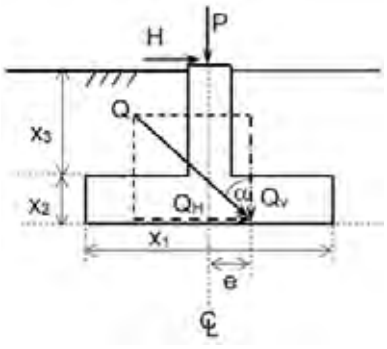

Figure 3. Equivalent problem of an inclined and eccentrically loaded strip footing.

It should be noted that the eccentricity distance e is calculated straightforwardly by taking the moment equilibrium at the centre of the footing base.

In this analysis it is assumed that the properties of the back-filled soil above the base of the footing are the same as those of the underlying soil. The net resulting inclined and eccentric load of the footing gives rise to the non-uniform, applied pressure underneath the footing base, as shown in Fig. 4. The maximum pressure ($q_{\max}$) and the minimum pressure ($q_{\min}$) at the footing corners can be calculated based on the vertical force equilibrium as:

$$q_{\max} = \frac{Q_v}{x_1}\left(1+\frac{6e}{x_1}\right) \qquad (5)$$

$$q_{\min} = \frac{Q_v}{x_1}\left(1-\frac{6e}{x_1}\right) \qquad (6)$$

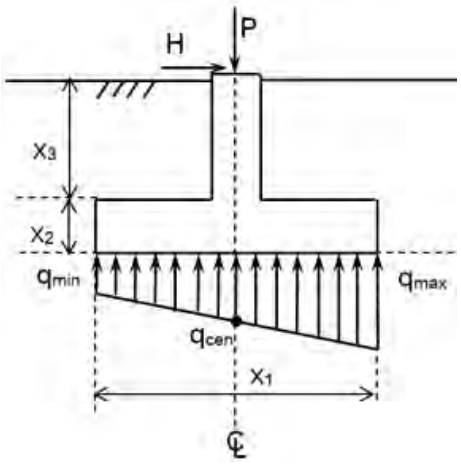

Figure 4. Pressure distribution under the footing.

Since the considered foundation is the strip footing, it is not necessary to include the correction factors for the footing shape. However, the depth factors (F_{cd}, F_{qd}, $F_{\gamma d}$), the inclination factors (F_{ci}, F_{qi}, $F_{\gamma i}$) and the effective width concept must be applied for calculating the ultimate bearing capacity (q_{ult}) of the footing. These correction factors together with the standard bearing-capacity factors (N_c, N_q, N_γ) can be found in most standard foundation textbooks [31, 32, 33]. The short- ($q_{ult,s}$) and long-term ($q_{ult,l}$) ultimate bearing capacity of this continuous footing can be approximated using Terzaghi's general bearing-capacity equation as:

$$q_{ult,s} = s_u N_c F_{cd} F_{ci} + qN_q F_{qd} F_{qi} + 0.5B'\gamma N_\gamma F_{\gamma d} F_{\gamma i} \qquad (7)$$

$$q_{ult,l} = c'N_c F_{cd} F_{ci} + q'N_q F_{qd} F_{qi} + 0.5B'\gamma' N_\gamma F_{\gamma d} F_{\gamma i} \qquad (8)$$

where

s_u = Undrained shear strength of soil
c' = Effective cohesion of soil
ϕ' = Effective friction angle of soil
γ' = Buoyant unit weight of soil = γ_t - γ_w
γ_w = Unit weight of water
q = Total surcharge = $\gamma_t(x_2 + x_3)$
q' = Effective surcharge = $\gamma'(x_2 + x_3)$
B' = Effective footing width = x_1 - $2e$

For the short-term condition or the total stress analysis, the $\phi = 0$ concept is applied in equation (7). For the long-term condition or the effective stress analysis, the effective cohesion and the effective soil friction angle are substituted in equation (8). Even though the ground-water table is assumed to locate at the base of the footing, the effective unit weight is used to calculate the effective surcharge due to the effect of the perched water table.

The corresponding ultimate load per unit length for the short- ($Q_{ult,s}$) and the long-term ($Q_{ult,l}$) conditions of the continuous footing are calculated from the effective width of the footing as:

$$Q_{ult,s} = q_{ult,s}B' \qquad (9)$$

$$Q_{ult,l} = q_{ult,l}B' \qquad (10)$$

The factor of safety against a bearing-capacity failure defined in terms of stress for the short-term ($FS_{bs,s}$) and long-term ($FS_{bs,l}$) conditions are given as:

$$FS_{bs,s} = q_{ult,s} / q_{\max} \qquad (11)$$

$$FS_{bs,l} = q_{ult,l} / q_{\max} \qquad (12)$$

The geotechnical criterion requires that the safety factor against a bearing-capacity failure must be equal to or greater than the required value. In addition, the minimum applied stress must be compression or greater than zero in order not to cause tensile stress to the underlying soil. These two criteria can be written for the short-term and long-term constraints as:

$$G_1(X) = FS_{bs,s} - FS_{b,r} \geq 0 \qquad (13)$$

$$G_2(X) = FS_{bs,l} - FS_{b,r} \geq 0 \qquad (14)$$

$$G_3(X) = q_{\min} \geq 0 \qquad (15)$$

where $FS_{b,r}$ = Required safety factor for a bearing-capacity failure.

In addition to enforcing the safety factor against a bearing-capacity failure as a function of stress, it is advisable

to enforce this term as a function of force. The factors of safety against a bearing-capacity failure defined in terms of force for the short-term ($FS_{bf,s}$) and long-term conditions ($FS_{bf,l}$) are given as:

$$FS_{bf,s} \quad Q_{ult,s} \quad Q \qquad (16)$$

$$FS_{bf,l} = Q_{ult,l} / Q \qquad (17)$$

Thus, those safety factors for a bearing-capacity failure in terms of force must be equal to or greater than the required value as:

$$G_4(X) = FS_{bf,s} - FS_{b,r} \geq 0 \qquad (18)$$

$$G_5(X) = FS_{bf,l} - FS_{b,r} \geq 0 \qquad (19)$$

It should be noted that expressions (13), (14) and (18), (19) can produce the same result in the case that there is no horizontal load acting on the top of the footing. In other words, it corresponds to the case of the concentric load without eccentricity, which is in contrast to the strip footing considered here.

The next geotechnical consideration is the overturning stability of the footing since it is applied using the horizontal load. The driving moment (M_d) about the right corner of the footing for the overturning mechanism and the resisting moment (M_r) due to the self-weight of concrete, the soil embedment and the applied total vertical force are given as:

$$M_r = Q_v X_1 / 2 \qquad (20)$$

$$M_d = H(x_2 + x_3) \qquad (21)$$

The safety factor against the overturning mechanism (FS_{ov}) is defined in terms of the ratio of the resisting moment to the driving moment as:

$$FS_{ov} = M_r / M_d \qquad (22)$$

The geotechnical criterion requires that the safety factor against the overturning mechanism (FS_{ov}) must be equal to or greater than the required value ($FS_{ov,r}$) as:

$$G_6(X) = FS_{ov} - FS_{ov,r} \geq 0 \qquad (23)$$

The last geotechnical criterion is the sliding stability of the footing along its base. In this case, the passive earth force of the soil embedment is neglected for the reason of conservatism. The resisting sliding force for the short- ($F_{r,s}$) and the long-term ($F_{r,l}$) conditions are given as:

$$FS_{r,s} = s_{ui} B' \qquad (24)$$

$$FS_{r,l} = c_i' B' + Q_v \tan(\delta') \qquad (25)$$

where

s_{ui} = Interface undrained shear strength between concrete and soil = $0.5 s_u$

c_i' = Interface effective cohesion between concrete and soil = $0.5c'$

δ' = Interface friction between concrete and soil = $0.5\phi'$

The sliding failure mechanism is caused by the applied horizontal force. Thus, the factors of safety against the global sliding for the short-term ($FS_{gs,s}$) and long-term ($FS_{gs,l}$) conditions are defined as:

$$FS_{gs,s} = F_{r,s} / H \qquad (26)$$

$$FS_{gs,l} = F_{r,l} / H \qquad (27)$$

The geotechnical criterion requires that the safety factor against the global sliding mechanism must be equal to or higher than the required value ($FS_{gs,r}$) for both the short- and long-term conditions as:

$$G_7(X) = FS_{gs,s} \geq FS_{gs,r} \qquad (28)$$

$$G_8(X) = FS_{gs,l} \geq FS_{gs,r} \qquad (29)$$

In addition, to ensure an adequate safety factor against the global sliding along the footing base, it is advisable to enforce additional constraints of the local sliding at each footing corner. This requirement is important and necessary, particularly for the long-term condition since there is a significant difference in the applied normal stress among the two footing corners, i.e., $q_{\max}$ (corner 1) and $q_{\min}$ (corner 2). As a result, the interface shear resistance at each corner is different, which results in a possible progressive local sliding failure. On the other hand, the short-term condition gives rise to the interface shear resistance, which is independent of those applied normal stresses because of the $\phi = 0$ concept. Thus, the short-term stability of the global sliding gives the same constraint as that of the local sliding. Thus, there is no need to enforce the constraint of the short-term stability of the local sliding.

For a generality of the formulation, the local sliding is enforced for both the short-term and long-term conditions. The interface shear resistance at each corner of the footing for both the short-term condition (corner 1, $\tau_{i1,s}$; corner 2, $\tau_{i2,s}$) and the long-term condition (corner 1, $\tau_{i1,l}$; corner 2, $\tau_{i2,l}$) can be calculated as:

$$\tau_{i1,s} = \tau_{i2,s} = s_{ui} \qquad (30)$$

$$\tau_{i1,l} = c_i' + q_{\max} \tan(\delta') \qquad (31)$$

$$\tau_{i2,l} = c_i' + q_{\min} \tan(\delta') \qquad (32)$$

Based on the effective width concept of the footing, the average applied shear stress (τ_{avg}) for each footing corner is given as:

$$\tau_{avg} = H / B' \qquad (33)$$

The ratio of the interface shear resistance to the applied average shear stress at each footing corner defines the safety factor against the local sliding failure for the short-term condition (corner 1 $FS_{ls1,s}$; corner 2 $FS_{ls2,s}$) and the long-term condition (corner 1 $FS_{ls1,l}$; corner 2 $FS_{ls2,l}$). These expressions are given as:

$$FS_{ls1,s} = \tau_{i1,s} / \tau_{avg} \qquad (34)$$

$$FS_{ls2,s} = \tau_{i2,s} / \tau_{avg} \qquad (35)$$

$$FS_{ls1,l} = \tau_{i1,l} / \tau_{avg} \qquad (36)$$

$$FS_{ls2,l} = \tau_{i2,l} / \tau_{avg} \qquad (37)$$

The geotechnical criterion requires that the safety factor against the local sliding failure must be equal to or greater than that of the required value ($FS_{ls,r}$) as:

$$G_9(X) = FS_{ls1,s} \geq FS_{ls,r} \qquad (38)$$

$$G_{10}(X) = FS_{ls2,s} \geq FS_{ls,r} \qquad (39)$$

$$G_{11}(X) = FS_{ls1,l} \geq FS_{ls,r} \qquad (40)$$

$$G_{12}(X) = FS_{ls2,l} \geq FS_{ls,r} \qquad (41)$$

2.2 Structural constraints of reinforced concrete

Fig. 5 shows the shear-force and bending-moment diagrams along the base of the footing generated from a linear distribution of pressure under the footing. For convenience, by neglecting the reduction effect from the concrete weight and the weight of the back-filled soil, the applied shear force (V_{cen}) and the bending moment (M_{cen}) calculated from the overturning side at the centre of base footing are given as:

$$V_{cen} = (q_{\max} + q_{cen}) x_1 / 4 \qquad (42)$$

$$M_{cen} = q_{cen}\, x_1^2 / 8 + (q_{\max} + q_{cen}) / 12 \qquad (43)$$

where $q_{cen} = 0.5(q_{max} + q_{min})$.

It should be noted that the shear force and the bending moment at the centre of the footing are slightly higher than those at the critical sections given by the design code [34]. According to the ACI code [34], there are two critical sections of the shear force: 1) the beam shear type; and 2) the punching shear type. The former and the latter happen at the distances $t = W_p/2 \pm d$ (V_b^+ and V_b^-) and $t = W_p/2 \pm d/2$ (V_p^+ and V_p^-) measured from the centre of the footing, where d is the effective depth of the base of the footing. The critical section of the bending moment happens at the pedestal edge or the distance $t = \pm W_p/2$ (M_b^+ and M_b^-) measured from the footing centre. Instead of using the exact calculation given by the design code, this analysis adopts the approximated values of the shear force (V_{cen}) and the bending moment (M_{cen}) at the centre of the footing shown in the expressions (42) and (43) as the substitutes for the values at the critical sections. If the calculations of the shear force and the moment follow the code, four constraints are needed to enforce the shear force and the moment on the left- and right-hand sides at the critical sections. However, since the modified calculations for the shear force and the moment at the centre give rise to the largest values, only two constraints are required. Thus, the use of maximum values for the shear force and the moment at the centre are adopted for reasons of convenience and conservatism.

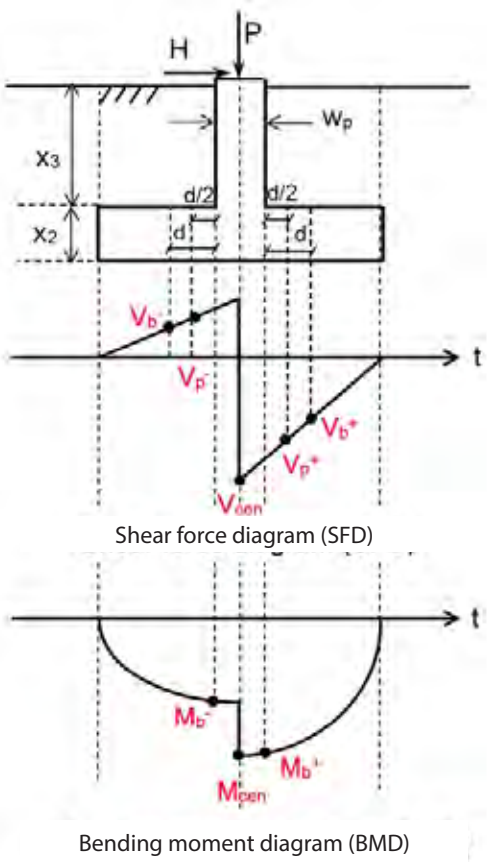

Figure 5. Shear-force and bending-moment diagrams along the base of the footing.

In this paper, the classical design code of the working stress method (e.g., Ricketts et al. [35]) is used to evaluate the allowable shear resistance and the bending

moment of the reinforced concrete footing. Based on this method, the allowable shear force of the concrete footing can be calculated as:

$$V_c = 29\sqrt{f_c'/100}bd \qquad (44)$$

where

f_c' = Unconfined compressive strength of concrete (kPa)
b = 1 unit length of footing (m)
d = Effective depth of slab footing = x_3 - c_v (m)
c_v = Effective concrete covering (m)

The allowable moment resistances of the reinforced concrete footing calculated from the concrete (M_c) and the steel reinforcement (M_s) are defined as:

$$M_c = Rbd^2 \qquad (45)$$

$$M_s = f_s jdx_4 \qquad (46)$$

where

$R = 0.5f_c kj$
$f_s = 0.5f_y \leq 170000$ kPa
f_y = Tensile strength of steel (kPa)
j = 1 - k/3
k =1/(1 + f_s/(nf_c))
$f_c = 0.45\, f_c'$
$n = E_s/E_c$
E_s = Young's modulus of steel = 2.04×10^8 kPa
E_c = Young's modulus of concrete (kPa) = $1521000\sqrt{f_c'/100}$

The first structural concrete criterion requires that the allowable shear force (V_c) of concrete must be equal to or greater than the approximated shear force at the critical section (V_{cen}). Moreover, the other criterion requires that the allowable moment resistance from the steel (M_s) must be equal to or greater than the approximated bending moment at the critical section (M_{cen}). These two criteria can be written as:

$$G_{13}(X) = V_c - V_{cen} \geq 0 \qquad (47)$$

$$G_{14}(X) = M_s - M_{cen} \geq 0 \qquad (48)$$

In order to design a single steel reinforcement at the bottom face of the footing base, it is necessary to enforce an additional constraint of the approximated bending moment at the critical section (M_{cen}) to be equal to or smaller than the allowable moment of the concrete (M_c) as:

$$G_{15}(X) = M_c - M_{cen} \geq 0 \qquad (49)$$

Finally, in addition to the structural constraints of the reinforced concrete criteria, it is necessary to specify the maximum and minimum allowable limits of the design variables since most optimization solvers require their searching ranges. The range of footing width, x_1, is defined as x_1 = 0.25–3.0m. The footing thickness, x_2 , and the soil embedment depth, x_3 , are in the range 0.5–2.0m. Finally, 0.2–5.0% of the total area of the footing base is used for the main steel reinforcement, x_4 . These maximum and minimum limits are converted to the inequality constraints as follows:

$$G_{16}(X) = x_1 - 0.25 \geq 0 \qquad (50)$$

$$G_{17}(X) = 3 - x_1 \geq 0 \qquad (51)$$

$$G_{18}(X) = x_2 - 0.5 \geq 0 \qquad (52)$$

$$G_{19}(X) = 2 - x_2 \geq 0 \qquad (53)$$

$$G_{20}(X) = x_3 - 0.5 \geq 0 \qquad (54)$$

$$G_{21}(X) = 2 - x_3 \geq 0 \qquad (55)$$

$$G_{22}(X) = x_4 - 0.002bx_2 \geq 0 \qquad (56)$$

$$G_{23}(X) = 0.05bx_2 - x_4 \geq 0 \qquad (57)$$

2.3 Objective function and optimization form

The objective function ($F(X)$) of the proposed optimization problem for a continuous footing is to minimize the total cost of the material in the strip footing, including the price of the concrete for the entire footing and the price of the main steel reinforcement of the footing slab. This objective function can be written as:

$$Minimize\ F(X) = Minimize\,(u_c(x_1x_2 + W_p x_3) + u_s x_1 x_4 \gamma_s) \qquad (58)$$

where

γ_s = Unit weight of steel
u_c = Unit price of concrete per unit volume (i.e., US\$/m^3)
u_s = Unit price of steel reinforcement per unit weight (i.e., US\$/kN)

The resulting numerical optimization of the dimension and reinforcement for a continuous footing leads to the constrained nonlinear programming, which has the form:

$$Minimize\ F(X) \qquad (59)$$

$$Subject\ to\text{: } G_i(X) \geq 0,\ \ i = 1..23$$

It should be noted that both the objective function and the geotechnical and structural constraints are nonlinear in terms of four unknown design variables and there are 18 nonlinear constants in this optimization.

There are two classes of optimization algorithm that can be used to solve the formulated optimization problem shown in expression (59). The first class is to apply the gradient-based algorithm of the optimization (e.g., NLPSolve [36], FindMinimum [37], fmincon [38], and Knitro [39]), while the other is to employ the free-derivative type of optimization (e.g., MIDACO [27, 28, 29, 30], ga [40], Nminimize [41], and Particle-swarm optimization [42, 43]). The gradient-based approach to optimization has the advantages such that it can efficiently determine the optimal solution with a rapid speed with the help of the first and second derivatives of the objective function and the constraints. Several algorithms of the gradient-based optimization approach can be found in Venkataraman [44]. On the other hand, the gradient-based technique of the optimization suffers a major drawback of being the local optimization, where its searching can be trapped into a local optimal solution, not the global optimal solution. Thus, several trials of other values of the decision variables must be performed in order to determine the global optimal solution.

Instead of using the classical technique of local optimization, which requires a first- and second-evaluations derivative approach and changes to the initial values of the variables, the optimal solution of the formulated optimization can also be solved using the technique of global optimization, such as evolutionary algorithms (Genetic algorithm [40, 45], Differential evolution [41]), swarm-based optimization algorithms (Particle-swarm optimization [42, 43], Ant-colony optimization [27, 28, 29, 30]). In this paper, the proposed optimization problem is coded in MATLAB and the optimal solution of the proposed formulation is solved using a state-of-the-art solver, MIDACO [27, 28, 29, 30].

MIDACO is an extended ant-colony optimization that is one of the swarm-based optimization algorithms. A distinct feature of this solver is that it employs an evolutionary metaheuristic search strategy to determine the global optimal solution from the search space in an intelligent and efficient way, as if ants seek the best path between their colony and a source of food. The search space is generated from the multi-kernel Gaussian probability density function. In addition, MIDACO is a self-adaptive algorithm to automatically determine the global optimal solution rather a local optimal solution. The major advantage of MIDACO is that there is no need to change the initial value of the decision variables by the users. Furthermore, the algorithm does not require the property of differentiability of the first or second derivatives for the nonlinear objective function or nonlinear equality or inequality constraints. Since MIDACO is a global optimization algorithm, it ensures that the computed solution from this software corresponds to the global optimal solution of the continuous footing that is subjected to the vertical and horizontal loads. Details of this solver are not within the scope of this study, but can be found in [27, 28, 29, 30].

All the analyses of the optimal design for a continuous footing are carried out on a personal computer, Windows 7 operating system, Intel Core I7-4770 CPU, @ 3.40 GHz and 8 GB memory.

3 RESULTS AND DISCUSSIONS

Table 1 lists all the input parameters used for demonstrating the application of the proposed optimization method in practice. Those parameters represent the actual conditions of the strip footing design. This continuous footing is used to support the stacker machine moving on the rail on top of the strip footing. Based on the results of triaxial testing, the soil is classified as a hard clay, whose total stress parameters are s_u = 150 kPa and the effective soil parameters are c' = 6 kPa and ϕ' = 30° The slow-moving stacker generates the static applied vertical and horizontal loads as P = 400 kN/m and H = 40 kN/m. The unit prices of the concrete and steel reinforcements are u_c = 83.33 US$/m^3 and u_s = 733.33 US$/ton (metric), based on the average unit costs in Thailand.

Table 1. Input parameters for the optimal design of the continuous footing.

Input parameters	Value
Applied vertical load, P (kN/m)	400
Applied horizontal load, H (kN/m)	40
Width of pedestal, W_p (m)	0.7
Total unit weight of soil, γt (kN/m^3)	20.0
Undrained shear strength of soil, s_u (kPa)	150
Effective cohesion, c' (kPa)	6.0
Effective friction angle, ϕ'	30°
Unit weight of concrete, γ_c (kN/m^3)	24
Unconfined compressive strength of concrete, f_c' (kPa)	28000
Effective concrete covering, c_v (m)	0.09
Unit weight of steel, γ_s (kN/m^3)	78.5
Tensile strength of steel, f_y (kPa)	400000
Unit price of concrete, u_c (US$/m^3)	83.33
Unit price of steel reinforcement, u_s (US$/ton)	733.33
Required safety factor for bearing, $FS_{b,r}$	3.0
Required safety factor for overturning, $FS_{ov,r}$	2.5
Required safety factor for global sliding, $FS_{gs,r}$	2.5
Required safety factor for local sliding, $FS_{ls,r}$	1.5

Table 2. The optimal solution of the continuous footing.

Design variables	Value
Footing width, x_1 (m)	2.839
Footing thickness, x_2 (m)	0.886
Soil embedment depth, x_3 (m)	0.5
Cross-sectional area of reinforcement, x_4 (m^2/m)	17.724×10^{-4}

The proposed optimization presented in Section 2 is applied to determine the optimal solution of this continuous footing. In this analysis, the nonlinear minimization problem is programmed in MATLAB and solved by MIDACO [27, 28, 29, 30] using the MATLAB toolbox. It should be noted that there is no need to try several initial solutions in order to ensure that the obtained optimal solution is the global minimum since MIDACO is the global optimization algorithm. Table 2 summarizes the global optimal solution of this actual case study using MIDACO. This solver handles the objective function and constraints as a black-box function or library. The constraints must be converted into the standard form as $G_i(X) \geq 0$ or $G_i(X) = 0$. The user needs to provide a function call to the optimization problem, i.e., objective function and constraints, which evaluates the objective function $F(X)$ and the constraints $G_i(X)$ for a given design variable X. The MIDACO solver does not require the user to determine the explicit form of the constraints in terms of the design variables x_1, x_2 … x_n. Several local variables in a function call can be used to store the values of some expressions, which are functions of the design variables. Then, the function calls return the computed value of the objective function and all the constraints back to MIDACO.

The stopping criterion in MIDACO was setup to find the minimum cost of the function for a period of 5 minutes during the optimization. This timing was sufficient to find the global optimal solution of the selected problem consisting of four design variables. Within this timing, the cost of the function converged to the lowest value during the running and was verified by manual checking.

A detailed result of the analysis is examined to verify which constraints are active and control the design. Table 3 lists each condition for all the required geotechnical and structural constraints. The active constraint $[G_i(x) = 0]$ means that the expression produces the equality sign, while the inactive constraint $[G_i(x) > 0]$ produces the inequality sign. The controlled design conditions or the active constraints are listed as follows:

1) Long-term safety factor for the bearing-capacity failure based on the stress calculated using $FS_{bs,l}$ $[G_2(x) = 0]$

Table 3. Results of each design constraint.

Design constraint	Value
Short-term safety factor for bearing-capacity stress, $FS_{bs,s}$ $[G_1(x)>0]$	3.95
Long-term safety factor for bearing-capacity stress, $FS_{bs,l}$ $[G_2(x)>0]$	3.00
Minimum applied pressure, σ_{min} (kPa) $[G_3(x)>0]$	136.4
Short-term safety factor for bearing force, $FS_{bf,s}[G_4(x)>0]$	4.47
Long-term safety factor for bearing force, $FS_{bf,l}$ $[G_5(x)>0]$	3.39
Safety factor for overturning, FS_{ov} $[G_6(x)>0]$	13.54
Short-term safety factor for global sliding, $FS_{gf,s}$ $[G_7(x)>0]$	4.75
Long-term safety factor for global sliding, $FS_{gf,l}[G_8(x)>0]$	3.39
Short-term safety factor for local sliding corner 1, $FS_{ls1,s}$ $[G_9(x)>0]$	4.75
Short-term safety factor for local sliding corner 2, $FS_{ls2,s}$ $[G_{10}(x)>0]$	4.75
Long-term safety factor for local sliding corner 1, $FS_{ls1,l}$ $[G_{11}(x) >0]$	3.82
Long-term safety factor for local sliding corner 2, $FS_{ls2,l}$ $[G_{12}(x)>0]$	2.50
Allowable shear force of concrete, V_c (kN/m) $[G_{13}(x)=0]$	329
Allowable bending moment of steel , M_s (kNm/m) $[G_{14}(x)=0]$	207
Allowable bending moment of concrete section M_c (kNm/m) $[G_{15}(x)>0]$	948
Minimum area of steel reinforcement (cm^2/m) $[G_{16}(x)>0]$	15.377
Minimum thickness of footing (m) $[G_{17}(x)>0]$	0.25
Minimum soil embedment depth (m) $[G_{18}(x)=0]$	0.5

2) Allowable shear force of concrete, V_c $[G_{13}(x) = 0]$
3) Allowable bending moment of steel, M_s $[G_{14}(x) = 0]$
4) Minimum soil embedment depth, $[G_{18}(x) = 0]$.

It is clear that there are four active constraints, which are equal to the numbers of design variables. However, the results of these four active constraints do not imply that they are always active for other cases. Similarly, the remaining inactive constraints may not always be irrelevant to the design. In general, the controlled design constraints or the active expressions depend on the relative magnitude of the vertical and horizontal loads, the soil parameters of the short- and long-term conditions, and the required safety factors for each failure mechanism. For example, the constraint of the compressive stress for the minimum applied pressure or the global sliding may become active and control the design for some cases of the input parameters of the loading, the soil parameters, the required safety factor, and the structured parameters.

4 MAJOR LIMITATION OF THE PROPOSED OPTIMAL DESIGN FOR CONTINUOUS FOOTINGS

It should be noted that the proposed optimal design for continuous footings has a major limitation, such that the single steel reinforcements or only the bottom bars are used in the footings. In general, continuous footings with double steel reinforcements may be the most economical scenario, instead of a single reinforcement. To achieve this design consideration, another new design variable, x_5, the cross-sectional area of the top reinforcements, must be introduced into the proposed optimization problem. In addition, the objective function must be modified to include the cost of the top bar reinforcements. Additional constraints of the reinforced concrete section with a double reinforcement must also be added to the formulated problem, together with the upper and lower limits of this new variable (i.e., x_5 = 0–10% of the total area of the footing base). As a result, this revised optimization problem is the most economical formulation that determines the optimal design consideration, including both single and double reinforcements of the continuous footings. For example, if the optimal solution yields the result such that $x_5 = 0$, this solution corresponds to the single steel reinforcement. On the other hand, if the optimal solution turns out to be $x_5 \neq 0$, this solution corresponds to the double steel reinforcements.

5. CONCLUSIONS

This paper presents a numerical technique for optimizing the dimensions and reinforcement of a continuous footing subjected to vertical and horizontal loads. The mathematical formulations lead to nonlinear programming, whose objective function is to determine the minimum cost of the reinforced concrete footings, including concrete and steel reinforcements. The analysis considers four design variables, i.e., the footing width, the footing thickness, the footing embedment, and the steel reinforcement. The continuous footing subjected to the vertical and horizontal loads generates the complex geotechnical and structural constraints in terms of the design variables, totalling 18 nonlinear constraints. The major advantage of the proposed method is that all the required constraints of the geotechnical and structural designs for the short-term and long-term stability considerations are optimized simultaneously. As a result, the final analysis yields the most optimal dimension of the foundation and the required reinforcements for both types of stability consideration. The proposed method is more efficient and convenient than most conventional footing designs where the short-term and long-term analyses are looked at separately. Moreover, a classical or conventional design may have to initially assume some design variables, such as the footing thickness or the footing width. Therefore, it is not always guaranteed that the assumed footing dimensions and reinforcement are the most optimal design.

The formulated optimization problem for the continuous footing is solved by the state-of-the-art ant-colony optimization solver, MIDACO, which is a global optimization algorithm and does not require any derivative of the objective function and the constraints, and does not require changing the initial values of the decision variables. The proposed method is applied to design the continuous foundation of an actual stacker machine used in bulk-material handling applications. The numerical optimization by MIDACO makes it possible to efficiently analyse 18 complex nonlinear constraints from the geotechnical and structural criteria, resulting in the global optimal solution in a single analysis for both the short-term and long-term conditions.

REFERENCES

[1] Available from: http://en.wikipedia.org/wiki/Stacker
[2] Available from: http://en.wikipedia.org/wiki/Reclaimer
[3] Guerra, A., Kiousis, P.D. 2006. Design optimization of reinforced concrete structures. Computers and Concrete 3, 5, 313-334.
[4] Kortnik, J. 2009. Optimization of the high safety pillars for the underground excavation of natural stone blocks. Acta Geotechnica Slovenica 6, 1, 61-73.
[5] Gil-Martin, L.M., Hernandez-Montes, E., Aschheim, M. 2010. Optimization of piers for retaining walls. Structural and Multidisciplinary Optimization 41, 6, 979-987. doi: 10.1007/s00158-010-0481-2
[6] Mendjel, D., Messast, S. 2012. Development of limit equilibrium method as optimization in slope stability analysis. Structural Engineering and Mechanics 41, 3, 339-348. doi: 10.12989/sem.2012.41.3.339
[7] Jelusic, P., Zlender, B. 2013. Soil-nail wall stability analysis using ANFIS. Acta Geotechnica Slovenica 10, 1, 35-48.
[8] Rhomberg, E.J., Street, W.M. 1981. Optimal design of retaining walls. Journal of Structural Division, ASCE 107, 5, 992-1002.
[9] Saribas, A., Erbatur, F. 1996. Optimization and sensitivity of retaining structures. Journal of Geotechnical Engineering, ASCE 122, 8, 649-656.
[10] Basudkar, P.K., Lakshman, B. 2006. Optimal cost design of cantilever retaining walls. Proc. Indian Geotechnical Conference, Chennai, 525-528.
[11] Alshawi, F.A.N., Mohammad, A.L., Farid, B.J. 1988. Optimum design of tied-back retaining walls. The Structural Engineering 66, 6, 97-105.
[12] Ceranic, B., Fryer, C., Baines, R.W. 2001. An Application of Simulated Annealing to the Optimum Design of Reinforced Concrete Retaining Structures.

Computers and Structures 79(17), 1569-1581. doi: 10.1016/S0045-7949(01)00037-2

[13] Castillo, E., Mínguezb, R., Teránb, A.R., Fernández-Cantelic, A. 2004. Design and Sensitivity Analysis using the Probability-Safety-Factor Method: An Application to Retaining Walls. Structural Safety 26, 159-179. doi: 10.1016/S0167-4730(03)00039-0

[14] Babu, G.L.S., Basha, B.M. 2008. Optimum Design of Cantilever Retaining Walls Using Target Reliability Approach. International Journal of Geomechanic ASCE 8, 240-252.

[15] Khajehzadeh, M., Taha, M.R., El-Shafie, A., Eslami, M. 2010. Economic Design of Retaining Wall Using Particle Swarm Optimization with Passive Congregation. Australian Journal of Basic and Applied Sciences 4, 5500-5507.

[16] Ghazavi, M., Bazzazian Bonab, S. 2011. Optimization of reinforced concrete retaining walls using ant colony method. Proc., 3rd Int. Symposium on Geotechnical Safety and Risk (ISGSR), Germany.

[17] Camp, C.V., Akin, A. 2012. Design of retaining walls using big bang-big crunch optimization. Journal of Structural Engineering 138(3), 438-448.

[18] Pourbaba, M., Talatahari, S., Sheikholeslami, R. 2013. A chaotic imperialist competitive algorithm for optimum cost design of cantilever retaining walls. KSCE Journal of Civil Engineering 17(5), 972-979. doi: 10.1007/s12205-013-0283-3

[19] Papazafeiropoulos, G., Plevris, V., Papadrakakis, M. 2013. Optimum design of cantilever walls retaining linear elastic backfill by use of genetic algorithm. In: Proc., 4th ECCOMAS Thematic Conference on Computational Methods in Structural Dynamics and Earthquake Engineering, Greece.

[20] Talatahari, S., Sheikholeslami, R. 2014. Optimum design of gravity and reinforced retaining walls using enhanced charged system search algorithm. KSCE Journal of Civil Engineering 18(5), 1464-1469. doi: 10.1007/s12205-014-0406-5

[21] Sadoglu, E. 2014. Design optimization for symmetrical gravity retaining walls. Acta Geotechnica Slovenica 11, 1, 61-73.

[22] Banichuk, N.V., Ragnedda, F., Serra, M. 2000. Dynamic problems of shape optimal design for shallow curved plates. Structural Multidiscipline Optimization 19, 303-310.

[23] Valliappan, S., Hakam, A. 2001. Finite element analysis for optimal design of foundation due to dynamic loading. International Journal for Numerical Methods in Engineering, 52, 5-6, 605-614. doi: 10.1002/nme.296

[24] Salac, P. 2002. Optimal design of an elastic circular plate on an unilateral elastic foundation. I: Continuous problems, ZEITSCHRIFT FUR ANGEWANDTE MATHEMATIKUND MECHANIK 82, 1, 21-32.

[25] Salac, P. 2002. Optimal design of an elastic circular plate on an unilateral elastic foundation. II: Approximate problems, ZEITSCHRIFT FUR ANGEWANDTE MATHEMATIK UND MECHANIK 82, 1, 33-42.

[26] Truman, K.Z., Hoback, A.S. 1992. Optimization of steel piles under rigid slab foundations using optimality criteria. Structural and Multidisciplinary Optimization 5, 1, 30-36.

[27] Schlueter, M., Egea, J.A., Banga, J.R. 2009. Extended ant colony optimization for non-convex mixed integer nonlinear programming. Computer Operation Research 36(7), 2217–2229. http://dx.doi.org/10.1016/j.cor.2008.08.015

[28] Schlueter, M., Egea, J.A., Antelo L.T., Alonso A. A., Banga, J.R. 2009. An extended ant colony optimization algorithm for integrated process and control system design. Industrial & Engineering Chemistry Res. 48(14), 6723-6738. doi: 10.1021/ie8016785

[29] Schlueter, M., Gerdts M., Ruckman J. J. 2012. A numerical study of MIDACO on 100 MINLP benchmarks. Optimization 61(7), 873-900. DOI: 10.1080/02331934.2012.668545

[30] Schlueter, M. 2013. MIDACO, Global optimization software for mixed integer nonlinear programming. Software available at http://www.midaco-solver.com.

[31] Braja, M. Das 2010. Principles of foundation engineering, 7th ed., Cengage Learning, USA.

[32] Bowles, J. 1996. Foundation analysis and design, 5th ed., McGraw-Hill Inc., USA.

[33] Coduto, D.P. 2001. Foundation Design, 2nd ed., Prentice Hall, New Jersey.

[34] ACI 1999. Building Code Requirements for Structural Concrete (ACI 318-99), American Concrete Institute.

[35] Ricketts, J.T., Loftin, M.K., Merritt, F.S. 2003. Standard Handbook for Civil Engineers 5th ed., McGraw-Hill Inc., USA.

[36] Waterloo Maple Inc. 2011. Maple Help: NLPSolve Available from: http://www.maplesoft.com/support/help/Maple/view.aspx?path=Optimization/NLPSole.

[37] Wolfram 2014. Mathematica Help: FindMinimum, Available from: http://reference.wolfram.com/language/ref/FindMinimum.html.

[38] Mathworks 2014. Matlab Help: fmincon, Available from: http://www.mathworks.com/help/optim/ug/fmincon.html.

[39] Ziena Optimization 2011. Inc. KNITRO, Available from: http://www.ziena.com/knitro.htm.

[40] Mathworks 2014. Matlab Help: ga, Available from: http://www.mathworks.com/help/gads/ga.html.

[41] Wolfram 2014. Mathematica Help: NMinimize, Available from: http://reference.wolfram.com/language/ref/NMinimize.html.

[42] Kennedy, J., Eberhart, R. 1995. Particle swarm optimization, Proc. of the IEEE Int. Conf. on Neural Networks, USA.

[43] Mathworks 2014. Matlab Help: particleswarm, Available from: http://www.mathworks.com/help/gads/particle-swarm.html.

[44] Venkataraman, P. 2009. Applied optimization with MATLAB Programming, John Wiley & Sons, USA.

[45] Ingber, L., Rosen, B. 1992. Genetic algorithms and very fast simulated reannealing: a comparison, J. of Mathematical and Computer Modeling 16(11), 87-100.

REOLOŠKE LASTNOSTI MORSKIH SEDIMENTOV IZ LUKE KOPER

Jasna Smolar *(vodilni avtor)*
Univerza v Ljubljani,
Fakulteta za gradbeništvo in geodezijo
Jamova 2, Ljubljana, Slovenija
E-pošta: jasna.smolar@fgg.uni-lj.si

Matej Maček
Univerza v Ljubljani,
Fakulteta za gradbeništvo in geodezijo
Jamova 2, Ljubljana, Slovenija
E-pošta: matej.macek@fgg.uni-lj.si

Ana Petkovšek
Univerza v Ljubljani,
Fakulteta za gradbeništvo in geodezijo
Jamova 2, Ljubljana, Slovenija
E-pošta: ana.petkovsek@fgg.uni-lj.si

Ključne besede

morski sedimenti, Bingham-ov model, napetost na meji tečenja, plastična viskoznost, koaksialni valjasti reometri, mrtvi tok, Koprski zaliv

Izvleček

Sedimenti na morskem dnu so nenehno izpostavljeni valovanju in drugim motnjam, ki povzročajo njihovo premikanje. Premikanje lahko opišemo z numeričnimi modeli, ki vključujejo reološke parametre, odvisne od vrste zemljine (trdnine), volumske koncentracije, slanosti in preiskovalnih metod.

Ta članek opisuje preiskave reoloških lastnosti morskega sedimenta iz Luke Koper. Raziskave so bile izvedene z uporabo dveh koaksialnih valjastih reometrov (DV3T HB, Brookfield in ConTec Viscometer 5). Analiziran je vpliv volumna vzorca, razdalje med notranjim in zunanjim valjem in vrste uporabljenih vreten. Meritve so analizirane z uporabo Bingham-ovega modela. Za vsako meritev je bila izvrednotena meja med materialom, ki teče in tistim, ki ne teče. Kjer je bilo potrebno, je bila za vrednotenje reoloških parametrov, namesto radija zunanjega cilindra uporabljena izračunana meja. Z uporabo te metode je bilo ugotovljeno dobro ujemanje rezultatov. Rezultati so primerljivi s podatki iz literature za podobne zemljine. ConTec Viscometer 5, ki je prvenstveno razvit za preiskave malt in betonov, je bil prepoznan, kot primeren tudi za preiskave sedimentov.

RHEOLOGICAL PROPERTIES OF MARINE SEDIMENTS FROM THE PORT OF KOPER

Jasna Smolar *(corresponding author)*
University of Ljubljana,
Faculty of Civil and Geodetic Engineering
Jamova 2, Ljubljana, Slovenia
E-mail: jasna.smolar@fgg.uni-lj.si

Matej Maček
University of Ljubljana,
Faculty of Civil and Geodetic Engineering
Jamova 2, Ljubljana, Slovenia
E-mail: matej.macek@fgg.uni-lj.si

Ana Petkovšek
University of Ljubljana,
Faculty of Civil and Geodetic Engineering
Jamova 2, Ljubljana, Slovenia
E-mail: ana.petkovsek@fgg.uni-lj.si

Keywords

marine sediments, Bingham model, yield stress, plastic viscosity, coaxial cylinder rheometer, plug flow, Bay of Koper

Abstract

Subaqueous, fine-grained, cohesive sediments are continuously fluidized by waves and other disturbances that cause their movement, which can be described with numerical models incorporating rheological parameters. The rheological behaviour depends on the soil (solid) type, the volume concentration, the salinity and the testing methods.

In this study, rheological investigations of marine sediments from the Port of Koper were carried out by using two coaxial cylinder rheometers (DV3T HB, Brookfield and ConTec Viscometer 5). The influence of the specimen volume, the size of the gap and the type of measuring spindles were analysed and compared.

The measured data were evaluated using the Bingham model. For each data set, the boundary between the sheared ("fluid") and the un-sheared ("solid") material was calculated and then the calculated boundary was used instead of the outer radius of the cylinder for the evaluation of the rheological parameters, where necessary.

A good comparison of the results was found when using this approach. The results are also in agreement with the literature data. The ConTec Viscometer 5, primarily designed for mortars and concrete, was shown to be also suitable for the investigation of sediments.

1 INTRODUCTION

Subaqueous sediments are continuously fluidized by waves and other disturbances that cause their transport over short or long distances. Sediment movements can also be accompanied by the migration of pollutants. To characterize the flow behaviours of sediments, numerical models of flow mechanics are used and the two rheological parameters, yield stress and viscosity, are required [1 - 6].

Recently, extensive investigations have been carried out in order to provide the rheological parameters of different types of subaqueous and subaerial mud and debris flows [3, 5, 7-18, among others]. The results show that the rheological parameters strongly depend on the soil (solid) type, the volume concentration, the salinity of the pore water, and the type and geometry of the rheometer [2, 6, 19].

In this study the rheological parameters of remolded marine sediments from the Port of Koper, Adriatic Sea, were investigated for the first time. The port is facing the permanent accumulation of fine-grained, cohesive sediments inside the existing waterways, while the wider

area of the Gulf of Trieste is facing the migration of pollutants [20-25, among others]. The prediction of the runout distances and the impacts due to the sediment transport are an important part of the risk analysis and mitigation measures in the port area.

The second goal of the study was to investigate how the use of different types of rheometers, specimen sizes and the measuring spindles can influence the results, reliability and repeatability of the measured rheological parameters.

2 RHEOLOGICAL BEHAVIOUR OF FINE GRAINED, COHESIVE SEDIMENTS

Soft cohesive sediments and slurries display non-Newtonian flow behaviour, which is both strain-rate and time dependent. This rheological behaviour is generally described by the relationship between the shear stress (τ) and the shear rate ($\dot{\gamma}$). The Bingham model is one of the simplest and most popular models for a description of pseudoplastic materials (Equation 1, Fig. 1 (a)) [5, 7, 9]. In this model the shear stress has two components, i.e., shear strength or yield stress (τ_y), and an increase of the shear stress due to shear rate and plastic viscosity (η_p).

$$\tau = \tau_y + \eta_p \cdot \dot{\gamma} \qquad (1)$$

Various types of rheometers were developed for investigating the rheological parameters of different materials (e.g., rotational rheometers/viscometers - coaxial cylinder, plate-plate, cone-plate; capillary viscometers and falling-ball viscometers) [26]. Rotational rheometers/viscometers with coaxial cylinders have been widely used for investigating the rheological parameters of sediments for decades [3, 4, 7-10, 27].

In coaxial cylinder rheometers, when high-yield-stress materials are tested, the material between the inner and the outer cylinder may not be entirely sheared. The boundary between the sheared "fluid" and un-sheared "solid" is called the plug radius (R_p) [28] (Fig. 1 (b)).

The plug radius is formed when the shear stress is equal to the yield stress and can be calculated as follows [28, 29]:

$$R_p = \sqrt{\frac{T}{\tau_y \cdot 2 \cdot \pi \cdot h}} \qquad (2)$$

where T is the torque (Nm), measured in the coaxial cylinder rheometer, and h is the height of the inner cylinder submerged in the material.

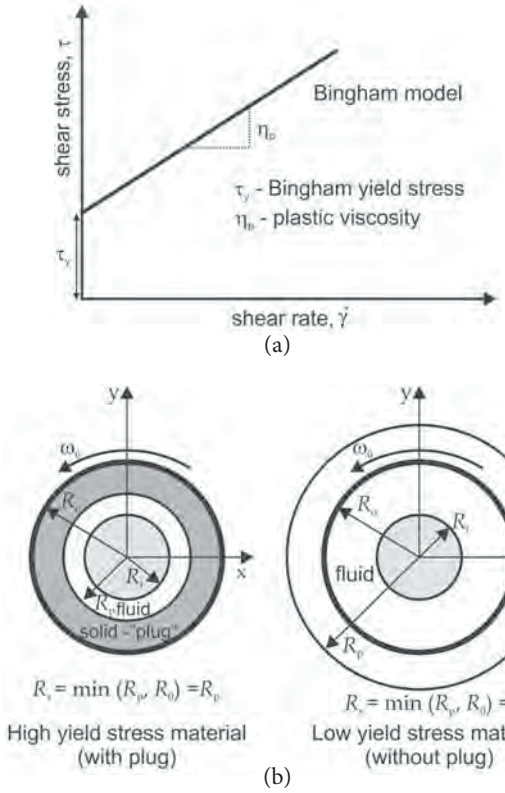

Figure 1. Bingham model (a), and top view of coaxial cylinder with sample (b) [28].

From the measured sets of rotational velocity (velocity of revolution) (N) and the corresponding torque (T), the Bingham yield stress (τ_y) and the plastic viscosity (η_p) can be calculated using Equation 3 and the least-squares method.

$$T = \frac{4 \cdot \pi \cdot h \cdot ln\left(\frac{R_s}{R_i}\right)}{\left(\frac{1}{R_i^2} - \frac{1}{R_s^2}\right)} \cdot \tau_y + \frac{8 \cdot \pi^2 \cdot h}{\left(\frac{1}{R_i^2} - \frac{1}{R_s^2}\right)} \cdot \eta_p \cdot N \qquad (3)$$

where $R_s = \min(R_p, R_o)$ (Fig. 1(b)).

Equation 3 was obtained by integrating the shear rates between the inner and outer cylinders in the coaxial cylinder rheometer and using the Bingham model [28].

For a graphical presentation of the flow curves, the shear rate is calculated using Equation 4.

$$\dot{\gamma} = \frac{T}{2 \cdot \pi \cdot R_i^2 \cdot h \cdot \eta_p} - \frac{\frac{T}{4 \cdot \pi \cdot h} \cdot \left(\frac{1}{R_i^2} - \frac{1}{R_s^2}\right)}{\eta_p \cdot ln\left(\frac{R_s}{R_i}\right)} + \frac{\omega_0}{ln\left(\frac{R_s}{R_i}\right)} \qquad (4)$$

where $\omega_0 = (2\pi/60)\, N$; N=RPM.

3 MATERIALS AND METHODS

3.1 Materials

The material used in this study is a fine-grained marine sediment from the Port of Koper. Table 1 presents the index properties and Fig. 2 shows a representative area of the grain size distribution. The investigated sediments consist mainly of illite, muscovite and chlorite [30].

The index tests show that salinity has no impact on the liquid limit and the plasticity index of the sediment (Table 1). The results are in good agreement with the literature data [31], [32] and others.

Table 1. Index properties of marine sediment.

Index properties	Material			
	marine sediment		marine clay*	
Natural water content, w_0 [33]	/	~80%	/	/
Salinity, s (g/L)	0	30	0	50
Liquid limit, w_L (%) [34]	64-67	69	72	74
Plasticity index, I_P (%) [34]	44-46	46	34	34
Water adsorption, w_A [35]	76-84	/	/	/

*Literature data [31].

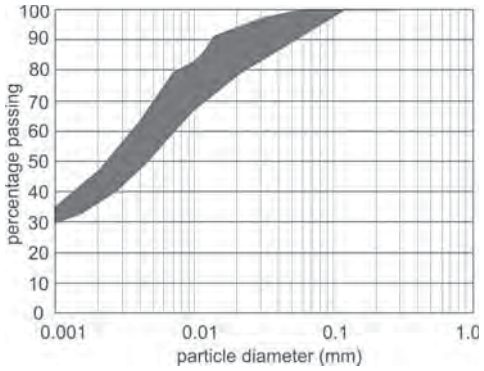

Figure 2. Representative area of grain size distribution.

3.2 Testing procedures

Two types of shear-rate-controlled coaxial cylinder rheometers were used: the DV3T HB (Brookfield) and the ConTec Viscometer 5. The main differences between these rheometers are the specimen volume and the gap size. All the investigations were carried out at room temperature (22–24 °C), on washed specimens without any salt content (s = 0 g/L).

3.2.1 DV3T HB Rheometer

Tests in the DV3T HB rheometer were conducted by using different combinations of smooth spindles (S), vanes (V) and chambers (Table 2, Fig. 3). In the evaluation of the results, the effective length of the spindles was used [36].

Table 2. Combinations of smooth spindles, vanes and chambers.

Combination	Glass beaker (GB)	Small sample adapter (SA)
Smooth spindle (S)	V_s ~ 800 ml Ro ~ 40 mm gap ~ 31-34 mm[1]	V_s ~ 7-14 ml Ro ~ 9.525 mm gap ~ 1.14-3.645 mm[1]
Vane (V)	V_s ~ 800 ml Ro ~ 40 mm gap ~ 23-34 mm[1]	/

[1] Gap size depends on the radius of the spindle or vane.
V_s – specimen volume, Ro – radius of outer cylinder, gap – distance between inner and outer cylinder

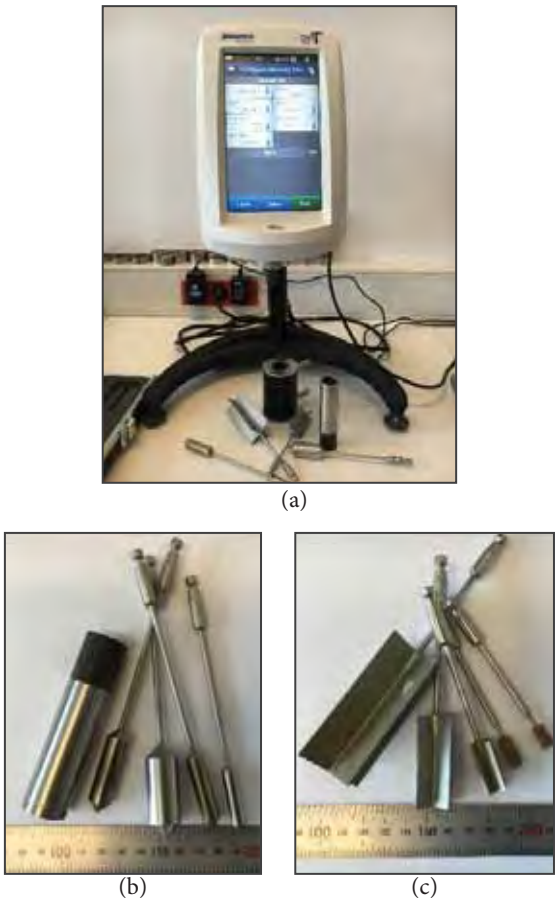

(a) (b) (c)

Figure 3. DV3T HB rheometer (a), small sample adapter with smooth spindles (b) and vanes (c).

Regardless of the combination of chamber and spindle, the "down curves" were measured. It consisted of measured values during decreasing the rotational velocity from 250 to 0.02 rounds/minute (RPM). Each step (at the desired rotational velocity) lasted until the spindle or vane had rotated for at least one revolution (360°) or at least 1 minute at velocities higher than 1 RPM. The resulting torque was calculated for each step as the average of the measured values after reaching equilibrium. During the investigation the outer cylinder was fixed, while the spindle or vane were rotating.

3.2.2 ConTec Viscometer 5

The ConTec Viscometer 5 (CTV 5) was primarily designed for the rheological testing of fresh mortars and concrete. It has an inner radius of 100 mm and an outer radius of 145 mm (with a 45 mm gap), while the height is 100 mm (Fig. 4). It allows investigations of materials with a maximum grain size of 22 mm.

Figure 4. ConTec Viscometer 5.

A pre-shear period of around 30 s is applied at the maximum rotational velocity to start the flow. During measurements the rotational velocity decreased in steps from 100 RPM to 6 RPM. The resulting torque was calculated from the 10 lowest measured values in 1 minute after 15 s of equilibration time. During the investigation the inner cylinder was fixed, while the outer one was rotating.

4 EXPERIMENTAL RESULTS

4.1 Results of tests

The physical properties of specimens are presented in Table 3.

The data, measured using different coaxial cylinder rheometers, were analyzed by using Equations 3 and 4, taking into account the radius R_s (Fig. 1). The comparison of the flow curves, determined by using two different rheometers and different vanes and spindles, are presented in Fig. 6.

Specimen S1 represents the densest specimen. During the test, a stable hollow was formed around the smooth spindle (Fig. 5).

The yield stress was measured separately with a laboratory vane at 0.25 RPM, on more than 140 specimens at a different liquidity index. The results are presented in Fig. 7 and compared with the literature data.

Table 3. Physical properties of specimens.

Specimen	water content, w (%)	liquidity index, I_L	volume concentration, C_v (%)
S1	79.5	1.34	32.2
S2	92.3	1.62	29.0
S3	103	1.86	26.7
S4	113	2.06	25.1
S5	130	2.44	22.4
S6	142	2.70	21.0

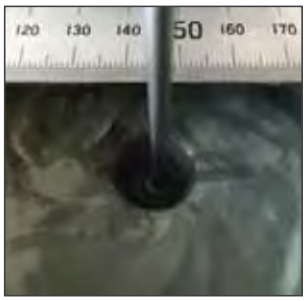

Figure 5. Stable hollow around the spindle during the investigation of S1.

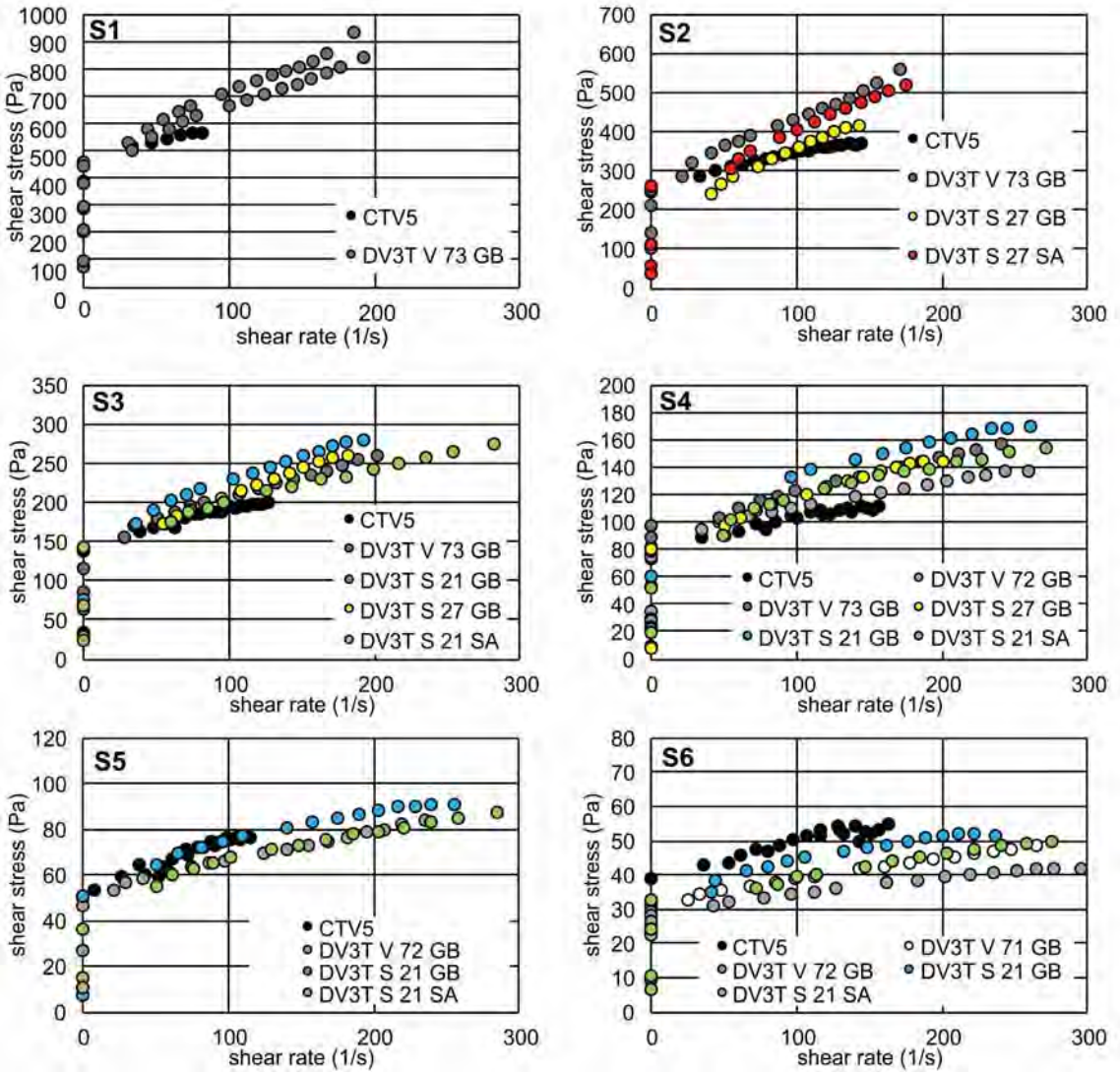

Figure 6. Flow curves of marine sediment for different water contents. Legend: CTV5 – ConTec Viscometer 5, DV3T – Rheometer DV3T HB, V – vane, S – spindle, 72 or 21 – number of vane or spindle, GB – glass beaker, SA – small sample adapter.

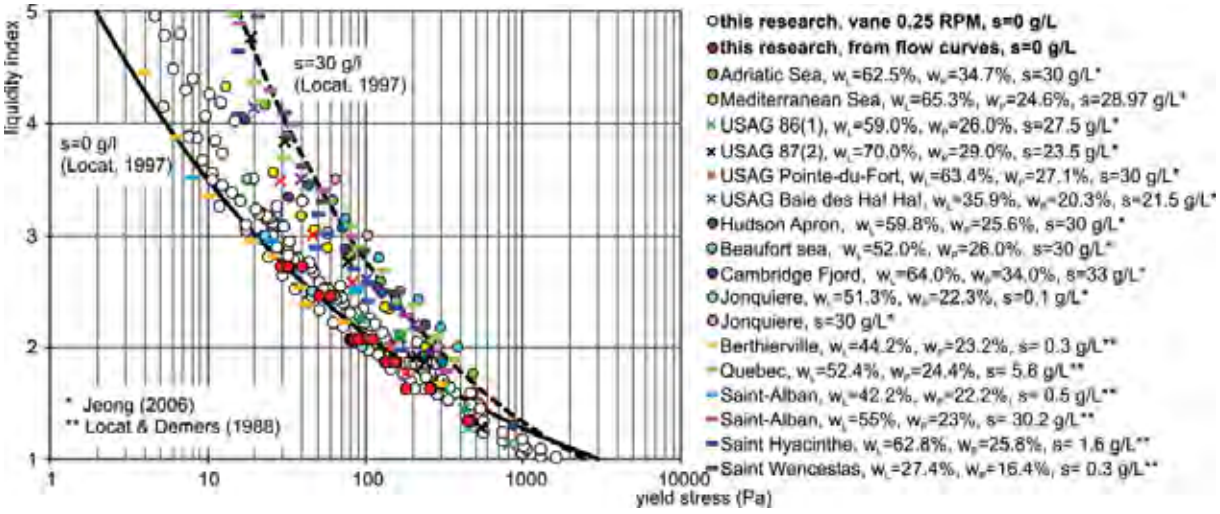

Figure 7. Yield stress and liquidity index of the investigated marine sediments in comparison with the literature data [9, 27, 37].

Table 4. Bingham rheological parameters of marine sediments, determined with different rheometers and spindles.

Specimen	S1		S2		S3		S4		S5		S6	
Parameter	τ_y	η_p	τ_y	η_p	τ_y	η_p	τ_y	η_p	τ_y	η_p	τ_y	η_p
CTV 5	476	1151	270	731	143	504	83.4	186	51.9	231	40.6	86
DV3T V71 GB	/	/	/	/	/	/	/	/	/	/	32.2	63
DV3T V72 GB	/	/	/	/	/	/	86.6-91.3	188-219	52.0	137	29.7	45
DV3T V73 GB	456-474	1998-2350	269	1637	149	561	97.1	247	/	/	/	/
DV3T 21S GB	/	/	/	/	159	660	113	229	61.2	128	34.1	85
DV3T 27S GB	/	/	186	1686	140	679	84.9	320	/	/	/	/
DV3T 21S SA	/	/	/	/	158	422	86.3	272	52.3	129	33.1	62
DV3T 27S SA	/	/	260	1457	/	/	/	/	/	/	/	/

τ_y (Pa), η_p (mPa·s)

4.2 Analysis of the measured rheological parameters

An analysis of the results shows that the rheometer type and the geometry of the spindles do not influence the results (Table 4). The observed scattering of the results seems to be more influenced by the experiment itself than by the type of rheometer.

4.3 Comparison of the measured parameters with the literature data

The results of the investigated marine sediments were analyzed in comparison with the literature data [9, 11-13, 15-18, 27] and by using the empirical relationships (Equations 5 to 7) for the calculation of the yield stress and plastic viscosity from the index test results [37].

$$\eta_p = \left(\frac{9.27}{I_L}\right)^{3.3} \quad (5)$$

$$\tau_y = \left(\frac{5.81}{I_L}\right)^{4.55} \quad (6)$$

$$\tau_y = \left(\frac{12.05}{I_L}\right)^{3.13} \quad (7)$$

where I_L is the liquidity index.

Equation 5 is valid for natural soft clays in the range of I_L between 1 and 5, where η_p represents only about 1/1000th of the total shearing resistance. Equation 6 is valid for very low salinity (s) sensitive clays and Equation 7 for clays with a salt content of about 30 g/l.

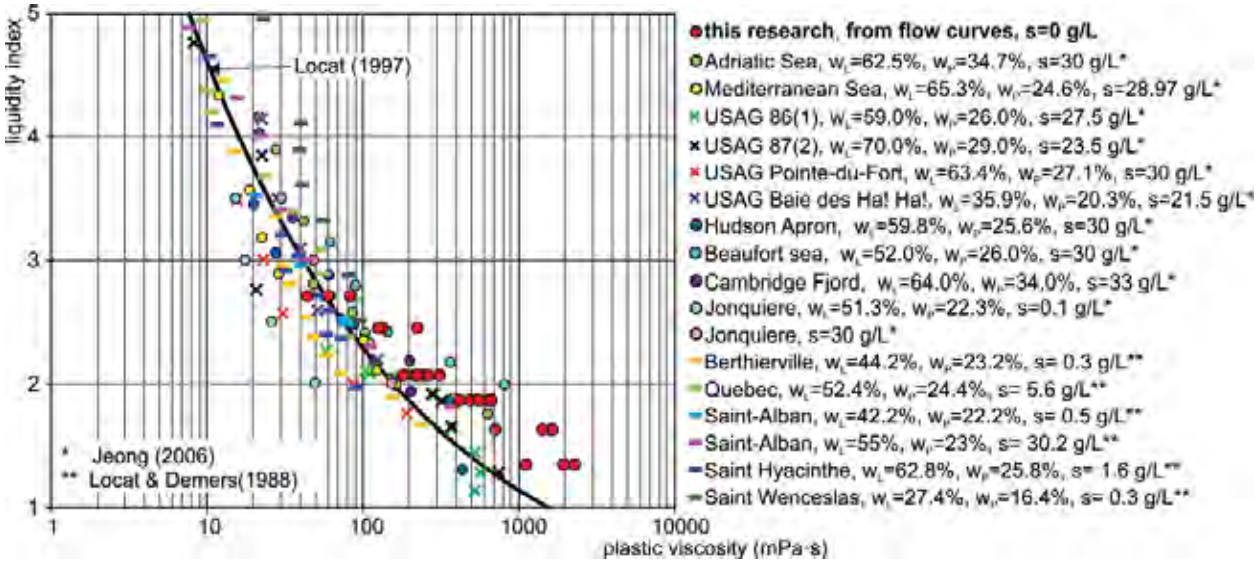

Figure 8. Plastic viscosity and liquidity index of the investigated marine sediments in comparison with the literature data [9, 27, 37].

Fig. 7 shows the yield stress and Fig. 8 the plastic viscosity, measured on sediments from the Port of Koper, in comparison with literature data. The index parameters (w_L,w_P) of the literature data are summarized in the legends of the figures. The black lines in Figs. 7 and 8 show the parameters calculated using empirical correlations (Equations 5 to 7). Both the shear stress and the plastic viscosity of the marine sediments from the Port of Koper are in relatively good agreement with the literature data. The yield stress is close to the values given by Equation 6, independently of the method. The plastic viscosity at the lower liquidity index is up to 4 times higher than that calculated from Equation 5. The same range of scatter was also found in the literature data.

One of the important factors that affect the rheological parameters is the soil texture. Thus, it is interesting to analyze the relationship between the index properties of the sediments and their rheological parameters (Fig. 9). The results of the investigated marine sediments fall close to clay-rich materials, which is in good agreement with the index properties given in Table 1.

5 CONCLUSIONS

The Bingham rheological parameters of cohesive marine sediments from the Port of Koper were, for the first time, determined by using a small DV3T HB rheometer and a large ConTec Viscometer 5. The measured data were analysed and compared to the literature data. The main conclusions are as follows:

(1) the investigated marine sediments behave as a Bingham-type viscoplastic fluid
(2) the rheological parameters (τ_y , η_p), calculated by using $R_s = \min(R_p, Ro)$, measured with both rheometers, are in the same range and are independent of the size of the gap
(3) the ConTec Viscometer 5 was found to be suitable for rheological investigations of the cohesive sediments
(4) the rheological parameters of the marine sediments from the Port of Koper are in good agreement with literature data and also with empirical correlations.

REFERENCES

[1] Yang, W., Yu, G., Tan, S. keat, Wang, H. 2014. Rheological properties of dense natural cohesive sediments subject to shear loadings. Int. J. Sediment Res. 29(4), 454–470.

[2] Faas, R.W., Reed, A.H. 2010. Comparative Analysis of Two Techniques for Determining the Rheological Properties of Fluid Mud Suspensions. Mar. Georesources Geotechnol. 28(4), 345–362.

[3] Jeong, S.W. 2014. The effect of grain size on the viscosity and yield stress of fine-grained sediments. J. Mt. Sci. 11(1), 31–40.

[4] Jeong, S.W., Locat, J., Leroueil, S. 2015. Geotechnical and Rheological Characteristics of Saguenay Fjord Sediments Near the Transition from Solid to Liquid. Mar. Georesources Geotechnol. 33(3), 239–252.

[5] Jeong, S.W., Locat,J., Leroueil, S., Malet, J.-P. 2010. Rheological properties of fine-grained sediment: the roles of texture and mineralogy. Can. Geotech. J. 47(10), 1085–1100.

[6] Jeong, S.W., Locat, J., Leroueil, S., Malet, J.-P. 2007. Rheological Properties Of Fine-Grained Sediments

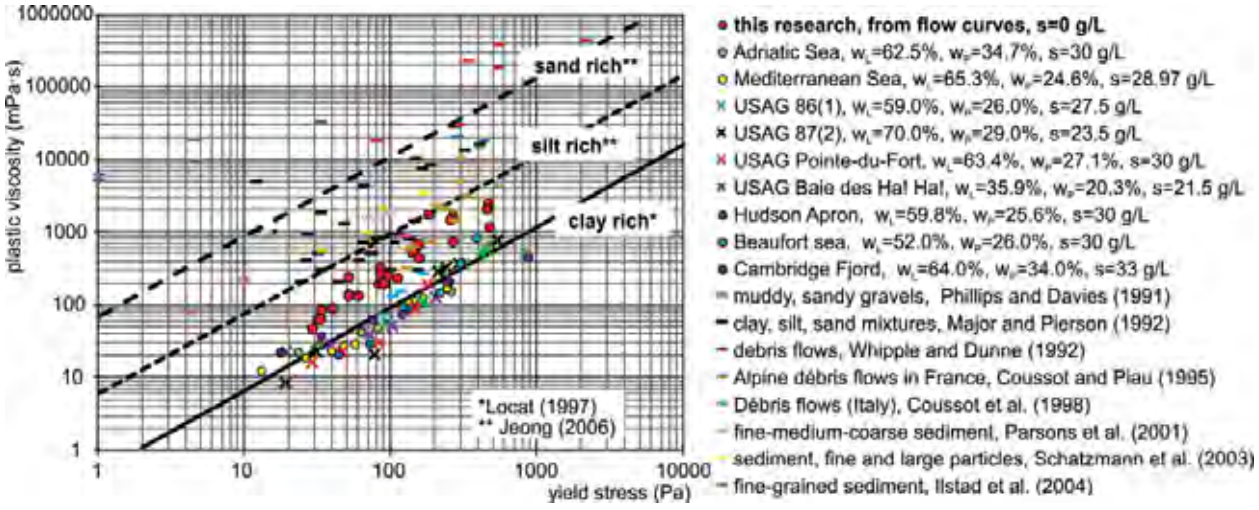

Figure 9. Yield stress versus plastic viscosity for a variety of soil types [9, 11–13, 15–18, 27].

In Modeling Submarine Mass Movements: The Role Of Texture, in V. Lykousis, D. Sakellariou, J. Locat (eds.), Submarine Mass Movements and Their Consequences, Volume 27 of the series Advances in Natural and Technological Hazards Research, Springer, Netherlands, pp.191-198.

[7] Jeong, S.W. 2013. Determining the viscosity and yield surface of marine sediments using modified Bingham models. Geosci. J. 17(3), 241–247.

[8] Jeong, S.W. 2013. The viscosity of fine-grained sediments: A comparison of low- to medium-activity and high-activity clays. Eng. Geol. 154, 1–5.

[9] Jeong, S.W. 2006. Influence of physico-chemical characteristics of fine-grained sediments on their rheological behavior. Ph.D. Thesis. Faculte de Sciences et Genie Universite Laval, Quebec.

[10] Jeong, S.W., Leroueil, S., Locat, J. 2009. Applicability of power law for describing the rheology of soils of different origins and characteristics. Can. Geotech. J. 46(9), 1011–1023.

[11] Coussot, P., Piau, J.-M. 1995. A large-scale field coaxial cylinder rheometer for the study of the rheology of natural coarse suspensions. Journal of rheology, 39(1), 105. doi:10.1122/1.550693.

[12] Ilstad, T., Elverhøi, A., Issler, D., Marr, J.G. 2004. Subaqueous debris flow behaviour and its dependence on the sand/clay ratio: a laboratory study using particle tracking. Marine geology, 213(1-4), 415–438. doi:10.1016/j.margeo.2004.10.017.

[13] Major, J.J., Pierson, T.C. 1992. Debris flow rheology: Experimental analysis of fine-grained slurries. Water resources research, 28(3), 841–857. doi:10.1029/91WR02834.

[14] Malet, J.-P., Laigle, D., Remaître, A., Maquaire, O. 2005. Triggering conditions and mobility of debris flows associated to complex earthflows. Geomorphology, 66(1-4), 215–235. doi:10.1016/j.geomorph.2004.09.014.

[15] Parsons, J.D., Whipple, K.X., Simoni, A. 2001. Experimental Study of the Grain-Flow, Fluid-Mud Transition in Debris Flows. The journal of geology, 109(4), 427–447. doi:10.1086/320798.

[16] Phillips, C.J., Davies, T.R.H. 1991. Determining rheological parameters of debris flow material. Geomorphology, 4(2), 101–110. doi:10.1016/0169-555X(91)90022-3.

[17] Schatzmann, M., Fischer, P., Bezzola, G.R. 2003. Rheological Behavior of Fine and Large Particle Suspensions. Journal of hydraulic engineering, 129(10), 796–803. doi:10.1061/(ASCE)0733-9429(2003)129:10(796).

[18] Whipple, K.X., Dunne, T. 1992. The influence of debris-flow rheology on fan morphology, Owens Valley, California. Geological society of america bulletin, 104(7), 887–900. doi:10.1130/0016-7606(1992)104<0887:TIODFR>2.3.CO;2.

[19] Yang, H., Wei, F., Hu, K., Zhou, G., Lyu, J. 2015. Comparison of rheometric devices for measuring the rheological parameters of debris flow slurry. J. Mt. Sci. 12(5), 1125–1134.

[20] Covelli, S., Piani, R., Acquavita, A., Predonzani, S., Faganeli, J. 2007. Transport and dispersion of particulate Hg associated with a river plume in coastal Northern Adriatic environments. Mar. Pollut. Bull. 55(10–12), 436–450.

[21] Covelli, S., Faganeli, J., Horvat, M., Brambati, A. 2001. Mercury contamination of coastal sediments as the result of long-term cinnabar mining activity (Gulf of Trieste, northern Adriatic sea). Appl. Geochem. 16(5), 541–558.

[22] Faganeli, J., Horvat, M., Covelli, S., Fajon, V., Logar, M., Lipej, L., Cermelj, B. 2003. Mercury and methylmercury in the Gulf of Trieste (northern Adriatic Sea). Sci. Total Environ. 304(1–3), 315–326.

[23] Ogrinc, N., Monperrus, M., Kotnik, J., Fajon, V., Vidimova, K., Amouroux, D., Kocman, D., Tessier, E., Žižek, S., Horvat, M. 2007. Distribution of mercury and methylmercury in deep-sea surficial sediments of the Mediterranean Sea. Mar. Chem. 107(1), 31–48.

[24] Žagar, D., Petkovšek, G., Rajar, R., Sirnik, N., Horvat, M., Voudouri, A., Kallos, G., Četina, M. 2007. Modelling of mercury transport and transformations in the water compartment of the Mediterranean Sea. Mar. Chem. 107(1), 64–88.

[25] Žagar, D., Knap, A., Warwick, J.J., Rajar, R., Horvat, M., Četina, M. 2006. Modelling of mercury transport and transformation processes in the Idrijca and Soča river system. Sci. Total Environ. 368(1), 149–163.

[26] Schramm, G. 2000. A Practical Approach to Rheology and Rheometry, 2nd Edition. Gebrueder HAAKE GmbH, Karlsruhe, Germany.

[27] Locat, J., Demers,D. 1988. Viscosity, yield stress, remolded strength, and liquidity index relationships for sensitive clays. Can. Geotech. J. 25(4), 799–806.

[28] Feys, D., Wallevik, D.E., Yahia, A., Khayat, K.H., Wallevik, O.H. 2013. Extension of the Reiner–Riwlin equation to determine modified Bingham parameters measured in coaxial cylinders rheometers. Mater. Struct. 46(1–2), 289–311.

[29] Malvern, L.E. 1969. Introduction to the mechanics of a continuous medium. Prentice-Hall.

[30] Mladenovič, A., Pogačnik, Ž., Milačič, R., Petkovšek, A., Cepak, F. 2013. Dredged mud from

the Port of Koper - Civil engineering applications. Materials and technology. 47(3), 353–356.
[31] Yan, W.M., Chang, J. 2015. Effect of pore water salinity on the coefficient of earth pressure at rest and friction angle of three selected fine-grained materials. Eng. Geol. 193, 153–157.
[32] Yukselen-Aksoy, Y., Kaya, A., Ören, A.H. 2008. Seawater effect on consistency limits and compressibility characteristics of clays. Eng. Geol. 102(1–2), 54–61.
[33] SIST. Geotechnical investigation and testing - Laboratory testing of soil - Part 1: Determination of water content. SIST-TS CEN ISO/TS 17892-1:2004.
[34] SIST. Geotechnical investigation and testing - Laboratory testing of soil - Part 12: Determination of Atterberg limits. SIST-TS CEN ISO/TS 17892-12:2004.
[35] DIN. Soil, testing procedures and testing equipment - Determination of water absorption. DIN 18132:2012-04.
[36] Brookfield Engineering Labs., Inc. 2014. More Solutions to Sticky Problems.
[37] Locat, J. 1997. Normalized rheological behaviour of fine muds and their flow properties in a pseudo-plastic regime. Proc. 1st Int. Conf. on Debris-Flow Hazards Mitigation: Mechanics, Prediction, and Assessment, San Francisco, California, United States, pp. 260–269.

DOLOČITEV DINAMIČNIH ZEMELJSKIH TLAKOV DELUJOČIH NA TOGE PREPUSTE: PREIZKUSI NA POTRESNIH MIZAH

Deniz Ulgen *(vodilni avtor)*
Mugla Sitki Koçman University,
Faculty of Engineering, Department of Civil Engineering
48100 Mugla, Turčija
E-pošta: denizulgen@mu.edu.tr

Mehmet Yener Ozkan
Middle East Technical University,
Faculty of Engineering, Department of Civil Engineering
06800 Ankara, Turčija
E-pošta: myozkan@metu.edu.tr

Ključne besede

škatlasti prepust, dinamični zemeljski pritisk, potresna miza, dinamična interakcija tla-konstrukcija, laminarna škatla, dinamični bočni koeficient

Izvleček

Potresna varnost podzemnih objektov (prepusti, podzemne železnice, sistemi za oskrbo z zemeljskim plinom in vodo), igra pomembno vlogo v trajnostni javni varnosti in urbanem razvoju. Ne poznamo splošno sprejetega postopka za oceno dinamičnih pritiskov, ki delujejo na podzemne objekte. Prav tako je na voljo zelo malo eksperimentalnih podatkov za oceno dinamičnih pritiskov. S študijo želimo izboljšati razumevanje dinamičnega obnašanja škatlastih prepustov in pritiskov, ki delujejo pri dinamičnih vzbujanjih s pomočjo eksperimentalnih analiz. V ta namen smo izvedli niz preizkusov na potresni-mizi na škatlastih prepustih zakopanih v suhem pesku. Za simulacijo robnih pogojev prostega polja, smo za uporabo v 1 g potresni mizi zasnovali in izdelali laminarno škatlo. Na dveh modelih prepustov, ki imata različne togosti smo v raznih harmoničnih gibanjih preučili vpliv razmerja prožnosti na vrednosti dinamičnih bočnih pritiskov tal. Na podlagi rezultatov preskusov predlagamo poenostavljeno porazdelitev dinamični pritiskov, ki delujejo na stranske stene modela prepusta. Za predlagano vrhnjo vrednost tlaka v porazdelitvi tlakov smo definirali dinamični bočni koeficient. Vrednosti tega koeficienta so funkcija strižnih specifičnih deformacij z upoštevanjem relativne togosti med tlemi in podzemno konstrukcijo.

EVALUATION OF DYNAMIC SOIL PRESSURES ACTING ON RIGID CULVERTS: SHAKING-TABLE TESTS

Deniz Ulgen *(corresponding author)*
Mugla Sitki Koçman University,
Faculty of Engineering, Department of Civil Engineering
48100 Mugla, Turkey
E-mail: denizulgen@mu.edu.tr

Mehmet Yener Ozkan
Middle East Technical University,
Faculty of Engineering, Department of Civil Engineering
06800 Ankara, Turkey
E-mail: myozkan@metu.edu.tr

Keywords

box culvert, dynamic earth pressure, shaking table, dynamic soil-structure interaction, laminar box, dynamic lateral coefficient

Abstract

The seismic safety of underground structures (culvert, subway, natural-gas and water-sewage systems) plays a major role in sustainable public safety and urban development. Very few experimental data are currently available and there is no generally accepted procedure to estimate the dynamic pressures acting on these underground structures. This study aims to enhance the state of the prevalent information necessary to understand the dynamic behaviour of box culverts and the stresses acting under dynamic excitations through experimental analyses. For this purpose, a series of shaking-table tests were conducted on box-type culverts buried in dry sand. To simulate the free-field boundary conditions, a laminar box was designed and manufactured for use with a 1-g shake table. Two culvert models having different rigidities were tested under various harmonic motions in order to examine the effect of the flexibility ratio on dynamic lateral soil pressures. Based on the test results, a simplified dynamic pressure distribution acting on the sidewalls of the culvert model was suggested. Then, a dynamic lateral coefficient was defined for the proposed peak pressure value in the distribution. The values of this coefficient were obtained as a function of the shear strain by considering the relative stiffness between the soil and the underground structure.

1 INTRODUCTION

The seismic design and safety of buried structures including pipelines, culverts, subways and tunnels are crucial requirements for economic and infrastructure development. The seismic assessment of underground structures gained more importance after the heavy damage from large earthquakes such as 1995 Kobe, Japan; 1999 Kocaeli, Turkey; and 1999 Chi Chi, Taiwan. The 1995 Hyogo-ken Nanbu (Kobe) Earthquake of magnitude M_w=6.9 occurred in the northern part of Awaji island near Kobe, Japan. It was one of the most destructive earthquakes and caused significant damage to Kobe's underground rapid transit system [1]. The extensive damage occurred in the Daikai Subway station built using the cut-and-cover technique. It was mentioned that the collapse of the subway and the intense damage were caused by the earthquake forces. Iida et al. [2] presented their observations from Daikai Station after the Kobe earthquake and explained the damage and failure mechanism in the subway tunnel. It was observed that shear cracks occurred on the walls of the station during the earthquake. The authors pointed out that the relative movement between the station and the overburden soil could be the main reason for the collapse. Parra-Montesinos et al. [3] evaluated the

collapse of the Daikai Subway Station and focused on the soil–structure interactions. It was emphasized that the friction between the structure and soil, the soil degradation and the relative movement between the soil and the structure should be taken into account in the design of underground structures against earthquakes. Wang et al. [4], Shimizu et al. [5], Wang and Zhang [6] and Shen et al. [7] assessed the damage mechanism of mountain tunnels under earthquake loading. It was observed that tunnels buried at shallow depths or near the surface experienced significant damage as compared to the deeply embedded tunnels. Furthermore, it was concluded that the tunnels should be constructed far away from the surface slopes and active faults. Hashash et al. [8] reviewed the several reported case histories of underground structures prepared by Duke and Leeds [9], Stevens [10], Dowding and Rozen [11], Owen and Scholl [12], Sharma and Judd [13], Power et al. [14], Kaneshiro et al. [15], In these case histories, the San Francisco Bay area rapid transit system, the Alameda tubes in California, the Los Angeles metro, the underground structures in Kobe, Japan, the underground structures in Taiwan, and the Bolu tunnel were investigated.

Ground shaking is produced by seismic waves including body waves and surface waves. Body waves are categorized as compressional and shear waves. Shear waves are the most destructive form of body waves that cause ovaling or racking deformation of underground structures [16, 8]. Within the scope of this study, the dynamic response of the underground structures was examined by producing vertically propagating shear waves.

Seismic deformations may be underestimated or overestimated depending on the relative stiffness between the buried structure and the surrounding ground [16]. In order to take into account the soil–structure interaction effect, simplified frame analysis (SFA) methods are proposed by Wang [16], Penzien [17], Huo et al. [18] and Bobet et al. [19]. Another approach to evaluating the seismic design of underground structures is the force-based method. In this method, equivalent seismic forces caused by the inertial force of the soil under earthquake loading are estimated. There is no generally accepted approach to predicting the dynamic soil pressures exerted on a culvert. One widely preferred approach to predicting the dynamic earth pressures acting on the embedded structures is the Mononobe-Okabe method [20,21]. It is not reasonable to use the Mononobe-Okabe method for rectangular buried structures since a yielding active wedge does not usually occur in the surrounding soil during an earthquake. Wang [16] stated that the Mononobe Okabe approach can be applied to structures having a U-section or buried near the soil surface. He emphasized that as the structure's embedment depth increased the theory tended to overestimate the racking deformations. Moreover, Luu [22] employed shaking-table tests and reported that the Mononobe Okabe approach gave inconsistent values for the soil's dynamic pressures.

Nishiyama et al. [23] performed shaking-table tests in order to investigate the friction between the soil and the underground structure. In the study it was pointed out that shear stresses at the ceiling and normal pressures acting on the sidewalls decrease with the decreasing friction between the ground and the embedded structure. Che and Iwatate [24] conducted shaking-table tests and numerical analyses to evaluate the dynamic lateral earth pressures and bending strains exerted on the underground structure. The authors concluded that the lateral earth pressures due to vertical motions could be ignored and rocking motions were observed during the horizontal motion. Matsui et al. [25] investigated the seismic performance of two span rectangular underground reinforced-concrete structures by employing large shaking-table experiments. The results of the study showed that the centre of the wall tended to deform inward owing to dynamic soil pressures. Bending cracks occurred at the top and bottom of the outer surface and uniform horizontal cracks were observed on the inner surface of the sidewall due to inward deformations. In later research, Che et al. [26] carried out shaking-table tests and observed that the absolute dynamic earth-pressure values were nearly identical to the values obtained from static analyses. Moreover, it was mentioned that the normal strain of the culvert could be ignored. Moss and Crosariol [27] studied the dynamic response of rigid underground structures buried in soft clay using shaking-table tests. The authors stated that the racking deformations were highly dependent on the input accelerations and that the racking deformations increased linearly with an increase of the accelerations. Chen et al. [28] performed shaking-table tests on a subway structure in soft soil and reported that the underground structures and soil were more sensitive to the low-frequency components of strong ground motions.

The ovaling deformation mode of underground structures was evaluated by Cilingir & Madabushi [29], Cilingir & Madabushi [30] and Lanzano et al. [31]. These studies mainly concentrated on the embedment depth, the dynamic soil pressures and the acceleration response of the soil. There are only a few researches [32-34] assessing the racking deformation and dynamic response of buried rectangular underground structures. Pitilakis et al. [33] performed centrifuge tests to examine the dynamic response of rectangular tunnels buried in soft soils. Results showed that the dynamic pressures acting at the centre of the sidewall were smaller than the pressures acting near the corners of the flexible tunnel.

There is a lack of experimental data for evaluating the dynamic response of rectangular underground structures. Thus, more research is required in order to clarify the seismic effects on a buried structure. In this study, 1-g shaking-table tests were performed to investigate the dynamic earth pressures acting on the box-type underground culvert. The effect of the relative stiffness between the buried culvert and the surrounding ground was evaluated under harmonic motions. Moreover, the influence of acceleration on the dynamic behaviour of the underground box-type culvert was examined. The tests provided a better understanding of the qualitative behaviour of box-type embedded structures subjected to dynamic loading. As a consequence, the main objective of this study is to make a reasonable contribution, to help to understand the dynamic load-transfer mechanism between the soil and the box-type underground culverts.

2 SHAKING-TABLE TEST SYSTEM

Shaking-table tests were carried out in the dynamic laboratory of the Civil Engineering Department of Middle East Technical University. The shaking-table system was mounted on the main steel frame having plan dimensions of 3.5 m × 1 m. The main frame was connected to a reinforced concrete foundation by welding the anchor plates. The whole system was designed and constructed by Calisan [35]. There were three main parts of the shaking-table system, i.e., the motion-generating system (actuators), the model container and the data-acquisition system. In the present study, the system was modified by using a motor driver and a laminar box. A motor driver was added to the motion-generating system to adjust the frequencies and to obtain a soft start during the shaking. Furthermore, a laminar box was designed and fabricated in the Ostim Organized Industry. The maximum displacement limit of the motion-generating system is 6 mm and the frequency range is 0.5–10 Hz. The peak accelerations used in the tests vary from 0 to 0.5 g.

2.1 Design of the Soil container

A rigid container does not conform to the soil deformation pattern and generate P-waves during shaking. Therefore, the available rigid system was renovated by using a laminar box instead of a rigid box so as to eliminate the boundary effects (Prasad et al. [36], Turan et al. [37], Hokmabadi [38]) in the current study. A rectangular laminar container was preferred rather than a ring-type container considering the plain-strain conditions for a box-type underground structure. A typical laminar box is constructed of several horizontal rectangular metal frames stacked together. The frames are free to move on linear roller bearings in the direction of motion. Thus, the box is able to conform to the soil-deformation pattern during shaking. The stiffness resisting the movement of the soil is the friction between the layers and the linear roller bearings. For this reason, the main purpose in the design of the laminar box is to minimize the friction as much as possible. Within the scope of this study, a laminar box (Fig. 1a) was designed and manufactured in the Ostim Organized Industry. It is rectangular in cross-section with dimensions of 1 m (width) × 1.5 m (length) × 1 m (height). The box is composed of nine rectangular steel frames. Each frame is 10-cm deep and the spacing between the frames is 1 cm. There are linear bearings connected to the outside rigid supporting frame on the long side (Fig. 1b). The linear bearings are fixed in a transverse direction, while they are free to move in the longitudinal direction. The short sides of the laminar frames (Fig. 1c) are connected to the long sides by means of hinge joints allowing rotation in

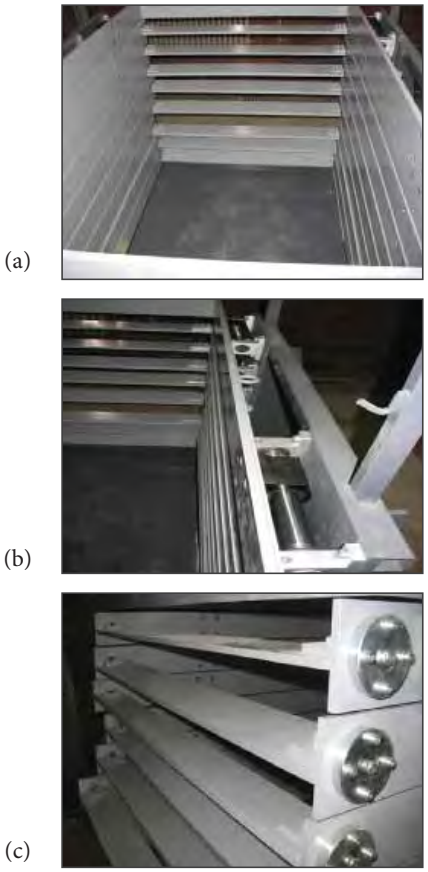

Figure 1. General view of the laminar box (b) Linear bearing connected to outside rigid supporting frame (c) Short side of the laminar box.

a transverse direction. Hence, the sidewalls of the box conform to soil-deformation and the boundary effects are minimized. The shaking table carries the ground model that was covered with a membrane to prevent soil leakage from the spacings between the laminar layers. There is no contact between the shaking table and the soil container. The shaking table vibrates the ground model and the laminar box conforms to the deformation scheme of the ground model.

2.2 Soil properties

Air dried Çine sand was used to construct the model ground in the shaking-table tests. Based on the Unified Soil Classification System (USCS), the soil can be identified as SP: poorly graded, slightly silty, medium sand. The grain size distribution curve of the sand was determined through a dry-sieve analysis. The parameters derived from distribution curve are as follows: Table 1 shows the physical properties of Çine sand.

Table 1. Physical properties of Çine sand used in shaking table tests.

Specific gravity	2.66	Coefficient of uniformity (C_u)	3.53
Minimum void ratio	0.44	Coefficient of curvature (C_c)	0.92
Maximum void ratio	0.80	Mean diameter (D_{50}) (mm)	0.45
Minimum unit weight (kN/m^3)	14.50	Fines content (%)	1.15
Maximum unit weight (kN/m^3)	18.10	Poisson's Ratio	0.3

Direct shear and triaxial tests were conducted to find the shear-strength parameters of the soil. The normal stress range in the direct shear and triaxial tests changes between 14 kPa and 50 kPa. A disturbed test sample was taken from the dry Çine sand and placed into triaxial test apparatus at a relative density of 60%. Çine sand has a friction angle of 42° at that relative density.

Initially, the maximum shear modulus was estimated as 20000 kPa using Eq.1, proposed by Hardin and Drnevich [39]. Next, the model ground was modelled in the one-dimensional ground-response analyses program SHAKE91 and the results were calibrated with the obtained free-field shear strains at the mid-depth of the culvert in shaking-table tests. Fig. 2 shows the shear modulus reduction (G/G_{max}) obtained from back-analyses of the free-field shaking-table results using SHAKE91. The shear-modulus degradation curve proposed by Darendeli [40] is given in the same figure for reference. The curve was plotted for a mean effective stress (3.6 kPa) representing the stress levels of the culvert depths in the shaking-table tests. G_{max} is the initial (low-strain) shear modulus and G is the shear modulus at any strain level. After the calibration, for a relative density of 60%, the maximum shear modulus of the ground surrounding the culvert was predicted to be 13,000 kPa.

$$G_{max} = 3230 \cdot \frac{(2.973 - e)^2}{(1+e)} \cdot OCR^k \cdot (\sigma'_m)^{1/2} \qquad (1)$$

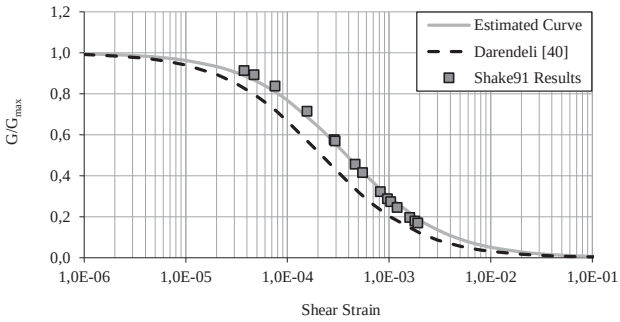

Figure 2. Variation of normalized shear modulus with respect to shear strain.

2.3 Preparation of model ground

The raining method [41] was used to prepare the model ground throughout the shaking-table tests. In order to obtain a homogeneous model ground and a uniform density throughout the laminar box, sand was pluviated into the laminar box from a height of 60cm using a sieve. The sieve is rectangular in cross-section with dimensions of 0.98 m (width) × 1.48 m (length) and a mesh size of 2.36 mm. When constructing the model ground, first, a sand bed with a thickness of 20 cm was placed into the box in two layers and compacted with a vibration tamper in order to represent a bearing stratum. Later, the remaining part of the sand was placed into the laminar box in layers of 10-cm thickness by pluviation to simulate a cut-and-cover tunnel model. During the sand raining, five small boxes were buried in the soil at different locations to determine the relative density of the sand. Measurements with small boxes showed that a uniform density and homogeneous ground model can be obtained by sand pluviation. The relative densities of the sand bed and the overlying sand changed by 80–85% and 60–65%, respectively.

2.4 Box-type culvert models

Two different types of box culvert models were used in the shaking-table tests. The box models were made of steel, which was selected as a suitable material for the culvert model among multiple alternatives such as aluminium, wood and concrete. Thus, the culvert model can be easily processed and thinner rigid walls can be obtained. Each model is 20 cm × 20 cm in cross-section and the side walls of the box structure models have two kinds of thickness, i.e., 5 mm and 10 mm. The culvert was placed into the laminar box in the transverse direction. The length of the culvert model is 80 cm. Hence, there is a friction between the culvert and the soil particles. The extremities of the culvert were lubricated to decrease the friction. The culverts were labelled as *C1* and *C2*, respectively. The upper and lower slabs of the culvert models were relatively thick and rigid, compared to sidewalls. Thus, dynamic lateral earth pressures can be monitored by eliminating the structural effects due to the bending of the slabs. Cross-sections of the box models are illustrated in Fig. 3.

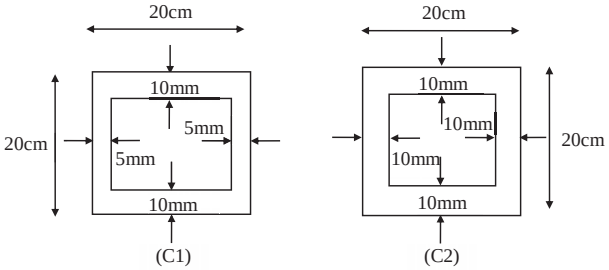

Figure 3. Cross-sections of the steel culvert models used in the shaking-table tests.

The box models were manufactured by considering the flexibility ratio, which represents the relative stiffness between the soil and the structure. The flexibility ratio of a single barrel box can be directly calculated by using the equation proposed by Wang [16]. The equation (Eq. 2) is given by:

$$F = \frac{G_s}{24}\left(\frac{H^2 W}{EI_W} + \frac{HW^2}{EI_R}\right) \qquad (2)$$

where G_s is the shear modulus of the soil, H is the height and W is the width of the box structure, I_w is the moment of inertia of the walls, and I_R is the moment of inertia of the slabs. The physical meaning of the F (flexibility ratio) values can be described as follows: for F>1, the structure is more flexible than the soil and for F<1 the structure is more rigid than the soil.

The configuration of the structure model and the layout of the transducers are depicted in Fig. 4. The box culvert model was buried in sand at a depth of 40 cm. In order to minimize the boundary effects caused by the laminar

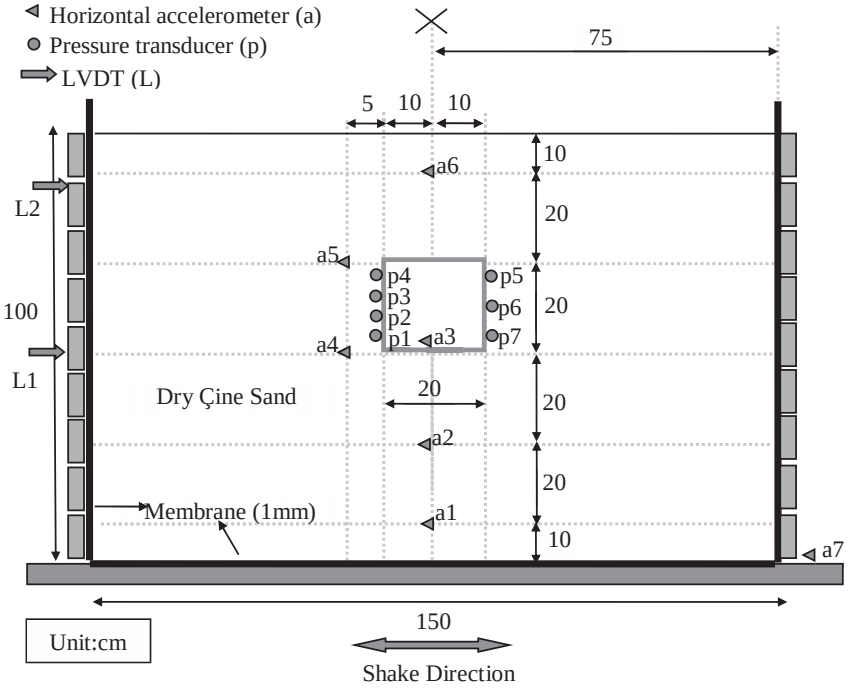

Figure 4. Layout of the culvert model and the numbering of the transducers.

box, the model and transducers were placed in the middle of the container. Seven pressure transducers were mounted on the box model to measure the dynamic soil pressures. Five accelerometers were buried in the ground model to determine the soil accelerations and deformations, and one accelerometer was placed on the shaking table to measure the input motion. Two displacement transducers (LVDT) were connected to a rigid, stable, outside frame at heights of 50 cm and 90 cm. The technical parameters of the transducers are given Table 2.

Table 2. Main technical parameters of the transducers.

Transducer	Acceleration	Pressure	Pressure	Displacement
Type	ARF-10A	KDF-200KPA	Honeywell AB/HP	SDP-100C
Capacity	10m/s^2	200kPa	42kPa	100mm
Rated output	0.5mv/v	0.3mv/v	1mv/v	2.5mV/V
Nonlinearity	1%	1%	0.5%	0.2%
Operating temperature	-10° C to 50° C	-20° C to 60° C	-54° C to 93° C	0° C to 60° C
Allowable excitation voltage	5V	10V	5V	5V
Weight	13g	160g	57g	350g

3 TESTING PROGRAM AND PROCEDURE FOR SHAKING-TABLE TESTS

There were a total of 33 shaking-table tests performed under different harmonic motions having various acceleration amplitudes and frequencies. The model ground was constructed for each test, hence, the input motions were applied separately for each test. Thus, the initial physical state is almost the same for each test. The testing program included different cases given as follows:

- Free-field response tests
- Model tests for two different culvert models (*C1*, *C2*), when the model was buried at a depth of 40 cm.

The testing program applied for all the culvert models can be tabulated as shown in Table 3.

4. RESULTS AND DISCUSSION

4.1 Boundary effect of laminar box

The boundary effect of the laminar container on the ground motion was investigated by using accelerometers. One accelerometer (a6) was placed near the sidewall at a distance of 5 cm from the membrane and the other accelerometer (a3) was placed in the middle of the laminar container. Both accelerometers were at the same level, at the mid-height of the laminar box. The acceleration time histories at those locations were recorded during the shaking-table tests. The results indicate that the acceleration record near the sidewall is very similar to the acceleration record in the middle of the container. There was almost no phase difference between the acceleration time histories; only the amplitudes changed. The ratio of the acceleration amplitude near the sidewall to the acceleration amplitude at the centre, ar, was plotted against the input acceleration in Fig. 5. As seen in Fig. 5,

Table 3. Testing program applied in shaking table experiments.

Free Field			Culvert Model 1 (*C1*)			Culvert Model 2 (*C2*)		
Test No	Acceleration (g)	Frequency (Hz)	Test No	Acceleration (g)	Frequency (Hz)	Test No	Acceleration (g)	Frequency (Hz)
1	0.05	2.0	12	0.05	2.0	23	0.05	2.0
2	0.07	2.0	13	0.07	2.0	24	0.07	2.0
3	0.11	3.1	14	0.11	3.1	25	0.11	3.1
4	0.17	3.1	15	0.17	3.1	26	0.17	3.1
5	0.22	3.1	16	0.22	3.1	27	0.22	3.1
6	0.26	4.2	17	0.26	4.2	28	0.26	4.2
7	0.30	4.2	18	0.30	4.2	29	0.30	4.2
8	0.35	5.3	19	0.35	5.3	30	0.35	5.3
9	0.40	5.3	20	0.40	5.3	31	0.40	5.3
10	0.45	6.4	21	0.45	6.4	32	0.45	6.4
11	0.50	6.4	22	0.50	6.4	33	0.50	6.4

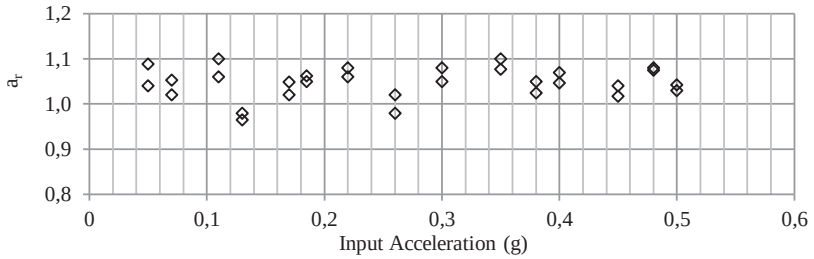

Figure 5. Variation of acceleration amplitude ratio (wall to centre), a_r, with respect to the input acceleration.

there is a minor variation of about 5% and 10% between the wall and the centre accelerations. Hence, it can be said that the walls of the laminar container do not have a significant boundary effect on the ground motion. In this study, the model was placed at the centre of the container to minimize the boundary effects.

4.2 Comparison of measured static lateral coefficients with Jaky's formula

Fig. 6 shows the variation of the lateral earth-pressure coefficients (K) with respect to the depth ratio. The depth ratio is represented by d/H, where d is the distance from the pressure transducer to the upper corner of the culvert and H is the culvert height. For comparison, two lines indicating the at-rest and the active earth-pressure coefficients, K_o and K_a, were drawn in the same plot. K_o was calculated from the following empirical relationship (Eq. 3) proposed by Jaky [42]:

$$K_o = 1 - \sin\phi' \qquad (3)$$

where ϕ' is the drained friction angle. K_a was determined using Eq. 4, suggested by Rankine [43]. For an internal friction angle of 42°, K_o and K_a were calculated as 0.33 and 0.2, respectively.

$$K_a = \frac{1 - \sin\phi'}{1 + \sin\phi'} \qquad (4)$$

As seen from Fig. 6, all the measured earth-pressure coefficient values are above the K_a line. The K values obtained for the culvert models *C1* and *C2* are in close agreement with the K_o line. The results showed that the lateral earth-pressure coefficient decreased with an increasing flexibility ratio, as expected. The sidewall of the flexible culverts deforms more than that of the rigid culverts and accordingly the walls are subjected to a low soil pressure.

4.3 Maximum acceleration along the depth of the ground model

In order to investigate the variation of the maximum acceleration along the depth of the soil model, the accelerometers were placed at 5 different depths in the soil, as shown in Fig. 7. The recorded maximum accelerations at those depths normalized with the maximum shaking acceleration and plotted versus the soil depth as given in Fig. 8a and Fig. 8b. As seen in Fig. 8a, the normalized acceleration (amplification ratio) is very low and changes around 1 for the maximum input accelerations 0.05 g, 0.07 g, and 0.11 g. This means that the soil behaves as a

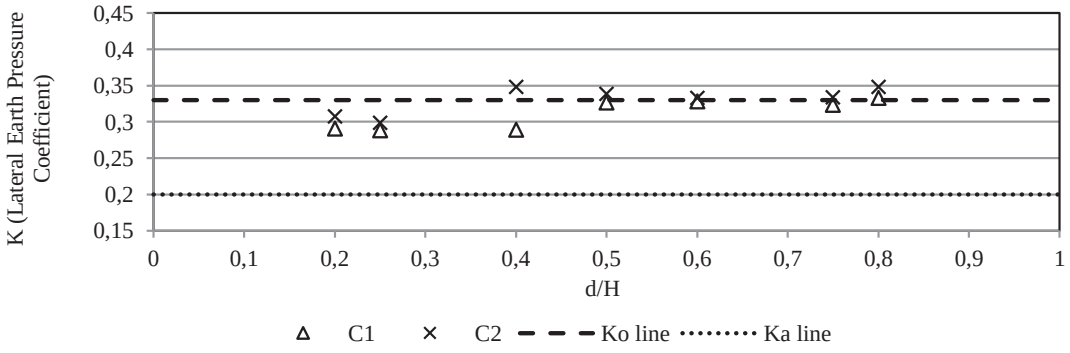

Figure 6. Variation of the earth-pressure coefficient (K) with respect to the depth ratio (d/H).

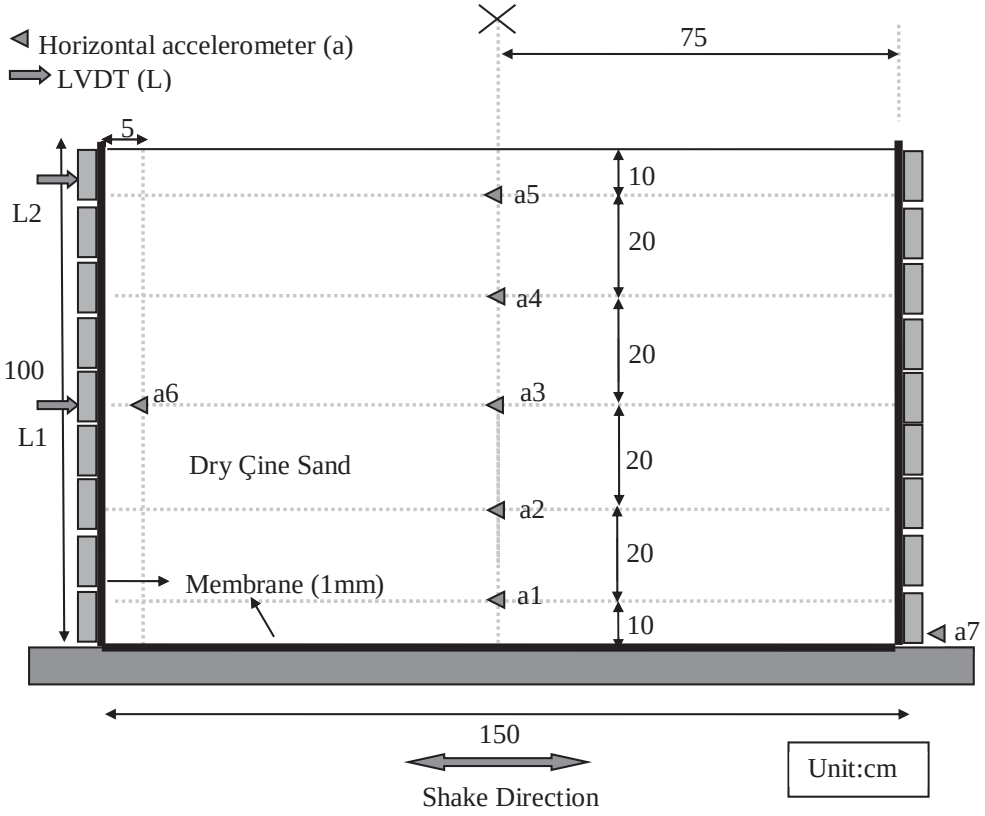

Figure 7. Layout of the transducers in free-field shaking-table tests.

rigid mass at low strain levels. The amplification ratio starts to increase at 0.17 g and at the top layer of the soil it becomes approximately 1.1 g. Fig. 8b shows the variation of the normalized acceleration along the depth of the soil model for the maximum input accelerations of 0.22 g, 0.26 g, 0.30 g, 0.34 g, 0.4 g, 0.45 g and 0.50 g. In the figure, it is observed that the amplification ratio near the surface changes between 1.2 and 1.4. Higher accelerations in the upper region of the model ground may occur due to reflection and refraction of the seismic waves from the surface.

4.4 Evaluation of displacements and shear strains

The displacement of the laminar box and the soil were measured by using linear variable transducers and accelerometers, respectively. The LVDT measures the displacements directly. In contrast to the LVDT, the accelerometer can provide an indirect measure of the displacement by integrating the acceleration time history twice. Before the integration process the data must be filtered to prevent any unwanted errors or misleading results. For this reason, the recorded acceleration time histories were filtered by a bandpass filter between 1Hz and 20Hz (high pass at 1 Hz and low pass at 20Hz). Thus, high-frequency noise and drift due to spurious low-frequency components were eliminated to enhance the data quality.

The accelerometers were placed at different heights in the soil model. As explained above, the displacements were computed by a double integration of the acceleration records. Assuming that the displacement is varying linearly between the two accelerometers located at points 1 and 2, the shear strain can be calculated using Eq. 5:

$$\gamma = \frac{d_2 - d_1}{z_2 - z_1} \qquad (5)$$

where γ is the shear strain, d_1, d_2 are the displacements at points 1, 2 and z_1, z_2 are the heights at points 1, 2, respectively. Based on this approach, the soil's shear strain around the culvert model was obtained for the input motions having different acceleration amplitudes. Two displacement transducers, $L1$ and $L2$, were placed at mid height (50 cm elevation) and near the top (90 cm elevation) of the laminar box. The displacement time histories were analysed at different acceleration levels, i.e., 0.11 g and 0.4 g. It was observed that the

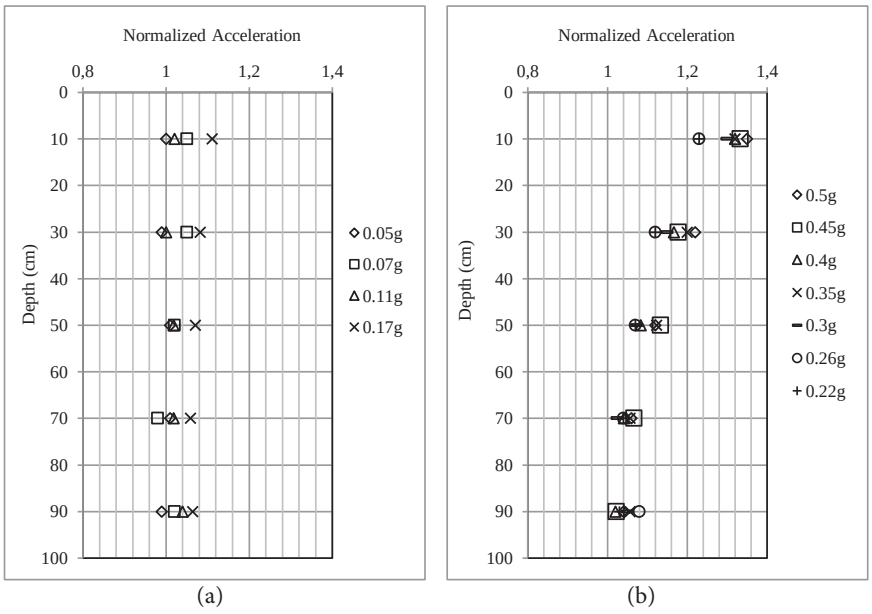

Figure 8. Variation of the maximum acceleration along the soil profile for maximum input accelerations (a) For 0.05 g, 0.07 g, 0.11 g, 0.17 g (b) For 0.22 g, 0.26 g, 0.3 g, 0.35 g, 0.4 g, 0.45 g, 0.5 g.

relative displacement between *L*1 and *L*2 increases with an increase in the acceleration, as expected. Moreover, there is a small phase shift at higher accelerations. The following figures (Fig. 9, Fig. 10) provide a comparison between the displacement time histories recorded by *L*1 and *L*2 for different accelerations.

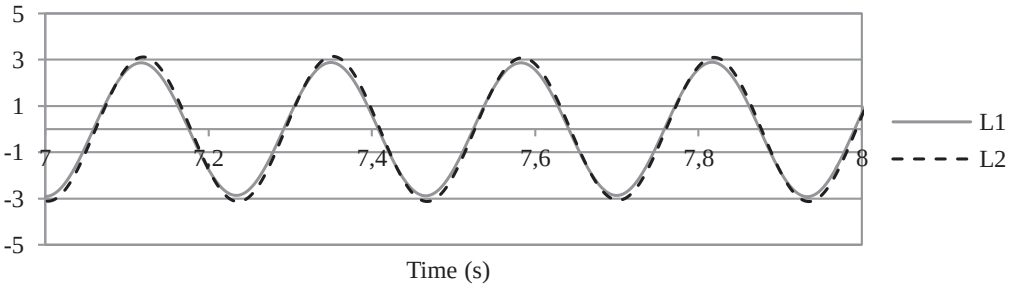

Figure 9. Displacement time histories recorded by *L*1 and *L*2 at 0.11 g maximum input acceleration.

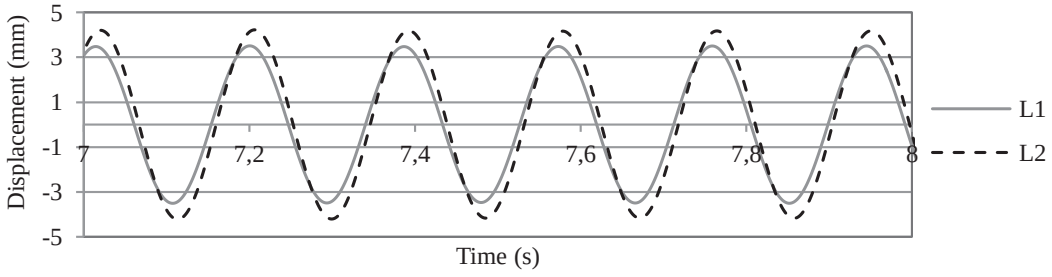

Figure 10. Displacement time histories recorded by *L*1 and *L*2 at 0.4 g maximum input acceleration.

4.5 Determination of the flexibility ratio for the culvert models

The flexibility ratio (relative stiffness) is defined as the ratio of the soil stiffness to the structural stiffness. It has a significant role on the dynamic response of the underground culverts; hence special attention should be given to the determination of the flexibility ratio. In dynamic soil culvert interaction analyses the relative stiffness is represented by the ratio of the shear modulus of the surrounding ground to the structural racking (flexural) stiffness. The main difficulty in determining the flexibility ratio is the assessment of shear modulus, which is strongly dependent on the intensity of the dynamic motion. It decreases with the increasing shear strain of the soil. Therefore, different flexibility ratios can be obtained under different dynamic motions for the same culvert. Based on this conclusion, the flexibility ratios of the two culvert models were determined at different strain levels. The three-step procedure for calculating the flexibility ratios is as follows:

1) The shear strain at the mid-depth of the culvert model was computed from the accelerometer records of a4 and a5 using Eq. 5.
2) The degraded shear modulus at the calculated shear strain in step 1 was obtained using Fig. 2.
3) The calculated shear modulus in step 2 was substituted into Eq. 2 to obtain the flexibility ratio.

Table 4 presents the flexibility ratio values for both of the culvert models at different input accelerations.

4.6 Dynamic soil pressures acting on the sidewalls of the culverts

In the shaking-table tests the lateral soil pressures were measured at each sidewall of the culvert models. During the tests the static and dynamic pressures were measured separately. For this purpose, first, the static pressure was recorded, then the dynamic pressures were measured by taking the initial values as static pressures. There are four pressure transducers on the left-hand side and three pressure transducers on the right-hand side of the culvert model. Fig. 11 and Fig. 12 show the variation of the recorded maximum dynamic pressures at those sensors with respect to the free field shear strain (at the mid-depth of the culvert) for the two culvert models used in the shaking-table tests.

The maximum pressures at each cell were measured at different times during the excitation. In other words, they do not act on the sidewalls of the culvert, simultaneously. As seen from the figures the maximum dynamic pressure increases with an increase of the shear strain and the rigidity of the structure, as expected. Moreover, it was observed that the maximum dynamic pressures occur near the corners of the culvert model. Dynamic lateral soil pressures acting on the sidewalls of

Table 4. Flexibility ratio values for the culvert models at different input accelerations.

Maximum Input Acceleration (g)	0	0.05	0.07	0.11	0.17	0.22	0.26	0.30	0.35	0.40	0.45	0.50
Flexibility Ratio for *C1*	2.3	2.25	2.18	2.06	1.71	1.05	1.03	0.98	0.91	0.80	0.80	0.63
Flexibility Ratio for *C2*	0.52	0.50	0.49	0.48	0.45	0.43	0.41	0.34	0.31	0.23	0.23	0.19

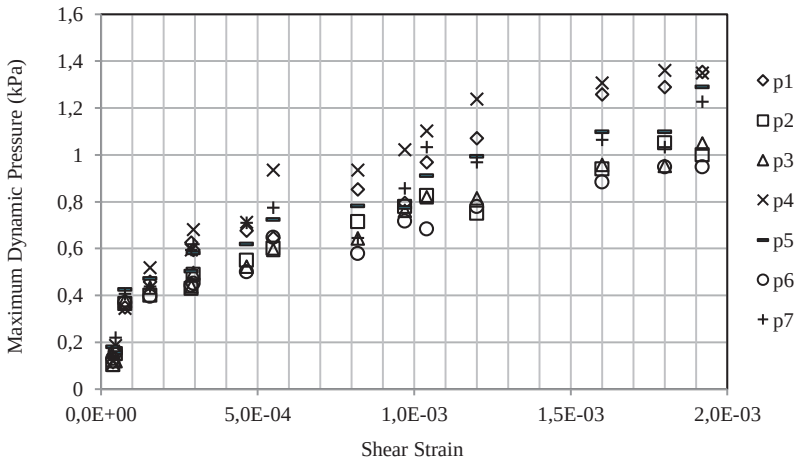

Figure 11. Variation of maximum dynamic pressure with field shear strain at the culvert mid-depth for model *C1*.

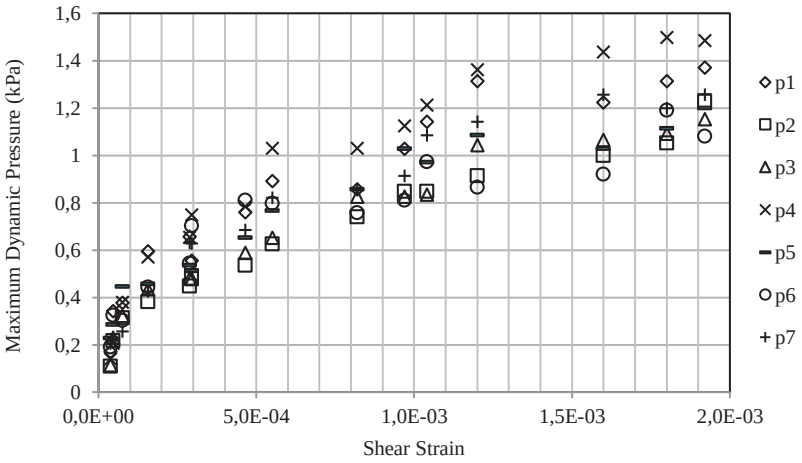

Figure 12. Variation of maximum dynamic pressure with field shear strain at the culvert mid-depth for model *C2*.

the culvert model are not constant and change during the excitation. This results in a rapidly varying pressure distribution along the sidewall of the culvert model. In order to evaluate the critical dynamic pressure distribution acting on the culvert model, the maximum bending moment at the lower slab of the culvert was calculated by considering the racking as the most critical deformation mode. Based on this analysis, the pressure distributions giving the maximum bending moments were determined. In the obtained pressure distribution there is an opposite phase angle between the recorded pressure values at same levels of the left- and right-hand sides of the culvert models, as found in the studies of Che et al. [44] and Nishiyama et al. [23]. When the upper-left corner, *UL*, of the box model is in compression, the upper-right, *UR*, corner is in tension. In contrast, when the lower-left, *LL*, corner is in tension, the lower-right corner, *LR*, is in compression, as illustrated in Fig. 13. This result can be interpreted by the cross-coupling forces that compel the culvert model to make racking deformation. Besides, it should again be noted that the "tension" forces do not represent the negative or suction

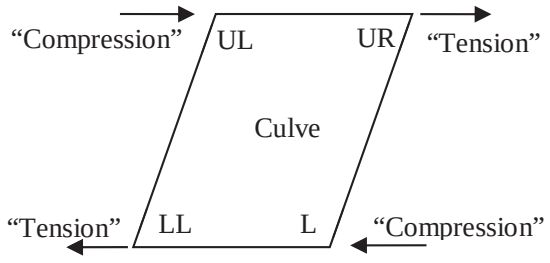

Figure 13. Schematic illustration of dynamic couple forces acting on the culvert box.

forces. It is an indication of the reduction in the static soil pressures acting on the sidewalls of the culvert.

4.7 Simplified pressure distribution

For the preliminary assessment of box-type culverts buried in dry sand, the most critical pressure distributions obtained from the shaking-table measurements were simplified, as given in Fig. 14. The peak value of the triangular dynamic pressure distribution is denoted as P_d. The P_d value was taken as the maximum pressure value measured at the upper corner of the culvert in the shaking-table tests. It was normalized with the geostatic vertical stress, $\sigma_{v,mid}$, at the mid-depth of the culvert (Eq. 6). The resulting factor was defined as the dynamic lateral pressure coefficient, k_d

$$k_d = \frac{P_d}{\sigma_{v,mid}} \qquad (6)$$

Fig. 14 shows the variation of k_d with respect to the free-field shear strain (at the mid-depth of the structure) and the maximum input acceleration for the two culvert models. The flexibility ratio of a culvert varies with the intensity of the dynamic motion. It is strongly dependent on the degraded soil shear modulus and, accordingly, on the shear strain. For this reason, the culvert models are represented by initial flexibility ratio, *IFR*, values, as given in Fig. 15. The *IFR* value is defined as the ratio of the maximum soil shear modulus to the structural racking stiffness.

The variation of k_d with respect to the shear strain and the maximum input acceleration were approximated by logarithmic and linear curves, respectively. The

approximated equations (Eq. 7 and Eq. 8) of the curves for different *IFR* values are given as follows:

For *IFR*=2.3:

$$k_d = 0.0479 \cdot \ln(\gamma_s) + 0.5005 \quad (R^2 = 0.9659) \qquad (7)$$

For *IFR*=0.52:

$$k_d = 0.0526 \cdot \ln(\gamma_s) + 0.5505 \quad (R^2 = 0.9659) \qquad (8)$$

where a_{max} is the maximum input acceleration in g and γ_s is the free-field strain at the mid-depth of the culvert. The intensity of the shaking is better represented by the shear strain than the maximum input acceleration. Hence, it is better to estimate the dynamic lateral pressure coefficient by using the k_d versus shear strain curves shown in Fig. 15 or the corresponding approximated equations given for different *IFR* values. It should be noted that the given curves are valid in the range of shear strain between 0.001% and 0.2%. Experimental validation is required for higher strains.

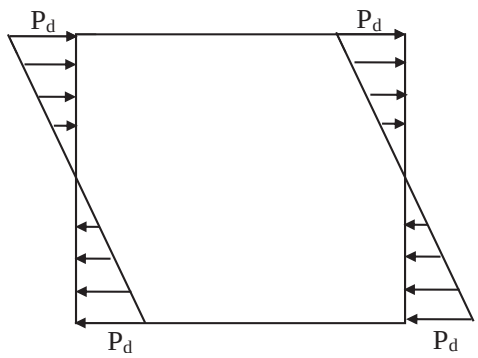

Figure 14. Simplified dynamic pressure distribution acting on the sidewalls of the culvert.

5. SUMMARY AND CONCLUSIONS

The aim of this study was to investigate the dynamic response of underground culverts by considering the soil–structure interaction. To achieve this, shaking-table tests were conducted on box-type models under harmonic motions. The results of the experiments were analysed in order to make an assessment of the dynamic lateral pressures acting on the underground culverts. To minimize the boundary effects, a laminar box was designed and manufactured for the shaking-table tests. Two culvert models having different aspect ratios were buried at a certain depth in a laminar container and subjected to harmonic excitations. The top and bottom thicknesses of the box models were kept thicker than the sidewalls of the box. In order to have different relative stiffness values for the box with respect to the surrounding soil, the effect of the relative stiffness on the soil's dynamic pressures was examined without considering the bending of the slabs. Pressure transducers were mounted on the right- and left-hand sides of the culvert model to measure the dynamic earth pressures. Acceleration transducers were buried in the surrounding soil to evaluate the shear strain and the acceleration response of the soil. Based on the results of the shaking-table tests, a simplified dynamic lateral coefficient was proposed to estimate the dynamic soil-pressure distribution acting on the culvert sidewalls. The major conclusions based upon an evaluation of the data obtained from the shaking table tests are summarized below:

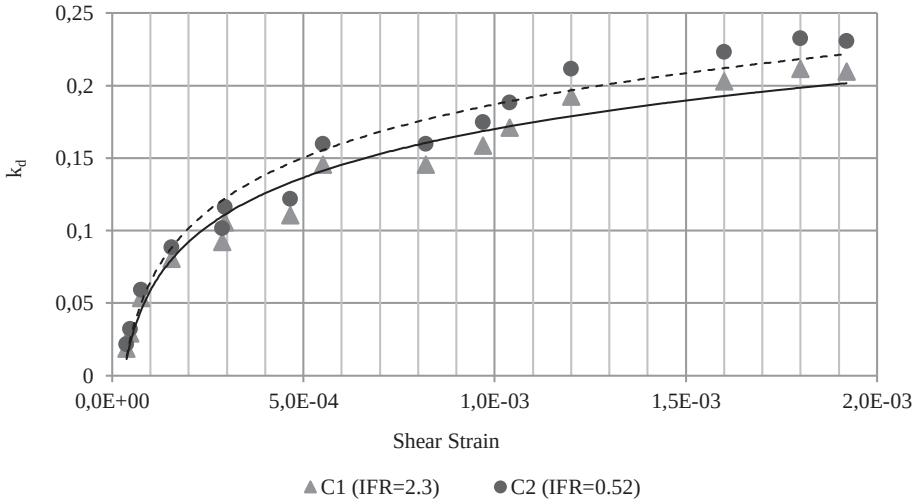

Figure 15. Variation of k_d with respect to free-field shear strain and *IFR*.

1) Static pressure values recorded at the sidewalls of the 1-g culvert models and the lateral pressure coefficient, *K*, calculated from these measurements were compared with the well-known at-rest pressure coefficient Ko and the active pressure coefficient, K_a. It was observed that the *K* values decrease with an increasing relative stiffness. The *K* values approach the K_o value obtained by Jaky's equation and they are larger than the K_a value.

2) Amplification of the acceleration depends on the shear strain level, which in turn is dependent upon the input motion acceleration amplitude and frequency. At low strains almost no amplification was observed in the model ground. At relatively higher strains and higher frequencies, the amplification values were between 1.2 and 1.4.

3) Dynamic pressure values recorded at the upper-left corner of the culvert model indicate an opposite phase with the lower-left and upper-right corners. In other words, when a pair of cross corners of the culvert is under dynamic compression the other pair is under dynamic tension. This behaviour indicates that the culvert model is compelled to make racking deformation by the cross-coupling forces.

4) Static and dynamic soil pressures acting on the sidewalls of the culvert were measured separately in the shaking-table tests. Based on the measurements, a dynamic pressure distribution along the sidewalls was approximated. The magnitude of the dynamic pressure distribution was normalized with the overburden pressure at the mid depth of the box-type culvert and accordingly a dynamic lateral pressure coefficient (k_d) was obtained. It was observed that the k_d value increases with a decreasing flexibility ratio and vice versa. Additionally, k_d increases logarithmically with an increasing shear strain.

5) The resonance frequencies of the ground model cannot be captured due to the limitations of the motion-generating system. The mean stresses are low due to the small scale of the box. Thus, the friction angle is higher and the soil exhibits more dilative behaviour. The proposed dynamic pressure distribution is given for box-type culverts buried in dry sand. It is necessary to perform further 1-g shaking-table tests or centrifuge tests to explore the effects of the structural dimensions and the type of soil. In this study, the range of shear-strain levels at the mid depth of the culvert varies between 0.001% and 0.2%. Further laboratory tests are needed to investigate the variation of the dynamic pressure at higher strain levels.

Acknowledgements

The research leading to these results has received funding from DPT with the Science Research Project (BAP) code: BAP0811DPT2002K120510COG05. Support of DPT is gratefully acknowledged.

REFERENCES

[1] Sitar, N. 1995. (editor and coauthor with 18 members of the geotechnical reconnaissance team), Geotechnical Reconnaissance of the Effects of the January 17, 1995, HyogokenNanbu Earthquake Japan. Earthquake Engineering Research Center, University of California, Report No. 9501, 143 p.

[2] Iida, H., Hiroto, T., Yoshida, N., Iwafuji, M. 1996. Damage to Daikai Subway Station, Soils and Foundations Special Issue on Geotechnical Aspects of the January 17, 1995 HyogokenNambu Earthquake. Japanese Geotechnical Society.

[3] Parra-Montesinos, G.J., Bobet, A., Ramirez, J. 2006. Evaluation of Soil-Structure Interaction and Structural Collapse in Daikai Subway Station During Kobe Earthquake. American Concrete Institute, Structural Journal 103(1), 113-122.

[4] Wang, W.L, Wang, T.T, Su J.J, Lin, C.H., Seng, C.R. Huang, T.H. 2001. Assessment of damage in mountain tunnels due to the Taiwan Chi Chi Earthquake. Tunnel Underground Space Technology 16(3), 133-150. doi:10.1016/S0886-7798(01)00047-5

[5] Shimizu, M., Suzuki, T., Kato, S., Kojima, Y., Yashiro, K., Asakura, T. 2007. Historical Damages of Tunnels in Japan and Case Studies of Damaged Railway Tunnels in the Mid Niigata Prefecture Earthquakes. ITA-AITES World Tunnel Congress 2007, Prague, Czech Rep.

[6] Wang, Z.Z., Zhang, Z. 2013. Seismic damage classification and risk assessment of mountain tunnels with a validation for the 2008 Wenchuan earthquake. Soil Dynamics and Earthquake Engineering 45, 45-55. doi:10.1016/j.soildyn.2012.11.002

[7] Shen, Y., Gao, B., Yang, X., Tao, S. 2014. Seismic damage mechanism and dynamic deformation characteristic analysis of mountain tunnel after Wenchuan earthquake. Engineering Geology 180, 85-98. doi:10.1016/j.enggeo.2014.07.017

[8] Hashash, Y. M., Hook, J. J., Schmidt, B., I-Chiang Yao, J. 2001. Seismic design and analysis of underground structures. Tunnelling and Underground Space Technology 16, 247-293. doi:10.1016/S0886-

7798(01)00051-7
[9] Duke, C.M., Leeds, D.J. 1959. Effects of Earthquakes on Tunnels, Protective Construction in a Nuclear Age. Proceedings 2nd Protective Construction Symp. March 24-26, pp. 303-328.
[10] Stevens, P.R. 1977. A review of the effects of earthquakes on underground mines. US Energy Research and Development Administration United States Geological Survey Open File, Report No. 77313, 47p.
[11] Dowding, C.H., Rozen, A. 1978. Damage to rock tunnels from earthquake shaking. J. Geotech. Eng. Div. ASCE 104(2), 175-192.
[12] Owen, G.N., Scholl, R.E. 1981. Earthquake engineering of large underground structures. Federal Highway Administration and National Science Foundation, Report no. FHWA_RD80_195.
[13] Sharma, S., Judd, W.R. 1991. Underground opening damage from earthquakes. Engineering Geology 30, 263-276. doi:10.1016/0013-7952(91)90063-Q
[14] Power, M., Rosidi, D., Kaneshiro, J. 1998. Seismic vulnerability of tunnels and underground structures revisited. Proceedings of the North American Tunneling Conference. Elsevier, Long Beach, CA, USA.
[15] Kaneshiro, J.Y., Power, M., Rosidi, D. 2000. Empirical correlations of tunnel performance during earthquakes and aseismic aspects of tunnel design. Proceedings of the Conference on Lessons Learned From Recent Earthquakes-On Earthquakes in Turkey 1999, November 8-11.
[16] Wang, J.N. 1993. Seismic Design of Tunnels: A State of the Art Approach. Monograph 7, Parsons, Brinckerhoff, Quade and Douglas Inc., New York.
[17] Penzien, J. 2000. Seismically induced racking of tunnel linings. Earthquake Engineering & Structural Dynamics 29(5), 683-691. doi:10.1002/(SICI)1096-9845(200005)29:5<683::AID-EQE932>3.0.CO;2-1
[18] Huo, H., Bobet, A., Fernandez, G., Ramirez, J. 2006. Analytical solution for deep rectangular underground structures subjected to far field shear stresses. Tunneling and Underground Space Technology 21, 613–625. doi:10.1016/j.tust.2005.12.135
[19] Bobet, A., Fernández, G., Huo, H., Ramírez, J. 2008. A practical iterative procedure to estimate seismic induced deformations of shallow rectangular structures. Canadian Geotechnical Journal 45, 923-938.
[20] Okabe, S. 1926. General theory of earth pressures, Journal of the Japan Society of Civil Engineering 12(1).
[21] Mononobe, H.A., Matsuo, H. 1929. On the determination of earth pressures during earthquakes. Proceedings of World Engineering Congress, Tokyo, Japan, pp. 177-185.
[22] Luu, A.L. 2013. Seismic earth pressures measured during a shake table experiment of underground structures. M. Sc. Thesis, University of California, Irvine.
[23] Nishiyama, S., Kawawa, I., Muroya, K., Haya, H., Nishimura, A. 2000. Experimental study of seismic behavior of box type tunnel constructed by open cutting method. Twelfth World Conference on Earthquake Engineering, January 30-February 4, Auckland, New Zealand.
[24] Che, A., Iwatate, T. 2002. Shaking table test and numerical simulation of seismic response of subway structures, Structures under shock and impact VII 367-376.
[25] Matsui, J., Ohtomo, K., Kanaya, K. 2004. Development and Validation of Nonlinear Dynamic Analysis in Seismic Performance Verification of Underground RC Structures, Journal of Advanced Concrete Technology 2(1), 25-35.
[26] Che, A., Iwatate, T., Ge, X. 2006a. Study on dynamic response of embedded long span corrugated steel culverts using scaled model shaking table tests and numerical analyses. Journal of Zhejiang University Science A 7(3), 430-435.
[27] Moss, R.E.S, Crosariol, V. A. 2013. Scale model shake table testing of an underground tunnel cross section in soft clay. Earthquake Spectra 29(4), 1413-1440. doi: http://dx.doi.org/10.1193/070611EQS162M
[28] Chen, G., Chen, S., Zuo, X., Du, X., QI, C., Wang, Z. 2014. Shaking-table tests and numerical simulations on a subway structure in soft soil. Soil Dynamics and Earthquake Engineering 76, 13-28. doi:10.1016/j.soildyn.2014.12.012.
[29] Cilingir, U., Madabhushi, S.P.G. 2011a. Effect of depth on the seismic response of circular tunnels. Canadian Geotechnical Journal 48(1), 117-127.
[30] Cilingir, U., Madabhushi, S.P.G. 2011b. A model study on the effects of input motion on the seismic behavior of tunnels. Soil Dynamics and Earthquake Engineering 31, 452-462. doi:10.1016/j.soildyn.2010.10.004
[31] Lanzano, G., Bilotta, E., Russo, G., Silvestri, F., Madabhushi, S.P.G. 2012. Centrifuge modeling of seismic loading on tunnels in sand. Geotechnical Testing Journal 35, 854-869.
[32] Cilingir, U., Madabhushi, S.P.G. 2011c. Effect of depth on the seismic response of square tunnels. Soils and Foundations 51(3), 449-457. http://doi.org/10.3208/sandf.51.449
[33] Pitilakis, K., Tsinidis, G., Anastisiadis, A., Pitilakis, D., Heron, C., Madabushi, S.P.G., Stringer,

M., Paolucci, R. 2013. Ivestigation of Several Aspects Affecting the Seismic Behaviour of Shallow Rectangular Underground Structures in Soft Soils, 2013. Series Project Web: http://www.series.upatras.gr/sites/default/files/file/SERIES_TUNNELSEIS_Final_Report.pdf

[34] Dashti, S., Hushmand, A., Ghayoomi, M., McCartney, J.S., Zhang, M., Hushmand, B., Mokarram, N., Bastani, A., Davis, C., Yangsoo, L., Hu, J. 2013. Centrifuge Modeling of Seismic Soil-Structure-Interaction and Lateral Earth Pressures for Large Near-Surface Underground Structures. Proceedings of the 18th International Conference on Soil Mechanics and Geotechnical Engineering, Paris, France.

[35] Çalısan, O. 1999. A Model Study on the Seismic Behavior of Gravity Retaining Walls. Ph.D Dissertation, Middle East Technical University, Ankara.

[36] Prasad, S.K., Towhata, I., Chandradhara, G.P., Nanjundaswamy, P. 2004. Shaking table tests in earthquake geotechnical engineering. Current Science Special section: Geotechnics and earthquake hazards 87(10), 1398-1404.

[37] Turan, A., Hinchberger, S., El Naggar, H. 2009. Design and commissioning of a laminar soil container for use on small shaking tables. Soil Dynamics and Earthquake Engineering 29(2), 404-414. doi:10.1016/j.soildyn.2008.04.003

[38] Hokmabadi, A.S. 2014. Effect of dynamic soil-pile-structure interaction on seismic response of mid-rise moment resisting frames. Ph. D. Dissertation, Faculty of Engineering and Information Technology, University of Technology Sydney, Sydney, Australia.

[39] Hardin, B.O., Drnevich, V.P. 1972. Shear modulus and damping in soils: design equation and curves. J. Soil Mech. Found. Engng. Div. 98(7), 667–692.

[40] Darendeli, M. 2011. Development of a new family of normalized modulus reduction and material damping curves. Ph.D. Thesis, Dept. of Civil Eng., Univ. of Texas, Austin.

[41] Okamoto, M., Fityus, S. 2006. An Evaluation of the Dry Pluviation Preparation Technique Applied to Silica Sand Samples. Geomechanics and Geotechnics of Particulate Media: Proceedings of the International Symposium on Geomechanics and Geotechnics of Particulate Media, London, pp. 33–34.

[42] Jaky, J. 1948. Pressure in soils, 2nd ICSMFE, London, Vol. 1, pp. 103-107.

[43] Rankine, W. 1857. On the stability of loose earth Philosophical Transactions of the Royal Society of London 147, 9-27.

[44] Che, A., Iwatate, T., Ge, X. 2006b. Evaluation of dynamic soil structure interaction and dynamic seismic soil pressures acting on it subjected to strong earthquake motions. Journal of Shangai Jiaotong University 11(4), 530-536.

VPLIV OBLIKE IN VELIKOSTI ZRN PESKOV NA HIDRAVLIČNO PREPUSTNOST

Ali Firat Cabalar *(vodilni avtor)*
University of Gaziantep,
Department of Civil Engineering
27310, Gaziantep, Turčija
E-pošta: cabalar@gantep.edu.tr

Nurullah Akbulut
Hasan Kalyoncu University,
Department of Civil Engineering
27100, Gaziantep, Turčija

Ključne besede

pesek, oblika, velikost, hidravlična prepustnost

Izvleček

Clij pričujoče študije je preiskati vpliv nekaterih fizikalnih lastnosti peskov (npr., velikost, oblika) na hidravlično prepustnost (k). Članek prikazuje rezultate obsežnih eksperimentalnih preiskav izvedenih z uporabo zrn peskov različnih velikosti in oblik. Preiskana so bila tri različna območja velikosti zrn (0.60 mm - 1.18 mm, 1.18 mm - 2.00 mm in 0.075 mm - 2.00 mm) peskov (i. drobljeni kamniti pesek, CSS; ii. pesek Trakya, TS; iii. pesek Narli, NS; iv. peleti elektrofiltrskega pepela, FAP; v. pesek Leighton Buzzard, LBS) z različnimi oblikami, vključno z okroglostjo, R, in sferičnostjo, S (R_i=0.15, S_i=0.55; R_{ii}=0.43, S_{ii}=0.67; R_{iii}=0.72, S_{iii}=0.79; R_{iv}=0.65, S_{iv}=0.89; R_v=0.78 S_v=0.65) v aparatu za določitev koeficienta prepustnosti s konstantno hidravlično višino pri relativni gostoti (D_r) okoli 35% in konstantno temperaturo prostora (20°C). Eksperimentalni rezultati so pokazali, da imajo peski z različnimi oblikami zrn (R, S) in enakih velikosti zrn ter granulometrije (c_c, c_u, D_{10}, D_{30}, D_{50}, D_{60}) različne vrednosti koeficientov hidravlične prepustnosti k. Fotografije posnete z vrstičnim elektronskim mikroskopom (Scanning Electron Microscope - SEM) kažejo fizikalne razlike / podobnosti med peski, ki so bili uporabljeni v tej preiskavi. Predstavljena je tudi primerjalna študija rezultatov preskusov in ocenjenih vrednosti hidravličnih prepustnosti z uporabo empiričnih enačb nekaterih raziskovalcev razvitih za oceno hidravlične prepustnosti tal.

EFFECTS OF THE PARTICLE SHAPE AND SIZE OF SANDS ON THE HYDRAULIC CONDUCTIVITY

Ali Firat Cabalar *(corresponding author)*
University of Gaziantep,
Department of Civil Engineering
27310, Gaziantep, Turkey
E-mail: cabalar@gantep.edu.tr

Nurullah Akbulut
Hasan Kalyoncu University,
Department of Civil Engineering
27100, Gaziantep, Turkey

Keywords

sand, shape, size, hydraulic conductivity

Abstract

This study aims to investigate the effects of some physical properties of sands (e.g., size and shape) on the hydraulic conductivity (k). The paper presents the results of an extensive series of experimental investigations performed using sands with different sizes and particle shapes. Three different particle size ranges (0.60- 1.18 mm, 1.18- 2.00 mm, and 0.075- 2.00 mm) of sands (i. Crushed Stone Sand, CSS; ii. Trakya Sand, TS; iii. Narli Sand, NS; iv. Fly Ash Pellets, FAP; v. Leighton Buzzard Sand, LBS) having distinct shapes, including roundness, R, and sphericity, S (R_i=0.15, S_i=0.55; R_{ii}=0.43, S_{ii}=0.67; R_{iii}=0.72, S_{iii}=0.79; R_{iv}=0.65, S_{iv}=0.89; R_v=0.78 S_v=0.65) were tested in a constant-head permeability testing apparatus at a relative density (D_r) of about 35% and constant room temperature (20°C). The experimental results showed that the sands having different shapes (R, S) with the same size and gradation characteristics (c_c, c_u, D_{10}, D_{30}, D_{50}, D_{60}) result in different k values. The scanning electron microscope (SEM) images indicate the physical differences/similarities among the sands used during this investigation. A comparative study of the tests results and the estimated hydraulic conductivity values using empirical equations previously developed for the hydraulic conductivity prediction of soils by certain researchers are presented.

1 INTRODUCTION

Water is free to flow through the pores between soil particles in accordance with the Darcy's empirical law (q=Aki). The hydraulic conductivity or coefficient of permeability (k) depends basically on the average size of the pores through the soil matrix and the temperature of the environment. It widely known that the hydraulic conductivity is related to the grain-size distribution of the soil grains [1]. In general, the smaller the soil grains, the lower is the coefficient of permeability. The presence of a fines content in a coarse-grained soil results in a k value significantly lower than that for the same soil without fines. The k value also changes with temperature, upon which the viscosity of the fluid (i.e., water) is dependent [2- 4]. From clay to gravels, the k value increases over many orders of magnitude. Typical k values for different soils are within the ranges shown in Table 1.

Because of its importance in some geotechnical problems, including the determination of seepage losses, settlement computations, and stability analyses [5], many field and laboratory investigations of permeability have been made [6- 19]. For example, Hazen [6, 7] developed an empirical formula (k=cD_{10}^2) for

Table 1. Coefficient of permeability, k (m/s) [13].

Permeability (m/s)	10^0	10^{-1}	10^{-2}	10^{-3}	10^{-4}	10^{-5}	10^{-6}	10^{-7}	10^{-8}	10^{-9}	10^{-10}	10^{-11}
Drainage	Good						Poor		Practically impervious			
Soil Types	Clean gravel		Clean sands, cleansand & gravel mixtures			Very fine sands, organic & inorganic silts, mixtures of sand silt & clay, glacial till, stratified clay deposits, etc.			Impervious soils e.g., homogeneous clays below zone of weathering			
						"Impervious" soils modified by effects of vegetation & weathering						

predicting the hydraulic conductivity of saturated sands. Kozeny [8], and Carman [9, 10], who presented widely accepted derivations for permeability, developed a semi-empirical formula for predicting the permeability of porous media. Goktepe and Sezer [15] have recently proposed a new method for obtaining the shape coefficient for the Kozeny-Carman equation. Shepherd [17] conducted statistical power-regression analyses on 19 sets of published data on the hydraulic conductivity of unconsolidated sediments vs. grain size. Alyamani and Sen [19] proposed an equation based on an analysis of 32 samples incorporating the initial slope and the intercept of the grain-size distribution curve. Sperry and Peirce [20] developed a model for delineating the importance of particle size/shape, and porosity in explaining the variability of the hydraulic conductivity of a granular porous medium. They concluded that the Hazen equation provides the best estimate of the hydraulic conductivity of the media studied, except for the irregularly shaped particles. Ishaku et al. [21] have recently employed several empirical formulae to specify the hydraulic conductivity of aquifer materials in the field. They stated that the most accurate estimation of the hydraulic conductivity was found using the Terzaghi equation, followed by the Kozeny-Carman, Hazen, Breyer and Slitcher equations, respectively. Although many different techniques have been proposed to determine its value, including field methods (the pumping-of-wells test, the auger-hole test and the tracer test), laboratory methods (the falling-head test, the constant-head test), and calculations from the empirical formulae of Todd and Mays [22], an accurate estimation of hydraulic conductivity, particularly in the field, is inadequately quantified. Applications of these empirical formulae to the same porous medium material can yield different values of hydraulic conductivity due to the difficulty of including all possible variables in the porous media Vukovic and Soro [23].

It has long been understood that particle shape characteristics have a significant effect on the engineering properties of the soil matrix [24- 29]. Terzaghi [24] was one of the first engineers to make an investigation to understand the shape characteristics using flat-grained constituents. The observations made by Gilboy [25] that any system of analysis or classification of soil that neglects the presence and effect of the shape will be incomplete and erroneous. Numerous researches have carried out investigations, because of the importance of particle shape and its role in the behaviour of sands for practicing engineers and researchers in helping to estimate soil behaviour. Holubec and D'Appolinia [30] showed that the results of dynamic penetration tests in sands depend on the particle shape. Cornforth [31], and Holtz and Kovacs [32] demonstrated how particle shape impacts on the internal fiction angle (φ). Cedergren [33] pointed out that particle shape affects the permeability. Particle shape also plays a significant role in the liquefaction potential [34]. Wadell [35], Krumbein [36], Powers [37], Holubec and D'Appolinia [30], Youd [38], and Cho et al. [39] have introduced detailed explanations for the particle shape. Two independent properties are typically employed to describe the shape of a soil particle: (i) roundness is a measure of the extent to which the edges and corners of a particle have been rounded, and (ii) sphericity (form) describes the overall shape of a particle, since it is a measure of the extent to which a particle approaches the shape of a sphere. Wadell [35] proposed a simplified sphericity (S) parameter, ($D_{max\text{-}insc}/D_{min\text{-}circ}$), where $D_{max\text{-}min}$ is the diameter of a maximum inscribed circle and $D_{min\text{-}circ}$ is the diameter of a minimum sphere circumscribing a gravel particle. Wadell [35] defined the roundness (R) as $D_{i\text{-}ave}/D_{max\text{-}insc}$, where $D_{i\text{-}ave}$ is the average diameter of the inscribed circle for each corner of the particle. Figures 3-5 describe R, S and a chart for a comparison between them to determine the particle shape [36, 37].

A widely know aspect of hydraulic conductivity equations in the literature is the determination of an empirical relationship between the hydraulic conductivity and the porosity, the effective diameter, or a portion of the grain size distribution curve, etc. However, these parameters cannot yield consistent results with respect to the

actual hydraulic conductivity values. Therefore, this paper attempts to relate the grain size, and in particular the shape parameters (i.e., roundness, sphericity), to hydraulic conductivity estimates. The major objectives of this study are, first, to conduct a number of permeability tests in the laboratory using sands artificially graded to certain size ranges to provide uniform specimens for classification purposes, and second, to relate the test results to hydraulic conductivity estimates.

2 EXPERIMENTAL STUDY

The materials used in the tests described in this study were Crushed Stone Sand (CSS), Trakya Sand (TS), Narli Sand (NS), Fly Ash Pellets (FAPs), Leighton Buzzard Sand (LBS) having distinct shapes and sizes falling between 0.60 mm and 1.18 mm, 1.18 mm and 2.00 mm, and 0.075 and 2.00 mm. Figure 1 indicates the particle size distribution of the sands used during the experimental study. Some properties (D_{10}, D_{30}, D_{60}, c_u, c_c, G_s, e_{max}, e_{min}) of the sands including roundness (R) and sphericity (S) estimations based on the study by Muszynski and Vitton [47] are listed in Table 2. Scanning electron microscope (SEM) images show the physical differences/similarities among the sands used during this investigation (Figure 2). The sands were tested using a constant-head permeability testing apparatus at a relative density (D_r) of about 35% and constant room temperature (20°C). The specimens, at the required

Table 2. Summary of the specimen data.

Sample	Gradation (mm)	USCS	G_s	e_{max}	e_{min}	especimen	dspecimen (g/cm^3)	R	S	k (cm/sec)
CSS	0.075-2.00	SW	2.66	0.787	0.435	0.664	1.599	0.15	0.55	0.189
	1.18-2.00	SP		0.900	0.604	0.796	1.481			1.259
	0.6-1.18	SP		1.013	0.668	0.892	1.406			0.418
TS	0.075-2.00	SW	2.65	0.744	0.450	0.641	1.615	0.43	0.67	0.173
	1.18-2.00	SP		0.874	0.627	0.788	1.483			1.231
	0.6-1.18	SP		0.931	0.679	0.843	1.438			0.375
NS	0.075-2.00	SW	2.68	0.581	0.335	0.495	1.793	0.72	0.79	0.139
	1.18-2.00	SP		0.720	0.506	0.645	1.629			1.097
	0.6-1.18	SP		0.795	0.543	0.707	1.570			0.296
FAP	0.075-2.00	SW	1.75	1.091	0.734	0.966	0.890	0.65	0.89	0.269
	1.18-2.00	SP		1.168	0.856	1.059	0.850			1.458
	0.6-1.18	SP		1.280	0.916	1.153	0.813			0.597
LBS	0.6-1.18	SP	2.65	0.842	0.525	0.731	1.531	0.78	0.65	0.323

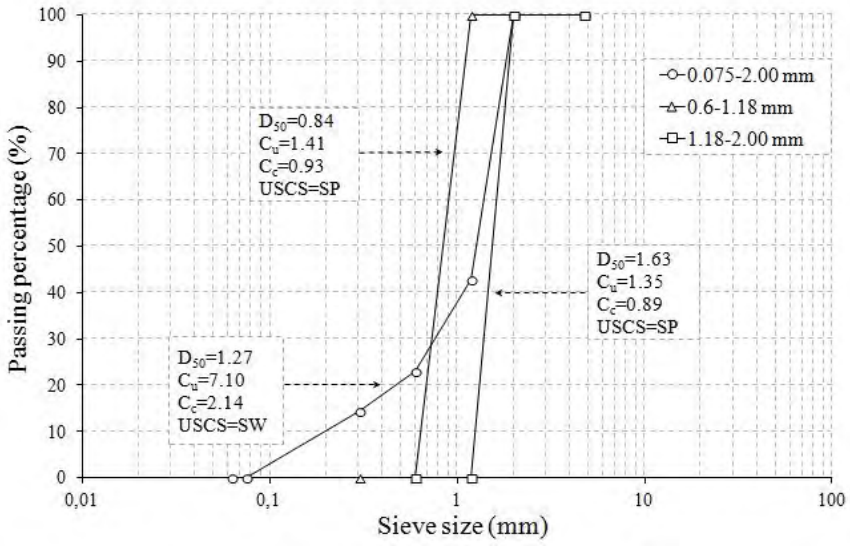

Figure 1. Particle size distribution for the sands used during the experimental study.

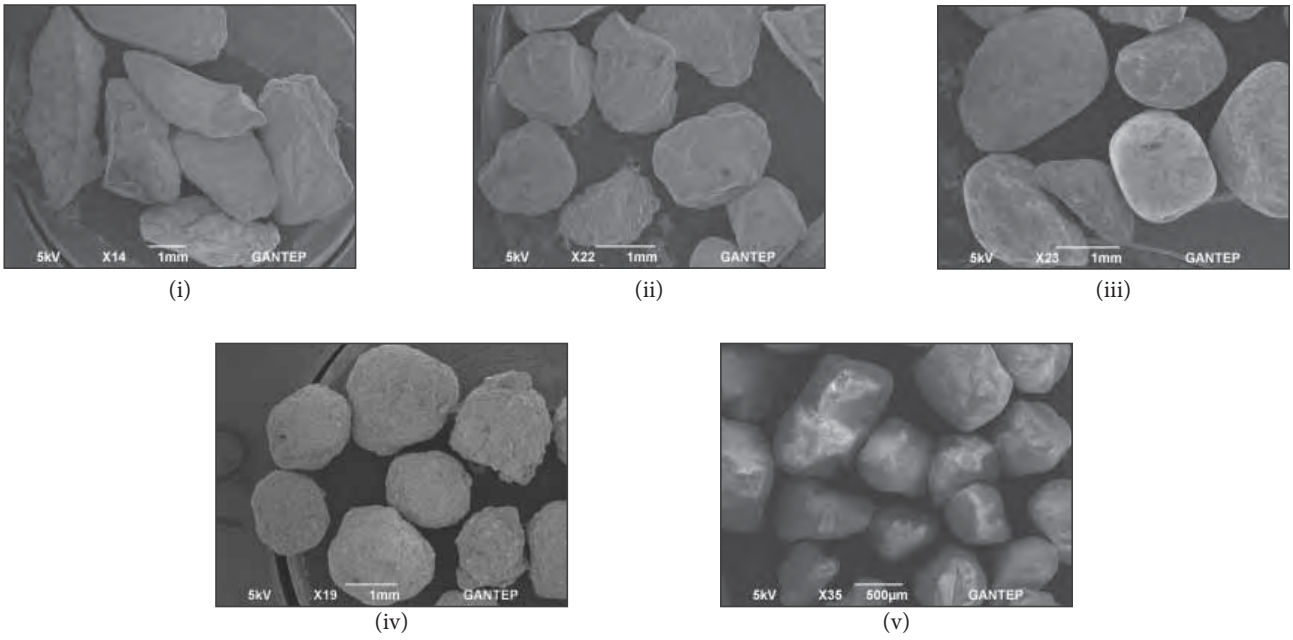

Figure 2. Scanning Electron Microscopy (SEM) images of the sands used during the experimental study (i- Crushed Stone Sand, ii. Trakya Sand, iii- Narli Sand, iv- Fly Ash Pellets, v- Leighton Buzzard Sand).

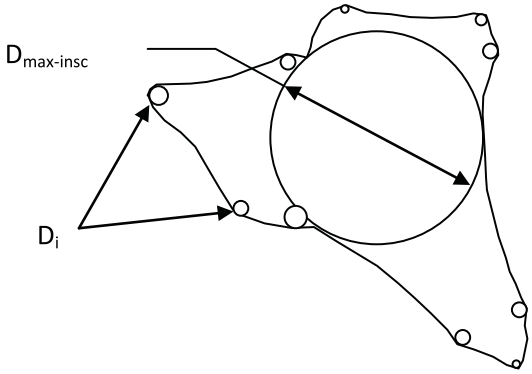

Figure 3. Graphical representation of roundness, *R* (redrawn from Muszynski and Vitton [47]).

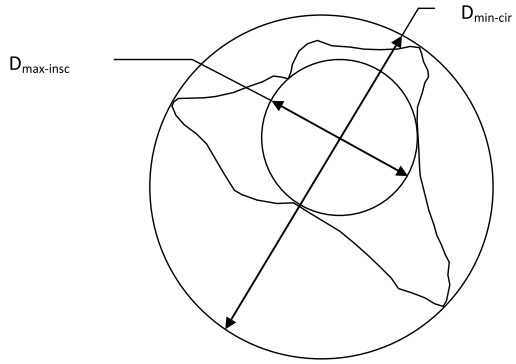

Figure 4. Graphical representation of sphericity, *S* (redrawn from Muszynski and Vitton [47]).

relative density (35%), are placed in a plexiglass cylindrical cell of about 50 cm^2 cross-sectional area (*A*). The specimens rest on a wire mesh at the bottom of the cell, which is a square grid of uniformly placed wires. The volume of the water (*q*) flowing during a certain time (*t*) is measured when a steady vertical water flow, under a constant head, is maintained through the soil specimen. Then, the *k* values of the specimens tested were calculated using Darcy's law ($k=ql/Ah$).

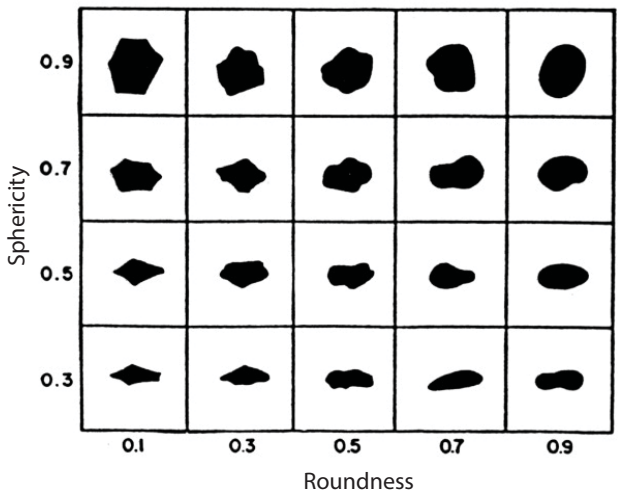

Figure 5. Comparison chart [49].

3 RESULTS AND DISCUSSION

Table 2 gives a summary of the specimens used in the tests reported here. The initial relative densities of all the specimens were around 35%. The specimens were loose to medium dense. Three different sizes of artificially graded CSS, TS, NS, FAP, and LBS sands, which have exactly the same gradation characteristics (D_{10}, D_{30},

Table 3. Empirical equations and their predictions on the sands tested in this paper.

Researcher/ Organization	Equation	Sample	k (cm/sec) 0.6-1.18 mm	k (cm/sec) 1.18-2.00 mm	k (cm/sec) 0.075-2.00 mm
Hazen	$k = 6\times10^{-4}\, x\frac{g}{v} x\left[1+10\left(n-0.26\right)\right] x\left(d_{10}\right)^2$	LBS*	0.6349	-	-
		TS$^-$	0.7196	2.5909	0.0545
		NS$^+$	0.6151	2.1434	0.0404
		CSS[1]	0.7540	2.6162	0.0565
		FAP[2]	0.9087	3.2713	0.0783
Kozeny-Carman	$k = 8.3\times10^{-3}\, x\frac{g}{v} x\left[\frac{n^3}{\left(1-n\right)^2}\right] x\left(d_{10}\right)^2$	LBS	0.7556	-	-
		TS	1.0872	3.4910	0.0525
		NS	0.6926	2.0844	0.0265
		CSS	1.2566	3.5916	0.0575
		FAP	2.3808	7.3642	0.1500
Terzaghi	$k = 0.0084\, x\frac{g}{v} x\left[\frac{n-0.13}{\sqrt[3]{1-n}}\right]^2 x\left(d_{10}\right)^2$	LBS	0.3229	-	-
		TS	0.4220	1.4208	0.0242
		NS	0.3022	0.9576	0.0135
		CSS	0.4676	1.4507	0.0260
		FAP	0.7181	2.3895	0.0525
Chapuis	$k = 1.5x\left(d_{10}\right)^2 x\frac{e^3}{1+e} x\frac{1+e_{\max}}{\left(e_{\max}\right)^3}$	LBS	0.4279	-	-
		TS	0.4776	1.7980	0.0408
		NS	0.4541	1.7625	0.0392
		CSS	0.4466	1.7176	0.0387
		FAP	0.4751	1.8385	0.0443
Slitcher	$k = 1\times10^{-2} x\frac{g}{v} x\, n^{3.287} x\left(d_{10}\right)^2$	LBS	0.2372	-	-
		TS	0.3082	1.0403	0.0179
		NS	0.2224	0.7093	0.0104
		CSS	0.3408	1.0617	0.0192
		FAP	0.5175	1.7296	0.0381
USBR	$k = 4.8\times10^{-3} x\frac{g}{v} x\left(d_{20}\right)^{0.3} x\left(d_{20}\right)^2$	LBS	0.2535	-	-
		TS	0.2535	1.0882	0.1048
		NS	0.2535	1.0882	0.1048
		CSS	0.2535	1.0882	0.1048
		FAP	0.2535	1.0882	0.1048
NAVFAC	$k = 10^{1.291e-0.6435} x\left(d_{10}\right)^{10^{(0.5504-0.2937e)}}$	LBS	0.7593	-	-
		TS	1.1357	3.7613	0.0376
		NS	0.6953	2.5811	0.0166
		CSS	1.3549	3.8503	0.0426
		FAP	3.3791	7.7911	0.2052
Alyamani & Sen	$k = 1300x\left[l_0 + 0.025\left(d_{50}-d_{10}\right)\right]^2$	LBS	0.5691	-	-
		TS	0.5691	2.1289	0.0418
		NS	0.5691	2.1289	0.0418
		CSS	0.5691	2.1289	0.0418
		FAP	0.5691	2.1289	0.0418
Breyer	$k = 6\times10^{-4} x\frac{g}{v} x\log\left[\frac{500}{C_u}\right] x\left(d_{10}\right)^2$	LBS	0.6172	-	-
		TS	0.6172	2.3718	0.0437
		NS	0.6172	2.3718	0.0437
		CSS	0.6172	2.3718	0.0437
		FAP	0.6172	2.3718	0.0437

LBS*: Leighton Buzzard sand; TS$^-$: Trakya sand; NS$^+$: Narli sand; CSS[1]: Crushed stone sand; FAP[2]: Fly ash pellet

D_{60}, c_u, c_c) (Figure 1) within the specified ranges, were classified as 'well graded' (*SW*) and 'poorly graded' (*SP*) based on the Unified Soil Classification System (USCS). The specific gravity of the grains, apart from the FAP specimens, were found to be between 2.65 and 2.68. The specific gravity of the FAP was found to be 1.75. Fly Ash Pellets (FAPs), as lightweight aggregates, were produced from fly ash and cement mixing using the pelletization method. The crushing strength, specific gravity, water absorption, surface characteristics and shear strength properties of the manufactured aggregates were already evaluated. The researchers showed that these manufactured aggregates could be a good alternative in some civil-engineering applications. The specific-gravity values of the fly ash pellets change with the fly ash and cement type, and the mix ratio of the constituents [40, 41]. The FAP specimens have a lower density (ρ) and a higher void ratio (e) than the other specimens, because the specific gravity of the soil grains is used in calculating the void ratio. As can be seen from Table 2, the densities of the FAP specimens, calculated after obtaining the void ratios, are lower than the others, for all three gradation ranges. Based on the roundness criteria and the values proposed by Powers [37] and Youd [38] the specimens used during the experimental investigation vary from very angular (i.e., CSS) to well rounded (i.e., LBS).

Table 3 presents the empirical equations and their implications for the sands tested for hydraulic conductivity in this experimental investigation. Hazen, Kozeny- Carman, Terzaghi, Chapuis, Slitcher, USBR, NAVFAC, Alyamani and Sen, and Breyer's equations were considered in this study. The Hazen formula was developed for a prediction of the hydraulic conductivity of uniformly graded loose sand with cu less than 5, and an effective grain size (d_{10}) between 0.10 and 3.0 mm. It is clear from Table 3 that the hydraulic conductivity values (k) vary from 0.6151 cm/sec to 0.9087 cm/sec for the sands falling between 0.6 and 1.18 mm, from 2.1434 cm/sec to 3.2713 cm/sec for the sands falling between 1.18 and 2.00 mm, and from 0.0404 cm/sec to 0.0783 cm/sec for the sands falling between 0.075 and 2.00 mm. Based on the limitation of c_u specified, as expected, the formula does not give realistic prediction results for the sands falling between 0.075 and 2.00 mm (see Figure 6). The authors' interpretation is that the effect of the parameter c_u was neglected, and thereby the grain size distribution results yield the same cu for various sands. The Kozeny-Carman formula is one of the widely used derivations for hydraulic conductivity calculations. This equation is not applicable for either soil with an effective size above 3 mm, or for clayey soils [42]. The estimated hydraulic conductivity values (k) vary from 0.6926 cm/sec to 2.3808 cm/sec for the sands falling between 0.6 and 1.18 mm, from 2.0844 cm/sec to 7.3642 cm/sec for the sands falling between 1.18 and 2.00 mm, and from 0.0265 cm/sec to 0.1500 cm/sec for the sands falling between 0.075 and 2.00 mm. The predicted hydraulic conductivity values (k) using the Terzaghi formula vary from 0.3022 cm/sec to 0.7181 cm/sec for the sands falling between 0.6 and 1.18 mm, from 0.9576 cm/sec to 2.3895 cm/sec for the sands falling between 1.18 and

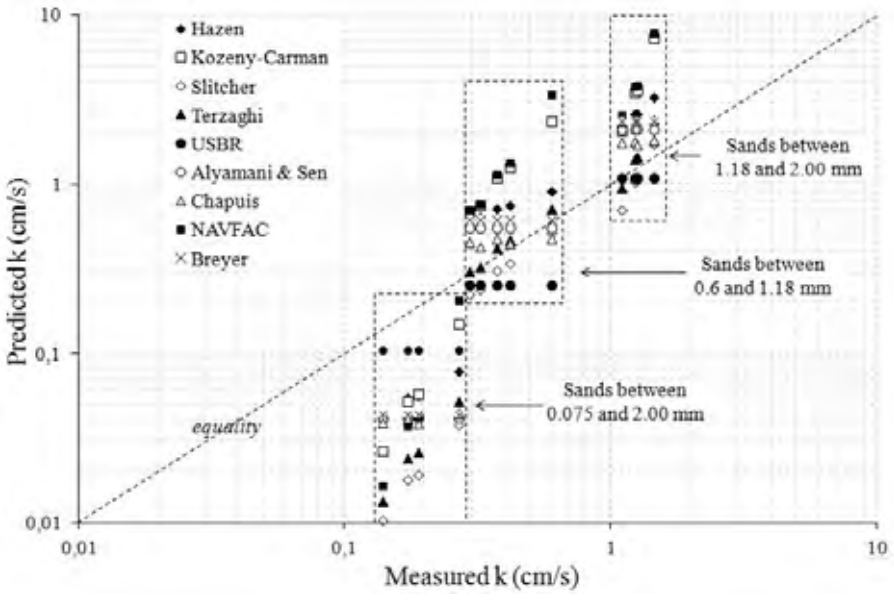

Figure 6. Predicted versus measured k values for the sands used during the during the experimental study.

Table 4. Empirical equations and their limitations for permeability estimates.

Researcher/ Organization	Equation	Limitations
Hazen	$k = 6\times10^{-4}\, x\, \frac{g}{v}\, x\left[1+10\left(n-0.26\right)\right] x\left(d_{10}\right)^2$	$c_u < 5$ $0.1 < d_{10} < 3.0$
Kozeny-Carman	$k = 8.3\times10^{-3}\, x\, \frac{g}{v}\, x\left[\frac{n^3}{\left(1-n\right)^2}\right] x\left(d_{10}\right)^2$	$0.5 < d_{10} < 4.0$
Terzaghi	$k = 0.0084\, x\, \frac{g}{v}\, x\left[\frac{n-0.13}{\sqrt[3]{1-n}}\right]^2 x\left(d_{10}\right)^2$	-
Chapuis	$k = 1.5 x\left(d_{10}\right)^2 x\, \frac{e^3}{1+e}\, x\, \frac{1+e_{\max}}{\left(e_{\max}\right)^3}$	-
Slitcher	$k = 1\times10^{-2}\, x\, \frac{g}{v}\, x\, n^{3.287} x\left(d_{10}\right)^2$	$0.1 < d_{10} < 5.0$
USBR	$k = 4.8\times10^{-3}\, x\, \frac{g}{v}\, x\left(d_{20}\right)^{0.3} x\left(d_{20}\right)^2$	$c_u < 5$
NAVFAC	$k = 10^{1.291\, e-0.6435}\, x\left(d_{10}\right)^{10^{(0.5504-0.2937\, e)}}$	$2 < c_u < 12$ $0.1 < d_{10} < 2.0$ $0.3 < e < 0.7$ $1.4 < d_{10}/d_5$
Alyamani & Sen	$k = 1300 x\left[l_0 + 0.025\left(d_{50} - d_{10}\right)\right]^2$	-
Breyer	$k = 6\times10^{-4}\, x\, \frac{g}{v}\, x \log\left[\frac{500}{C_u}\right] x\left(d_{10}\right)^2$	$0.06 < d_{10} < 0.6$ $1 < c_u < 20$

2.00 mm, and from 0.0135 cm/sec to 0.0525 cm/sec for the sands falling between 0.075 and 2.00 mm. Figure 6 presents a comparative study using all the formulae employed in this study. As can be seen from the Figure 6, Terzaghi's empirical equation has more accurate results than the other equations for the sands between 0.6 and 1.18 mm, and those between 1.18 and 2.00 mm. This equation, however, seems not to be appropriate for the soils between 0.075 and 2.00 mm, although it has no limitations reported (Table 4). Similarly, predicted *k* values using the Chapuis formula give us a relatively good correlation with the measured *k* values for the sands between 0.6 and 1.18 mm, and between 1.18 and 2.00 mm (Figure 6). Although there is no limitation for this approach as well, the estimated *k* values do not fit very well to the actual *k* values determined experimentally. The estimated hydraulic conductivity values (*k*) using the Chapuis approach vary from 0.4279 cm/sec to 0.4776 cm/sec for the sands falling between 0.6 and 1.18 mm, from 1.7176 cm/sec to 1.8385 cm/sec for the sands falling between 1.18 and 2.00 mm, and from 0.0387 cm/sec to 0.0443 cm/sec for the sands falling between 0.075 and 2.00 mm. The limitations of the empirical equation developed by Slitcher is that the d10 should be between 0.01 and 5.0 (Table 4). Figure 6 indicates that the Slitcher formula is the best fitted to the sands between 0.6 and 1.18 mm, and between 1.18 and 2.00 mm. However, the *k* predictions for the sand between 0.075 and 2.00 mm have no good agreement with the measured *k* values (Figure 6). Estimated *k* values using the Slitcher approach vary from 0.2224 cm/sec to 0.5175 cm/sec for the sands falling between 0.6 and 1.18 mm, from 0.7090 cm/sec to 1.7296 cm/sec for the sands falling between 1.18 and 2.00 mm, and from 0.0104 cm/sec to 0.0381 cm/sec for the sands falling between 0.075 and 2.00 mm. The US Bureau of Reclamation (USBR) formula estimates *k* values using the effective grain size (d_{20}), and it does not depend on the porosity (Table 4). The formula is most suitable for medium-grain sand with c_u less than 5 [43]. The estimated *k* values using the USBR formula

are 0.2535 cm/sec for the sands falling between 0.6 and 1.18 mm, 1.0882 cm/sec for the sands falling between 1.18 and 2.00 mm, and 0.1048 cm/sec for the sands falling between 0.075 and 2.00 mm. The k values are same for each of three gradations due to the same d_{20}. The Alyamani and Sen equation, one of the well-known equations, considers both sediment grain sizes d_{10} and d_{50} as well as the sorting characteristics. Estimated k values using the Alyamani and Sen approach are 0.5691 cm/sec for the sands falling between 0.6 and 1.18 mm, 2.1289 cm/sec for the sands falling between 1.18 and 2.00 mm, and 0.0418 cm/sec for the sands falling between 0.075 and 2.00 mm. The k values are the same for each gradation of sands due to the same d_{10} and d_{50} values. Similarly, the Breyer equation gives the same k values for each gradation, 0.6172 cm/sec for the sands falling between 0.6 and 1.18 mm, 2.3718 cm/sec for the sands falling between 1.18 and 2.00 mm, and 0.0437 cm/sec for the sands falling between 0.075 and 2.00 mm, because of the same d_{10} value employed in this equation. The Naval Facilities Engineering Command design manual DM7 (NAVFAC) proposed a chart to predict the saturated k value of clean sand and gravel based on e and d_{10}. The limitations described in this approach are $0.3 < e < 0.7$, $0.10 < d_{10} < 2.0$ mm, $2 < c_u < 12$, and $d_{10}/d_5 < 1.4$. Estimated k values using NAVFAC vary from 0.6953 cm/sec to 3.3791 cm/sec for the sands falling between 0.6 and 1.18 mm, from 2.5811 cm/sec to 7.7911 cm/sec for the sands falling between 1.18 and 2.00 mm, and from 0.0166 cm/sec to 0.2052 cm/sec for the sands falling between 0.075 and 2.00 mm. The observed differences between the predicted and measured k values calculated using different equations (see Figure 6) could be because of some inaccuracies in the measured soil parameters, and some deficiencies in the predictive equations, as previously discussed. Finally, it also seems to be worth bearing in mind that the Vukovic and Soro [23] porosity (n) may be derived from the empirical relationship with the coefficient of grain uniformity (c_u) as $n=0.255(1+0.83c_u)$. However, the porosity value (n) employed here in the empirical equations has been considered as equal to $e/e+1$, as described by Terzaghi and Peck [13], Craig [2], Powrie [4], and Das [3]. This is because, the approach by Vukovic and Soro [23] may not be applicable for the sands having the same c_u values as described here in this investigation.

Figure 7 shows the variation of the coefficient of permeability (k) values and the void ratio (e) for the sands tested, and the regression results for each of the three gradations. The results demonstrate that the higher e values cause higher k values for the measured type of sands. In general, if the void ratio is high, particles are free to rotate, which results in higher k values [44-45]. In densely packed soils with a low void ratio, a larger number of contacts per particle resulted in lower k values. Comparing the hydraulic conductivity values of CSS, TS, NS, and LBS, it is clear that the granular packing in more angular soil grain samples has a more open fabric than those in relatively rounded soil grain samples, resulting in higher k values in more angular sands with the G_s about 2.66. However, the FAP specimens with G_s about 1.75 exhibit much higher k values. The authors interpreted the reason could be attributed to the (i) the dispersion of fly ash particles on the pellet grains during the saturation phase and testing, or (ii)

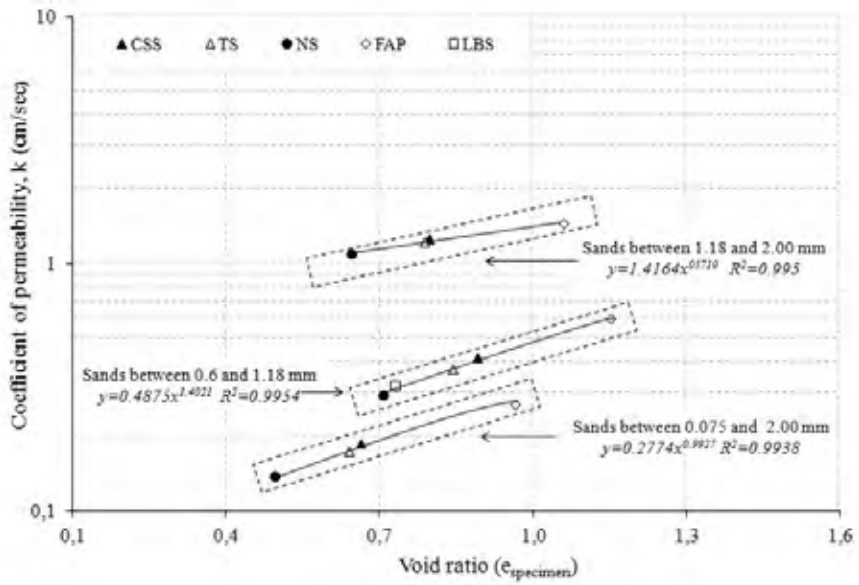

Figure 7. Graph of permeability against void ratio for the sands used during the experimental study.

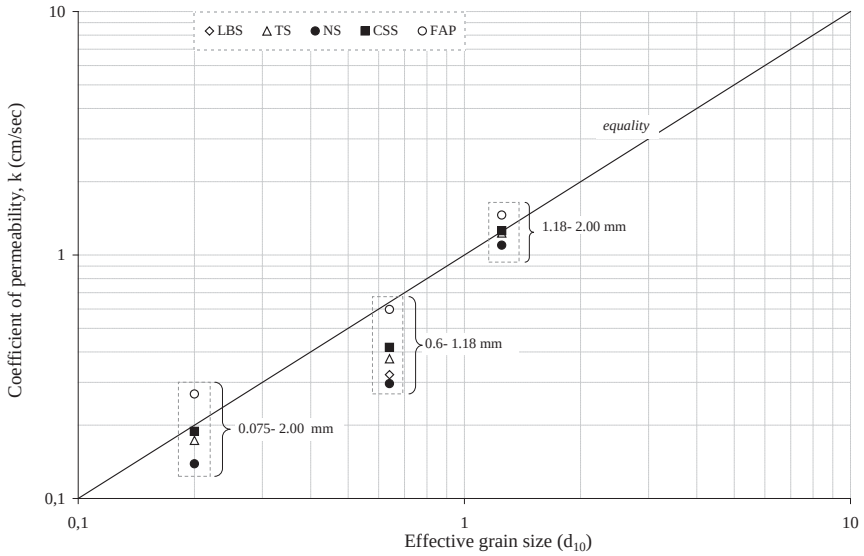

Figure 8. Plot of permeability against grain size for the sands used during the during the experimental study.

the lower specific gravity value of the FAP grains, which may cause a more open fabric because such grains are less likely to settle. Figure 8 illustrates a plot of hydraulic conductivity vs. grain size for the sands used in the experimental study. As can be seen, the measured k values are close to the each other for the sand specimens with d_{10} values about 1.20.

In this study, as an alternative approach, a stepwise regression (SR) model based on a laboratory study is proposed for the prediction of the hydraulic conductivity of the sands. In statistics, a SR contains regression models where the selection of predictive variations is conducted by a semi-automated process. The input variables in the developed SR models are the coefficient of uniformity (c_u), coefficient of curvature (c_c), specific gravity (G_s), porosity (n), roundness (R), and sphericity (S), while the output is k. As shown in Figure 9, comparing the results from the experiments and from the equation proposed here in this study, the accuricies of the proposed SR models are found to be quite satisfactory (R^2=0.9933). The results confirmed that the SR method can identify the k value effectively, while certain available methods result in an error. The developed model provides a way of expressing information to assess the contribution of each parameter (c_u , c_c , G_s , n, R, S) to the variance of the model output (k). The parameters c_u and c_c are more influential than the parameters R and S in Equation 1, and thereby changes in the hydraulic conductivity may be primarily due to the size of the grains. Evidently, the proposed SR model is also presented as a simple explicit mathematical function for further use by researchers. The SR equation (Eq. 1) is as follows:

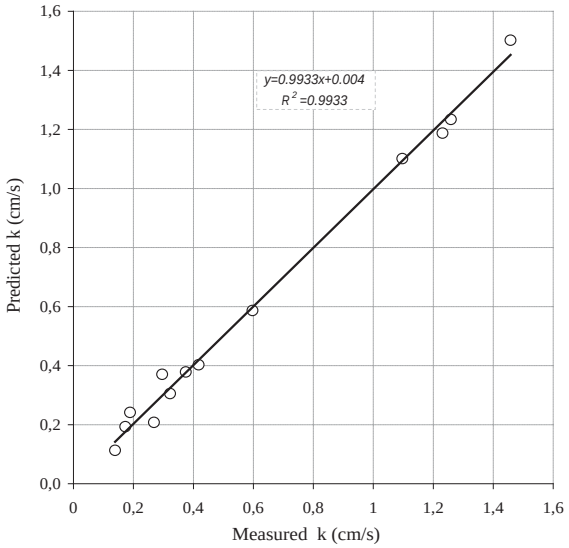

Figure 9. Comparison of the experimental results and predictions by proposed SR model.

$$k(cm/s) = 0.065 + 0.029 \cdot \frac{c_u}{c_c{}^4 \cdot (G_s \cdot n)^2} - \frac{0.21R^2}{S} \qquad (1)$$

The hydraulic conductivity (k), roundness (R), and sphericity (S) relationship can be seen in the 3-D plot in Figure 10. The k value increases in a relatively linear pattern with a decrease in the roundness. However, it was realized that the sphericity value is not very effective for the k value, while the grains have a higher value of roundness. On the other hand, the k value exhibits an increasing trend at lower roundness values, while the sphericity increases.

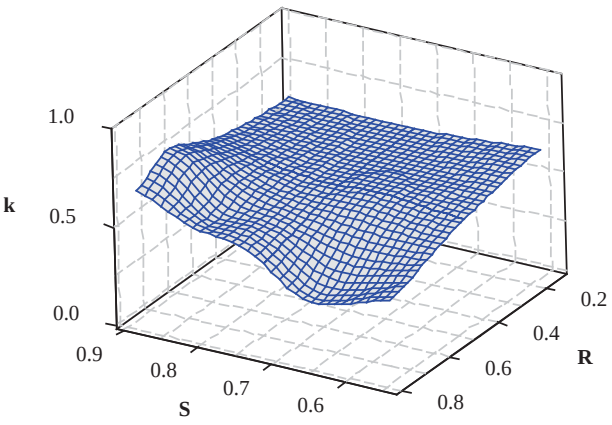

Figure 10. Surface plot of hydraulic conductivity (k) vs. roundness (R), sphericity (S).

4 CONCLUSIONS

In this investigation, three ranges of particle size (0.60-1.18 mm, 1.18-2.00 mm, and 0.075-2.00 mm) of five different sands (i. Crushed Stone Sand, CSS; ii. Trakya Sand, TS; iii. Narli Sand, NS; iv. Fly Ash Pellets, FAP; v. Leighton Buzzard Sand, LBS) having distinct shapes (R_i=0.15, S_i=0.55; R_{ii}=0.43, S_{ii}=0.67; R_{iii}=0.72, S_{iii}=0.79; R_{iv}=0.65, S_{iv}=0.89; R_v=0.78 S_v=0.65) were tested in a constant-head permeability testing apparatus at a relative density (D_r) of about 35%. Also, already available empirical permeability equations were briefly discussed for an estimation of the coefficient of permeability values (k). The tests reported in this paper indicate three new facets of behaviour:

1. Sands having different shapes (R, S) with the same grading characteristics (c_u, c_c, D_{10}, D_{30}, D_{50}, D_{60}) result in different k values.
2. Relatively rounded sand grains have lower k values than the angular sand grains with the exception of the FAP specimens. This could be due to (i) the dispersion of fly ash particles on the FAP grains during the saturation phase and testing, or (ii) the lower specific gravity value of the FAP grains.
3. Empirical equations by Terzaghi and Slitcher give more accurate results than the other equations [6, 8, 19, 46, 51] employed to predict the k values of the sand specimens tested in this investigation.

This suggests that the already-available methods employed here are capable of, but not sufficient for, an accurate prediction of the k values. Therefore, it is obvious that further investigations of the microstructural behavior of the soil matrix are required in order to gain an insight regarding the shape and size effects on permeability.

REFERENCES

[1] Freeze, R. A., Cherry, J.A. 1979. Groundwater. Prentice Hall Inc., Englewood Cliffs, New Jersey.
[2] Craig, R.F. 1997. Craig's Soil Mechanics, 2nd ed. Taylor and Francis, London.
[3] Das, B.M. 2008. Advanced Soil Mechanics, 3rd ed. Taylor and Francis, London.
[4] Powrie, W. 2004. Soil Mechanics Concepts & Applications, 2nd ed. Taylor and Francis, London.
[5] Boadu, F.K. 2000. Hydraulic Conductivity of Soils from Grain-Size Distribution: New Models. Journal of Geotechnical and Geoenvironmental Engineering 126, 8, 739-746. http://dx.doi.org/10.1061/(ASCE)1090-0241(2000)126:8(739)
[6] Hazen, A. 1892. Some Physical Properties of Sands and Gravels, with Special Reference to their Use in Filtration. 24th Annual Report, Massachusetts State Board of Health, Pub. Doc. 34, 539-556.
[7] Hazen, A. 1911. Discussion: dams on sand foundations. Transactions of the American Society of Civil Engineers 73, 199–203.
[8] Kozeny, J. 1927. Uber Kapillare Leitung Des Wassers in Boden. Sitzungsber Akad. Wiss. Wien Math. Naturwiss. Kl., Abt.2a, 136, 271-306 (In German).
[9] Carman, P.C. 1937. Fluid Flow through Granular Beds. Trans.Inst.Chem. Eng. 15,150.
[10] Carman, P.C. 1956. Flow of Gases through Porous Media. Butterworths Scientific Publications, London.
[11] Krumbein W.C., Monk G.D. 1942. Permeability as a function of the size parameters of unconsolidated sand. American Institute of Mining and Engineering, Littleton, CO. Tech. Pub. 153-163.
[12] Harleman D.R.F., Melhorn P.F., Rumer, R.R. 1963. Dispersion-permeability correlation in porous media. Am. Soc. Civ. Eng. (NY) 89, 67-85.
[13] Terzaghi, K., Peck, R.B. 1964. Soil Mechanics in Engineering Practice. Wiley, New York.
[14] Masch, F.D., Denny, K.T. 1966. Grain-size distribution and its effect on the permeability of unconsolidated sands. Water Res. 2, 665-677.
[15] Goktepe, A.B., Sezer, A. 2010. Effect of particle shape on density and permeability of sands. Proceedings of the Institution of Civil Engineer-Geotechnical Engineering 163 (6), 307-320.
[16] Wiebega, W.A., Ellis, W.R., Kevi, L. 1970. Empirical relations in properties of unconsolidated quartz sands and silts pertaining to water flow. Water Res., 6, 1154-1161.
[17] Shepherd, R.G. 1989. Correlations of permeability and Grain-size. Groundwater 27(5), 663-638.
[18] Uma, K.O., Egboka, B.C.E., Onuoha, K.M. 1989. New statistical grain-size method for evaluating the hydraulic conductivity of sandy aquifers. J. Hydrol. 108, 143-366.
[19] Alyamani, M.S., Sen, Z. 1993. Determination of Hydraulic Conductivity from Grain-Size Distribution Curves. Groundwater 31(4), 551-555.

[20] Sperry, M.S., Peirce, J.J. 1995. A model for estimating the hydraulic conductivity of granular material based on grain shape, grain size and porosity. Ground Water, 33(6), 892- 898. doi: 10.1111/j.1745-6584.1995.tb00033.x
[21] Ishaku, J.M., Gadzama, E.W., Kaigama, U. 2011. Evaluation of empirical formulae for the determination of hydraulic conductivity based on grain-size analysis. Journal of Geology and Mining Research, 4, 105-113
[22] Todd, D.K., Mays, L.W. 2005. Groundwater Hydrology. John Wiley & Sons, New York.
[23] Vukovic, M., Soro, A. 1998. Determination of Hydraulic Conductivity of Porous Media from Grain-Size Composition. Water Resources Publications, Littleton, Colorado.
[24] Terzaghi, K. 1925. Erdbaumechanik auf bodenphysikalischer grundlage. Deuticke, Leipzig/Vienna.
[25] Gilboy, G. 1928. The compressibility of sand–mica mixtures. Proceedings of the ASCE 2, 555- 568.
[26] Lees, G. 1964. A new method for determining the angularity of particles. Sedimentology, 3, 2-21.
[27] Olson, R.E., Mesri, G. 1970. Mechanisms controlling the compressibility of clay. Journal of the Soil Mechanics and Foundations Division, ASCE 96 (SM6), Proc. Paper 7649, 1863-1878.
[28] Abbireddy, C.O.R., Clayton, C.R.I., Huvenne, V.A. 2009. A method of estimating the form of fine particulates. Geotechnique 59 (6), 503- 511. http://dx.doi.org/10.1680/geot.2008.P.009
[29] Clayton, C.R.I., Abbireddy, C.O.R., Schiebel, R. 2009. A method of estimating the form of coarse particulates. Geotechnique 59(6), 493-501. doi:10.1680/geot.2007.00195
[30] Holubec, I., D'Appolonia, E. 1973. Effect of particle shape on the engineering properties of granular soils. Evaluation of relative density and its role in geotechnical projects involving cohesionless soils. ASTM, STP523, West Conshohocken, PA, 304- 318.
[31] Conforth, D.H. 1973. Prediction of drained strength of sands from relative density measurements. Evaluation of relative density and its role in geotechnical projects involving cohesionless soils. Special technical publication 523, ASTM, West Conshohoken, PA, 281-303
[32] Holtz, R.D., Kovacs, W.D. 1981. An introduction to geotechnical engineering. Prentice-Hall, Englewood Cliffs, NJ, 517.
[33] Cedergren, H.R. 1989. Seepage, drainage, and flownets. 3rd ed., Wiley, New York, 26.
[34] Kramer, S.L. 1996. Geotechnical earthquake engineering. Prentice Hall, Upper Saddle River, NJ, 653.
[35] Wadell, H. 1932. Volume, shape, and roundness of rock particles. J. Geol., 40(5), 443- 451.
[36] Krumbein, W.C. 1941. Measurement and geological significance of shape and roundness of sedimentary particles. J. Sediment. Petrol., 11(2), 64- 72.
[37] Powers, M.C. 1953. A new roundness scale for sedimentary particles. Journal of Sedimentary Petrology 23(2), 117-119.
[38] Youd, T.L. 1973. Factors controlling maximum and minimum densities of sands, Evaluation of Relative Density and Its Role in Geotechnical Projects Involving Cohesionless Soils. ASTM STP 523, 98-112
[39] Cho, G.C., Dodds, J.S., Santamarina, J.C. 2006. Particle shape effects on packing density, stiffness and strength: Natural and crushed sands. J. Geotech. Geoenviron. Eng. 132(5), 591- 602. http://dx.doi.org/10.1061/(ASCE)1090-0241(2006)132:5(591)
[40] Doven. A.G. 1996. Lighweight fly ash aggregate production using cold bonding agglomeration process. PhD thesis, Bogazici University, Turkey.
[41] Arslan, H., Baykal, G. 2006. Utilization of fly ash as engineering pellet aggregates. Environ. Geol. 50, 761-770. doi: 10.1007/s00254-006-0248-7
[42] Carrier, W.D. 2003. Goodbye Hazen: Hello. Kozeny-Carman. J. Geotech. Geoenviron. Eng. 129,11, 1054-1056. http://dx.doi.org/10.1061/(ASCE)1090-0241(2003)129:11(1054)
[43] Cheng, C., Chen, X. 2007. Evaluation of Methods for Determination of Hydraulic Properties in an Aquifer- Aquitard System Hydrologically Connected to River. Hydrogeology Journal, 15, 669-678. doi: 10.1007/s10040-006-0135-z
[44] Zelasko, J. S., Krizek, R. J., Edil T. B. 1975. Shear Behavior of Sands as a Function of Grain Characteristics. Proc. Istanbul Conference on Soil Mechanics and Foundation Engineering, Turkish National Committee of Soil Mechanics and Geotechnical Engineering, Istanbul, Turkey, 55-64.
[45] Sukumaran, B., Ashmawy, A. K. 2001. Quantitative characterisation of the geometry of discrete particles. Geotechnique 51(7), 619-627. doi: http://dx.doi.org/10.1680/geot.2001.51.7.619
[46] Chapuis, R.P. 2004. Predicting the Saturated Hydraulic Conductivity of Sand and Gravel Using Effective Diameter and Void Ratio. Can. Geotech. J., 41, 787-795.
[47] Muszynski, M.R., Vitton, S.J., 2012. Particle shape estimates of uniform sands: visual and automated methods comparison. J. Mater. Civ. Eng. 24(2), 194-206. 10.1061/(ASCE)MT.1943-5533.0000351
[48] NAVFAC, 1974. Soil mechanics, foundations, and earth structures. Naval Facilities Engineering Command (NAVFAC) design manual DM7. U.S. Government Printing Office, Washington, D.C.
[49] Santamarina, J.C., Cho, G.C. 2004. Soil behaviour: The role of particle shape. The Skempton Conference, Thomas Telford, London, 604- 617.
[50] Slichter, C.S. 1898. Theoretical investigation of the motion of ground waters. 19th Annual Report. U.S. Geology Survey.
[51] USBR 1990. Earth Manual-Part 2, U.S. Department of the Interior Bureau of Reclamation, Denver, 1270 p.

NAVODILA AVTORJEM

Vsebina članka

Članek naj bo napisan v naslednji obliki:

- Naslov, ki primerno opisuje vsebino članka in ne presega 80 znakov.
- Izvleček, ki naj bo skrajšana oblika članka in naj ne presega 250 besed. Izvleček mora vsebovati osnove, jedro in cilje raziskave, uporabljeno metodologijo dela, povzetek izidov in osnovne sklepe.
- Največ 6 ključnih besed, ki bi morale biti napisane takoj po izvlečku.
- Uvod, v katerem naj bo pregled novejšega stanja in zadostne informacije za razumevanje ter pregled izidov dela, predstavljenih v članku.
- Teorija.
- Eksperimentalni del, ki naj vsebuje podatke o postavitvi preiskusa in metode, uporabljene pri pridobitvi izidov.
- Izidi, ki naj bodo jasno prikazani, po potrebi v obliki slik in preglednic.
- Razprava, v kateri naj bodo prikazane povezave in posplošitve, uporabljene za pridobitev izidov. Prikazana naj bo tudi pomembnost izidov in primerjava s poprej objavljenimi deli.
- Sklepi, v katerih naj bo prikazan en ali več sklepov, ki izhajajo iz izidov in razprave.
- Vse navedbe v besedilu morajo biti na koncu zbrane v seznamu literature, in obratno.

Dodatne zahteve

- Vrstice morajo biti zaporedno oštevilčene.
- Predložen članek ne sme imeti več kot 18 strani (brez tabel, legend in literature); velikost črk 12, dvojni razmik med vrsticami. V članek je lahko vključenih največ 10 slik. Isti rezultati so lahko prikazani v tabelah ali na slikah, ne pa na oba načina.
- Potrebno je priložiti imena, naslove in elektronske naslove štirih potencialnih recenzentov članka. Urednik ima izključno pravico do odločitve, ali bo te predloge upošteval.

Enote in okrajšave

V besedilu, preglednicah in slikah uporabljajte le standardne označbe in okrajšave SI. Simbole fizikalnih veličin v besedilu pišite poševno (npr. *v*, *T* itn.). Simbole enot, ki so sestavljene iz črk, pa pokončno (npr. Pa, m itn.). Vse okrajšave naj bodo, ko se prvič pojavijo, izpisane v celoti.

Slike

Slike morajo biti zaporedno oštevilčene in označene, v besedilu in podnaslovu, kot sl. 1, sl. 2 itn. Posnete naj bodo v katerem koli od razširjenih formatov, npr. BMP, JPG, GIF. Za pripravo diagramov in risb priporočamo CDR format (CorelDraw), saj so slike v njem vektorske in jih lahko pri končni obdelavi preprosto povečujemo ali pomanjšujemo.

Pri označevanju osi v diagramih, kadar je le mogoče, uporabite označbe veličin (npr. *v*, *T* itn.). V diagramih z več krivuljami mora biti vsaka krivulja označena. Pomen oznake mora biti razložen v podnapisu slike.

Za vse slike po fotografskih posnetkih je treba priložiti izvirne fotografije ali kakovostno narejen posnetek.

Preglednice

Preglednice morajo biti zaporedno oštevilčene in označene, v besedilu in podnaslovu, kot preglednica 1, preglednica 2 itn. V preglednicah ne uporabljajte izpisanih imen veličin, ampak samo ustrezne simbole. K fizikalnim količinam, npr. *t* (pisano poševno), pripišite enote (pisano pokončno) v novo vrsto brez oklepajev. Vse opombe naj bodo označene z uporabo dvignjene številke[1].

Seznam literature

Navedba v besedilu

Vsaka navedba, na katero se sklicujete v besedilu, mora biti v seznamu literature (in obratno). Neobjavljeni rezultati in osebne komunikacije se ne priporočajo v seznamu literature, navedejo pa se lahko v besedilu, če je nujno potrebno.

Oblika navajanja literature

V besedilu: Navedite reference zaporedno po številkah v oglatih oklepajih v skladu z besedilom. Dejanski avtorji so lahko navedeni, vendar mora obvezno biti podana referenčna številka.

Primer: »..... kot je razvidno [1,2]. Brandl and Blovsky [4], sta pridobila drugačen rezultat…«

V seznamu: Literaturni viri so oštevilčeni po vrstnem redu, kakor se pojavijo v članku. Označimo jih s številkami v oglatih oklepajih.

Sklicevanje na objave v revijah:

[1] Jelušič, P., Žlender, B. 2013. Soil-nail wall stability analysis using ANFIS. Acta Geotechnica Slovenica 10(1), 61-73.

Sklicevanje na knjigo:
[2] Šuklje, L. 1969. Rheological aspects of soil mechanics. Wiley-Interscience, London
Sklicevanje na poglavje v monografiji:
[3] Mitchel, J.K. 1992. Characteristics and mechanisms of clay creep and creep rupture, in N. Guven, R.M. Pollastro (eds.), Clay-Water Interface and Its Rheological Implications, CMS Workshop Lectures, Vol. 4, The clay minerals Society, USA, pp. 212-244..
Sklicevanje na objave v zbornikih konferenc:
[4] Brandl, H., Blovsky, S. 2005. Slope stabilization with socket walls using the observational method. Proc. Int. conf. on Soil Mechanics and Geotechnical Engineering, Bratislava, pp. 2485-2488.
Sklicevanje na spletne objave:
[5] Kot najmanj, je potrebno podati celoten URL. Če so poznani drugi podatki (DOI, imena avtorjev, datumi, sklicevanje na izvorno literaturo), se naj prav tako dodajo.

Podatki o avtorjih

Članku priložite tudi podatke o avtorjih: imena, nazive, popolne poštne naslove, številke telefona in faksa, naslove elektronske pošte. Navedite kontaktno osebo.

Sprejem člankov in avtorske pravlce

Uredništvo si pridržuje pravico do odločanja o sprejemu članka za objavo, strokovno oceno mednarodnih recenzentov in morebitnem predlogu za krajšanje ali izpopolnitev ter terminološke in jezikovne korekture. Z objavo preidejo avtorske pravice na revijo ACTA GEOTECHNICA SLOVENICA. Pri morebitnih kasnejših objavah mora biti AGS navedena kot vir.

Vsa nadaljnja pojasnila daje:

Uredništvo
ACTA GEOTECHNICA SLOVENICA
Univerza v Mariboru,
Fakulteta za gradbeništvo, prometno inženirstvo in arhitekturo
Smetanova ulica 17, 2000 Maribor, Slovenija
E-pošta: ags@uni-mb.si

INSTRUCTIONS FOR AUTHORS

Format of the paper

The paper should have the following structure:

- A Title, which adequately describes the content of the paper and should not exceed 80 characters;
- An Abstract, which should be viewed as a mini version of the paper and should not exceed 250 words. The Abstract should state the principal objectives and the scope of the investigation and the methodology employed; it should also summarise the results and state the principal conclusions;
- Immediately after the abstract, provide a maximum of 6 keywords;
- An Introduction, which should provide a review of recent literature and sufficient background information to allow the results of the paper to be understood and evaluated;
- A Theoretical section;
- An Experimental section, which should provide details of the experimental set-up and the methods used to obtain the results;
- A Results section, which should clearly and concisely present the data, using figures and tables where appropriate;
- A Discussion section, which should describe the relationships shown and the generalisations made possible by the results and discuss the significance of the results, making comparisons with previously published work;
- Conclusions, which should present one or more conclusions that have been drawn from the results and subsequent discussion;
- A list of References, which comprises all the references cited in the text, and vice versa.

Additional Requirements for Manuscripts

- Use double line-spacing.
- Insert continuous line numbering.
- The submitted text of Research Papers should cover no more than 18 pages (without Tables, Legends, and References, style: font size 12, double line spacing). The number of illustrations should not exceed 10. Results may be shown in tables or figures, but not in both of them.
- Please submit, with the manuscript, the names, addresses and e-mail addresses of four potential referees. Note that the editor retains the sole right to decide whether or not the suggested reviewers are used.

Units and abbreviations

Only standard SI symbols and abbreviations should be used in the text, tables and figures. Symbols for physical quantities in the text should be written in Italics (e.g. *v*, *T*, etc.). Symbols for units that consist of letters should

be in plain text (e.g. Pa, m, etc.).
All abbreviations should be spelt out in full on first appearance.

Figures

Figures must be cited in consecutive numerical order in the text and referred to in both the text and the caption as Fig. 1, Fig. 2, etc. Figures may be saved in any common format, e.g. BMP, JPG, GIF. However, the use of CDR format (CorelDraw) is recommended for graphs and line drawings, since vector images can be easily reduced or enlarged during final processing of the paper.

When labelling axes, physical quantities (e.g. *v*, *T*, etc.) should be used whenever possible. Multi-curve graphs should have individual curves marked with a symbol; the meaning of the symbol should be explained in the figure caption. Good quality black-and-white photographs or scanned images should be supplied for the illustrations.

Tables

Tables must be cited in consecutive numerical order in the text and referred to in both the text and the caption as Table 1, Table 2, etc. The use of names for quantities in tables should be avoided if possible: corresponding symbols are preferred. In addition to the physical quantity, e.g. *t* (in Italics), units (normal text), should be added on a new line without brackets.
Any footnotes should be indicated by the use of the superscript[1].

LIST OF references

Citation in text

Please ensure that every reference cited in the text is also present in the reference list (and vice versa). Any references cited in the abstract must be given in full. Unpublished results and personal communications are not recommended in the reference list, but may be mentioned in the text, if necessary.

Reference style

Text: Indicate references by number(s) in square brackets consecutively in line with the text. The actual authors can be referred to, but the reference number(s) must always be given:

Example: "... as demonstrated [1,2]. Brandl and Blovsky [4] obtained a different result ..."

List: Number the references (numbers in square brackets) in the list in the order in which they appear in the text.

Reference to a journal publication:
[1] Jelušič, P., Žlender, B. 2013. Soil-nail wall stability analysis using ANFIS. Acta Geotechnica Slovenica 10(1), 61-73.

Reference to a book:
[2] Šuklje, L. 1969. Rheological aspects of soil mechanics. Wiley-Interscience, London

Reference to a chapter in an edited book:
[3] Mitchel, J.K. 1992. Characteristics and mechanisms of clay creep and creep rupture, in N. Guven, R.M. Pollastro (eds.), Clay-Water Interface and Its Rheological Implications, CMS Workshop Lectures, Vol. 4, The clay minerals Society, USA, pp. 212-244.

Conference proceedings:
[4] Brandl, H., Blovsky, S. 2005. Slope stabilization with socket walls using the observational method. Proc. Int. conf. on Soil Mechanics and Geotechnical Engineering, Bratislava, pp. 2485-2488.

Web references:
[5] As a minimum, the full URL should be given and the date when the reference was last accessed. Any further information, if known (DOI, author names, dates, reference to a source publication, etc.), should also be given.

Author information

The following information about the authors should be enclosed with the paper: names, complete postal addresses, telephone and fax numbers and E-mail addresses. Indicate the name of the corresponding author.

Acceptance of papers and copyright

The Editorial Committee of the Slovenian Geotechnical Review reserves the right to decide whether a paper is acceptable for publication, to obtain peer reviews for the submitted papers, and if necessary, to require changes in the content, length or language.
On publication, copyright for the paper shall pass to the ACTA GEOTECHNICA SLOVENICA. The AGS must be stated as a source in all later publication.

For further information contact:

Editorial Board
ACTA GEOTECHNICA SLOVENICA
University of Maribor,
Faculty of Civil Engineering, Transportation Engineering and Architecture
Smetanova ulica 17, 2000 Maribor, Slovenia
E-mail: ags@uni-mb.si

NAMEN REVIJE

Namen revije ACTA GEOTECHNICA SLOVENICA je objavljanje kakovostnih teoretičnih člankov z novih pomembnih področij geomehanike in geotehnike, ki bodo dolgoročno vplivali na temeljne in praktične vidike teh področij.

ACTA GEOTECHNICA SLOVENICA objavlja članke s področij: mehanika zemljin in kamnin, inženirska geologija, okoljska geotehnika, geosintetika, geotehnične konstrukcije, numerične in analitične metode, računalniško modeliranje, optimizacija geotehničnih konstrukcij, terenske in laboratorijske preiskave.

Revija redno izhaja dvakrat letno.

AIMS AND SCOPE

ACTA GEOTECHNICA SLOVENICA aims to play an important role in publishing high-quality, theoretical papers from important and emerging areas that will have a lasting impact on fundamental and practical aspects of geomechanics and geotechnical engineering.

ACTA GEOTECHNICA SLOVENICA publishes papers from the following areas: soil and rock mechanics, engineering geology, environmental geotechnics, geosynthetic, geotechnical structures, numerical and analytical methods, computer modelling, optimization of geotechnical structures, field and laboratory testing.

The journal is published twice a year.

AVTORSKE PRAVICE

COPYRIGHT

ODGOVORNOST

RESPONSIBILITY

www.fg.um.si

www.sloged.si

Univerza v Ljubljani

Fakulteta za gradbeništvo in geodezijo

Naravoslovnotehniška Fakulteta

www.fgg.uni-lj.si
www.ntf.uni-lj.si

www.ita-slovenia.si